Carbon Nanostructures

Carlos P. Bergmann
Fernando Machado Machado *Editors*

Carbon Nanomaterials as Adsorbents for Environmental and Biological Applications

Springer

Carbon Nanostructures

Series editor

Paulo Araujo, Tuscaloosa, AL, USA

More information about this series at http://www.springer.com/series/8633

Carlos P. Bergmann · Fernando Machado Machado
Editors

Carbon Nanomaterials as Adsorbents for Environmental and Biological Applications

Springer

Editors
Carlos P. Bergmann
Escola de Engenharia Departamento
de Materials—LACER
The Federal University of Rio Grande
do Sul
Porto Alegre
Brazil

Fernando Machado Machado
Center of Technological Development
Federal University of Pelotas
Pelotas, RS
Brazil

ISSN 2191-3005 ISSN 2191-3013 (electronic)
Carbon Nanostructures
ISBN 978-3-319-18874-4 ISBN 978-3-319-18875-1 (eBook)
DOI 10.1007/978-3-319-18875-1

Library of Congress Control Number: 2015939165

Springer Cham Heidelberg New York Dordrecht London

Printed on acid-free paper

Springer International Publishing AG Switzerland is part of Springer Science+Business Media (www.springer.com)

Preface

The potential offered by carbon nanomaterials and its innovative applications is attracting increasing interest from various sectors, both academic and industrial, especially application as nanoadsorbent. Carbon nanomaterials can play an important role in this context, and therefore, an emerging research area is the development of new nanomaterials with promisingly high affinity, capacity, and selectivity for adsorption. The removal of obstacles to the use of carbon nanomaterials, enabling products based on nanostructured materials to be available soon to society, will take place as advances occur in the interaction between industry, research centers, and the development of human resources. Therefore, it is essential to exchange information and experiences in these areas. This book "Carbon Nanomaterials as Adsorbents for Environmental and Biological Applications" shall consider this context.

This book presents a development of the current knowledge available regarding the application of this broad and versatile family for water treatment, drug delivery systems, and nanosensors. The first chapter elucidates aspects of the adsorption process. Afterward, we present the characteristics and properties of fascinating carbon nanomaterials for adsorption application. The subsequent chapter of this book presents the kinetic and equilibrium models of adsorption, processing of experimental data, and adsorption process peculiarities. Environmental and biological applications of carbon nanomaterials are discussed in the last chapter.

The clear language and the application-oriented perspective from which this book is written make it suitable for both students and researchers that wish to discover more captivating applications of carbon nanomaterials as nanoadsorbents.

Porto Alegre, Brazil, May 2015 — Carlos P. Bergmann
Pelotas, Brazil — Fernando Machado Machado

Contents

Chapter 1
Introduction

Carlos P. Bergmann, Fernando Machado Machado and Éder Cláudio Lima

Abstract Nanoscience and Nanotechnology have the ability to produce materials with unusual functions and properties that are revolutionizing all segments of industrial. Among the different classes of nanomaterials, carbon nanomaterials such as fullerene, carbon nanotubes, and graphene stand out. These nanomaterials have several practical applications, especially those involving adsorption processes. Carbon nanomaterials show fascinating structures potentially interesting for the development of highly sensitive, selective, and efficient adsorbent devices for the removal of inorganic, organic and biological contaminants from water solutions, as well as for applications as nanosensors and drug delivery systems. In this chapter we demonstrated the number of articles reported in the literature in recent years involving carbon nanomaterials as adsorbents. In addition, this chapter addresses the fundamental aspects of adsorption, such as the distinction between physical adsorption and chemical adsorption.

Keywords Carbon Nanomaterials · Nanoadsorbents · Fullerene · Carbon nanotubes · Graphene · Adsorption

C.P. Bergmann (✉)
Departamento de Engenharia de Materiais, Universidade Federal do Rio Grande do Sul, Porto Alegre, RS 90035190, Brazil
e-mail: bergmann@ufrgs.br

F.M. Machado
Centro de Desenvolvimento Tecnológico, Universidade Federal de Pelotas, Pelotas, RS 96010610, Brazil
e-mail: fernando.machado@hotmail.com.br

É.C. Lima
Instituto de Química, Universidade Federal do Rio Grande do Sul, Porto Alegre, RS 91501970, Brazil
e-mail: profederlima@gmail.com

C.P. Bergmann and F.M. Machado (eds.), *Carbon Nanomaterials as Adsorbents for Environmental and Biological Applications*, Carbon Nanostructures,
DOI 10.1007/978-3-319-18875-1_1

Abbreviations

CN Carbon nanomaterials
CNT Carbon nanotubes
$\Delta G°$ Gibb's free energy change
$\Delta H°$ Enthalpy change
$\Delta S°$ Entropy change

Nanotechnology is one of the twenty-first century's most attractive and promising fields of technological development, with opportunities for research and innovation provided by the unusual properties of matter organised as structures of nanometre dimensions. We can standardise fields of nanotechnology (according to ISO/TC 229 Nanotechnologies) as technologies that include: (i) the understanding and control of matter and processes which are, typically, but not exclusively, below 100 nm in one or more dimensions and where the onset of size-dependent phenomena usually enables novel applications; (ii) utilising the properties of nanoscale materials that differ from those of individual atoms, molecules and bulk matter, to create improved materials, devices and systems that exploit these new properties.

Nanotechnology has aroused considerable interest, not only because of the expectation of the impact nanomaterials may have on improving our quality of life, but also for their potential role in environmental preservation, particularly with respect to water treatment. In recent years, nanotechnology has provided a variety of materials that are currently being evaluated as possible nanoadsorbents for environmental and biological applications. Among the different classes of nanomaterial, carbon nanomaterials (CN) stand out, including fullerene [1], carbon nanotubes (CNT) [2–4] and the graphene-family [5] (see Fig. 1.1).

Recent studies indicate that many of today's water quality problems could be solved via the use of CN. Several research groups are currently focusing on the treatment-purification of wastewater using CN as nanoadsorbents. The goal of most of the activities developed by these groups is to demonstrate the efficiency of CN in comparison to that of traditional adsorbents, especially activated carbon. One method with which to fully appreciate the importance that has been/is given to CN for this purpose is to conduct a review of articles published on the subject. Analysis of Fig. 1.2, which presents the results of such a survey, reveals significant annual increases in paper numbers. For example, in 2014, more than 2200 papers were available in the literature regarding the use of CN for water treatment, approximately 38 % more than the year before and over twenty times more than in 2004. It is noteworthy that in 2015 there are already 1144 publications on this topic.

Among the three classes of nanomaterials that will be evaluated in this book as potential carbon nanoadsorbents, CNT have been most extensively examined for adsorption applications. Several studies have reported that CNT possess a good adsorption capacity for many of the organic and inorganic pollutants present in aqueous phases [6, 7]. Although members of the graphene—family

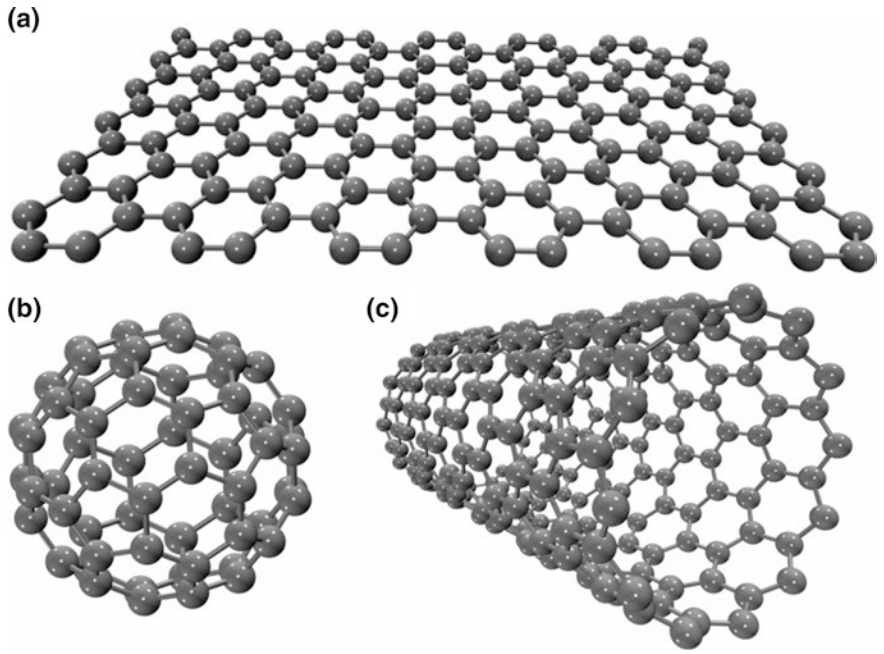

Fig. 1.1 CN structures with potential for adsorption applications: **a** graphene, **b** fullerene and **c** carbon nanotube

(such as graphene oxide and reduced graphene oxide) have not yet been studied as extensively as CNT, several authors have demonstrated the capacity of these materials to successfully remove various contaminants, including antibiotics [8], heavy metals [9] and synthetic dyes [8, 10], from aqueous solutions. The adsorptive activity of fullerenes for organic pollutant [6, 10] compounds in water has also been investigated, but at a lower intensity compared to that for the other two carbon allotropes.

In terms of biological applications, there has been a significant amount of research conducted regarding new ways of detecting and treating diseases using CN for drug delivery, as well as for biosensor monitoring. Considerable effort is currently focused on finding the ideal materials with which to ensure the optimal characteristics of nanostructured sensors [11–13] and drug delivery systems [14, 15]. CN have great potential for such applications, as evidenced by the growing number of publications in this area. Figures 1.3 and 1.4 show, respectively, a historical survey of articles published regarding the use of CN in drug delivery systems and biosensors for the period between 2004 and 2015.

An understanding of the phenomena involved in the adsorption process is of vital importance for the development of drug delivery systems and more efficient nanosensors.

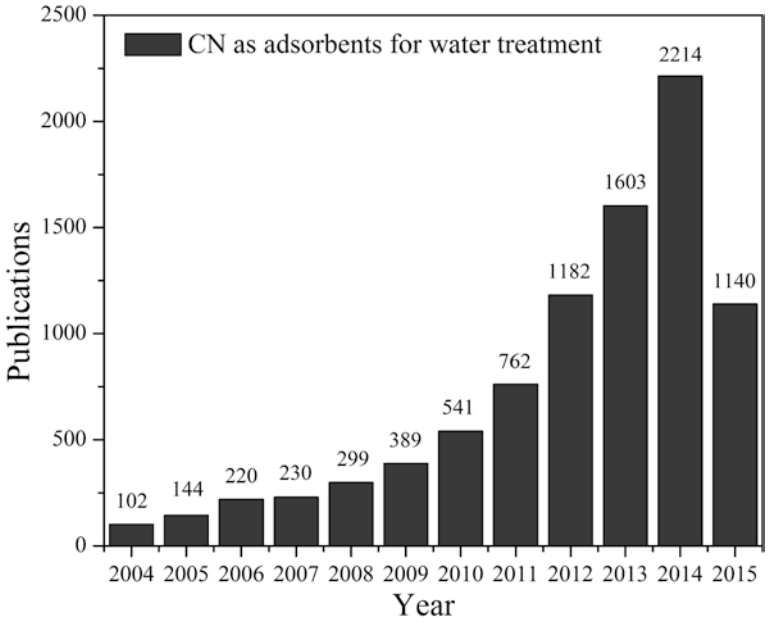

Fig. 1.2 Articles published since 2004 regarding the application of CN as adsorbents for water treatment (www.sciencedirect.com, last accessed 25th February 2015)

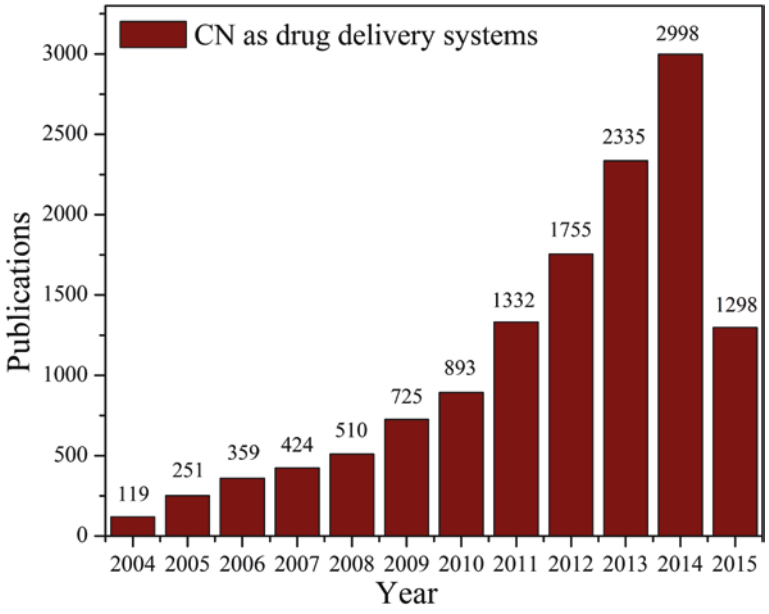

Fig. 1.3 Articles published since 2004 regarding the application of CN in drug delivery systems (www.sciencedirect.com, last accessed 25th February 2015)

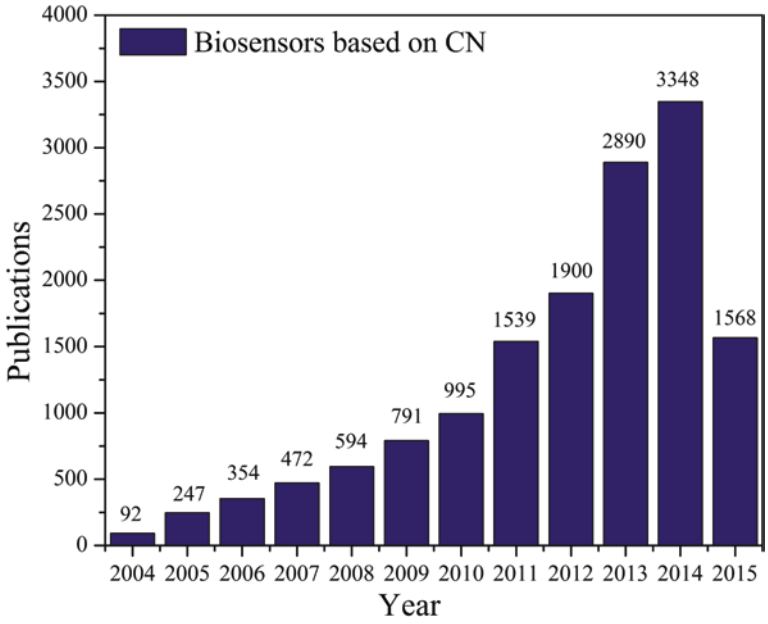

Fig. 1.4 Articles published since 2004 regarding the development of CN-based biosensors (www.sciencedirect.com, last accessed 25th February 2015)

1.1 What Is Adsorption?

A focus of study since the beginning of the last century [16], adsorption phenomena occurring at different interfaces are seen in a number of processes in everyday life, with their practical application in industry, environmental protection and biological media extremely important.

Innumerable chemical, physical and biological processes occur at the boundary between two phases. Adsorption is effectively the change in concentration of a given substance at the interface with respect to that of neighbouring phases [16]. Depending on the type of phases in contact, we can consider this process in the following systems: liquid-gas, liquid-liquid, solid-solid, solid-liquid and solid-gas. For the purposes of this book, we will consider only the solid-liquid system.

Adsorption is essentially a surface phenomenon involving two components: (i) the compound that is attached to the solid surface, i.e. the material in the adsorbed state, defined as the 'adsorbate', and (ii) the compound on which adsorption occurs, known as the 'adsorbent'. It is worth pointing out that the penetration by the adsorbate molecules into the bulk solid phase is typically defined as 'absorption'; the terms 'sorption', 'sorbent', "sorbate" and "sorptive", are also used to denote both adsorption and absorption, when both occur simultaneously or cannot be distinguished [16].

Table 1.1 The general features of physisorption and chemisorption

Features	Physisorption	Chemisorption
Origin of interactions	Van der Waals bonds (no common electronic orbitals)	Chemical bonds (common electronic orbitals)
Specificity	Non specific	Specific
Heat of adsorption	Low heat of adsorption (<2 or 3 times latent heat of evaporation)	High heat of adsorption (>2 or 3 times latent heat of evaporation)
Number of adsorbed layers	Monolayer or multilayer	Monolayer
Dissociation	No dissociation of adsorbent species	May involve dissociation
Electrons transfer	No electrons transfer although polarization of sorbate may occur	Electron transfer leading to bond formation between sorbate and surface

When discussing the fundamentals of adsorption it is useful to make a distinction between physical adsorption (physisorption), which involves only relatively weak intermolecular forces, and chemical adsorption (chemisorption), which involves, essentially, the formation of a chemical bond between the sorbate molecule and the surface of the adsorbent [17]. The general features which distinguish physisorption and chemisorption are presented in Table 1.1.

Although this distinction (Table 1.1) is conceptually useful, there are many intermediate cases and it is not always possible to categorise a particular system unequivocally. In some situations, the thermodynamic parameters related to the adsorption process, i.e. Gibb's free energy change ($\Delta G°$, kJ mol^{-1}), enthalpy change ($\Delta H°$, kJ mol^{-1}) and entropy change ($\Delta S°$, J mol^{-1} K^{-1}), can be used to define the magnitude of the adsorption process. These parameters are determined via the following equations:

$$\Delta G^0 = \Delta H^0 - T\Delta S^0 \tag{1.1}$$

$$\Delta G^0 = -RT \ln (K) \tag{1.2}$$

Equation 1.3 is obtained from Eqs. 1.1 and 1.2;

$$\ln (K) = \frac{\Delta S^0}{R} - \frac{\Delta H^0}{R} \cdot \frac{1}{T} \tag{1.3}$$

where R is the universal gas constant (8.314 J K^{-1} mol^{-1}), T is the absolute temperature (Kelvin) and K represents the equilibrium adsorption constants of the isotherm fits [7].

A variety of different adsorption equilibrium constants (K) have been obtained from different isotherm models [18, 19]. The values of $\Delta H°$ and $\Delta S°$ can be calculated from the slope and intercept of the linear plot of ln (K) versus 1/T, with the type of interaction taking place classified, to a certain extent, by the magnitude of enthalpy change [20]. Instances of physisorption, such as van der Waals'

interactions, are usually lower than 20 kJ mol^{-1} [21]. Electrostatic interaction ranges from 20 to 80 kJ mol^{-1} and is frequently classified as physisorption [20, 22]. Chemisorption bond strengths can range at around 80–450 kJ mol^{-1} [23].

Besides the magnitude of the adsorption, the thermodynamic parameters obtained from Eqs. 1.1, 1.2 and 1.3 enable the acquisition of other information regarding the adsorption process. Positive values of $\Delta H°$ indicate an endothermic process that occurs with the absorption of energy [22]. Conversely, negative values of $\Delta H°$ denote an exothermic process, translated as energy release [24]. Negative values of $\Delta G°$ are indicative of a process that is spontaneous and thermodynamically favourable, with the adsorbate having a high affinity with the adsorbent [24]. In addition, the more negative the value of $\Delta G°$ the greater the driving force of the adsorption process, resulting in a higher adsorption capacity [25]. Positive values of $\Delta S°$ demonstrate a high preference of adsorbate molecules on the surface of the adsorbent, and also suggest the possibility of some structural changes or readjustments in the adsorbate—adsorbent adsorption complex [22].

From a theoretical point of view, knowledge of the magnitude of enthalpy alone, which may be associated with the binding energy, is not sufficient to identify a process as physical or chemical adsorption. To determine an interaction as physical or chemical, we must also take into consideration other parameters such as charge transfer and bond distance, as well as conduct a detailed analysis of the electronic energy bands of the systems involved [20, 26–28].

1.2 Why Use Carbon Nanomaterials as Adsorbents for Environmental and Biological Applications?

CN have been analysed extensively for adsorption applications due to their good chemical stability, structural diversity, low density and suitability for large-scale production. Their textural properties, such as average pore diameter, total pore volume and infinitely high surface-to-volume ratio, have stimulated a large number of investigations into the use of CN as potential adsorbents for water purification and for biological applications [7, 20, 22]. The chemical nature of CN allows their surfaces to be easily modified via chemical and physical treatments, thus enabling the directed improvement of their properties [29]. Additionally, the possibility of performing biofunctionalisations suggests a large number of potential applications for use in biological systems [30]. These characteristics make CN a fascinating target subject for the development of highly sensitive, selective and efficient adsorbent devices for the removal of inorganic, organic and biological contaminants from water solutions, as well as for the development of drug delivery systems and nanosensors.

Acknowledgments The authors acknowledge funding from Brazilian agencies CNPq, CAPES, FAPERGS and INCT Nanomateriais de Carbono.

References

1. Kroto HW, Heath JR, Obrien SC, Curl RF, Smalley RE (1985) C_{60}: buckminsterfullerene. Nature 318:162–163
2. Iijima S (1991) Helical microtubules of graphitic carbon. Nature 354:56–58
3. Iijima S, Ichihashi T (1993) Single-shell carbon nanotubes of 1-nm diameter. Nature 363:603–605
4. Bethune DS, Klang CH, De Vries MS et al (2003) Cobalt-catalysed growth of carbon nanotubes with single-atomic-layer walls. Nature 363:605–607
5. Novoselov KS, Geim AK, Morozov SV et al (2004) Electric field effect in atomically thin carbon films. Science 306:666–669
6. Gupta VK, Saleh TA (2013) Sorption of pollutants by porous carbon, carbon nanotubes and fullerene—an overview. Environ Sci Pollut Res 20:2828–2843
7. Machado FM, Bergmann CP, Fernandes THM et al (2011) Adsorption of reactive red M-2BE dye from water solutions by multi-walled carbon nanotubes and activated carbon. J Hazard Mater 192:1122–1131
8. Chowdhury S, Balasubramanian R (2014) Recent advances in the use of graphene-family nanoadsorbents for removal of toxic pollutants from wastewater. Adv Colloid Interface Sci 204:35–56
9. Huang Z-H, Zheng X, Lv W, Wang M, Yang Q-H, Kang F (2011) Adsorption of lead(II) ions from aqueous solution on low-temperature exfoliated graphene nanosheets. Langmuir 27:7558–7562
10. Li Y, Du Q, Liu T et al (2013) Comparative study of methylene blue dye adsorption onto activated carbon, graphene oxide, and carbon nanotubes. Chem Eng Res Des 91:361368
11. Wang Y, Li Z, Wang J, Li J, Lin Y (2001) Graphene and graphene oxide: biofunctionalization and applications in biotechnology. Trends Biotechnol 29(5):205–212
12. Shao W, Paul A, Zhao B, Lee C, Rodes L, Prakash S (2013) Carbon nanotube lipid drug approach for targeted delivery of a chemotherapy drug in a human breast cancer xenograft animal model. Biomaterials 34(38):10109–10119
13. Kuila T, Bose S, Khanra P, Mishra AK, Kim NH, Lee JH (2011) Recent advances in graphene-based biosensors. Biosens Bioelectron 26(12):4637–4648
14. Liu J, Cui L, Losic D (2013) Graphene and graphene oxide as new nanocarriers for drug delivery applications. Acta Biomater 9(12):9243–9257
15. Wong BS, Yoong SL, Jagusiak A et al (2103) Carbon nanotubes for delivery of small molecule drugs. Adv Drug Deliv Rev 65(15):1964–2015
16. Dąbrowski A (2001) Adsorption—from theory to practice. Adv Colloid Interface Sci 93:135–224
17. Ruthven DM (1984) Principles of adsorption and adsorption processes. Wiley, New York
18. Calvete T, Lima EC, Cardoso NF, Vaghetti JCP, Dias SLP, Pavan FA (2010) Application of carbon adsorbents prepared from Brazilian-pine fruit shell for the removal of reactive orange 16 from aqueous solution: kinetic, equilibrium, and thermodynamic studies. J Environ Manag 91:1695–1706
19. Calvete T, Lima EC, Cardoso NF, Dias SLP, Pavan FA (2009) Application of carbon adsorbents prepared from the Brazilian-pine fruit shell for removal of Procion Red MX 3B from aqueous solution—kinetic, equilibrium, and thermodynamic studies. Chem Eng J 155:627–636
20. Machado FM, Bergmann CP, Lima EC et al (2012) Adsorption of reactive blue 4 dye from water solutions by carbon nanotubes: experiment and theory. Phys Chem Chem Phys 14:11139–11153
21. Sun CL, Wang CS (2010) Estimation on the intramolecular hydrogen-bonding energies in proteins and peptides by the analytic potential energy function. J Mol Struct 956:38–43
22. Prola LDT, Machado FM, Bergmann CP et al (2013) Adsorption of direct blue 53 dye from aqueous solutions by multi-walled carbon nanotubes and activated carbon. J Environ Manage 130:166–175

23. Kuo CY, Wu CH, Wu JY (2008) Adsorption of direct dyes from aqueous solutions by carbon nanotubes: Determination of equilibrium, kinetics and thermodynamics parameters. J Colloid Interface Sci 327:308–315
24. Kuo CY, Wu CH, Wu JY (2008) Adsorption of direct dyes from aqueous solutions by carbon nanotubes: Determination of equilibrium, kinetics and thermodynamics parameters. J Colloid Interface Sci 327:308–315
25. Chao L, Lu Z, Li A et al (2005) Adsorption of reactive dyes onto polymeric adsorbents: effect of pore structure and surface chemistry group of adsorbent on adsorptive properties. Sep Purif Technol 44:91–96
26. Girão CE, Liebold-Ribeiro Y, Batista J et al (2010) Functionalization of single-wall carbon nanotubes through chloroform adsorption: Theory and experiment. Phys Chem Chem Phys 12:1518–1524
27. Ferreira OP, Otubo L, Aguiar AL (2009) Non-covalent interaction of benzonitrile with single-walled carbon nanotubes. J Nanopart Res 11:2163–2170
28. Fagan SB, Souza Filho AG, Lima JOG et al (2004) 1,2-Dichlorobenzene interacting with carbon nanotubes. Nano Lett 4:1285–1288
29. Mishra AK, Arockiadoss T, Ramaprabhu S (2010) Study of removal of azo dye by functionalized multi walled carbon nanotubes. Chem Eng J 162:1026–1034
30. Wang Y, Li Z, Wang J, Li J, Lin Y (2011) Graphene and graphene oxide: biofunctionalization and applications in biotechnology. Trends Biotechnol 29:205–212

Chapter 2
Carbon Nanoadsorbents

Fernando Machado Machado, Solange Binotto Fagan, Ivana Zanella da Silva and Mônica Jung de Andrade

Abstract Nanoscience and Nanotechnology suggest that many of the current problems involving water quality can be solved or greatly ameliorated using the nanoscale adsorbents, called nanoadsorbents. Innovations in the development of novel carbon nanomaterials like fullerenes, carbon nanotubes, and graphene are among the most exciting and promising materials for water treatment—purification. This chapter gives detailed description of the structure, morphology, and adsorption properties of carbon nanoadsorbents. The textural properties of fullerene, carbon nanotubes, and graphene family are highlighted. A brief description of the effects of the electronic properties in the adsorption capability was inferred as well as how the adsorption of molecules may affect photoelectronic properties of carbon nanotubes.

Keywords Textural properties · Adsorption property · Fullerene · Carbon nanotubes · Graphene

F.M. Machado (✉)
Centro de Desenvolvimento Tecnológico, Universidade Federal de Pelotas, Pelotas, RS 96010610, Brazil
e-mail: fernando.machado@hotmail.com.br

S.B. Fagan · I.Z. da Silva
Área de Ciências Tecnológicas, Centro Universitário Franciscano, Santa Maria, RS 97010032, Brazil
e-mail: solange.fagan@gmail.com

I.Z. da Silva
e-mail: ivanazanella@gmail.com

M.J. de Andrade
Nanotech Institute, University of Texas at Dallas, Richardson, TX 75080, USA
e-mail: mja0612@gmail.com

C.P. Bergmann and F.M. Machado (eds.), *Carbon Nanomaterials as Adsorbents for Environmental and Biological Applications*, Carbon Nanostructures,
DOI 10.1007/978-3-319-18875-1_2

Abbreviations

0D	Zero-dimensional
1D	One-dimensional
2D	Two-dimensional
3D	Bulk
2D	Two-dimensional
3D	Bulk
CNT	Carbon Nanotube
CVD	Chemical Vapor Deposition
DOS	Density of States
FLG	Few-Layer Graphene
GO	Graphene Oxide
MWCNT	Multiwall Carbon Nanotube
rGO	Reduced Graphene Oxide
SWCNT	Single-walled Carbon Nanotubes

2.1 Introduction

The nanomaterials, particularly carbon nanostructures, are promising systems for several applications, in particular for molecule adsorption due to their intrinsic dimensionality, textural, and electronic properties.

The carbon allotropes differ in the coordination number of the carbon atoms or in the packaging sequence of the layers in the crystal lattice environment. Different degrees of sp^2 hybridization result in carbonaceous nanomaterials with distinct atomic bounds and arrangements. For example, a 2D carbon allotropic form, such as graphene [1], is a hypothetical infinite aromatic surface with sp^2 hybridization and a carbon atom thickness. The structure of single-walled (SWCNT) [2, 3] and multiwalled carbon nanotubes (MWCNT) [4], both 1D systems, can be simplified as the result of one or more graphene sheets rolled up in a concentric form, respectively. On the other hand, a 0D system such as fullerene, C_{60}, consists of 60 carbon atoms with sp^2-like hybridization with 20 hexagonal and 12 pentagonal rings, which are responsible for its curvature [5]. These topological changes provide different interactions between carbon-based nanoadsorbents and the adsorbate molecule [6, 7]. Apart from fullerene, carbon nanotubes, and graphene family in isolated form, it should be also taken into account those materials when available in 3D arrangements (bulk) [8]. Figure 2.1 presents some examples for 0D, 1D, 2D, and 3D carbon nanostructures. The union of several isolated carbon structures can change the behavior of adsorption process [9] because when they are in clusters form they present new unit adsorption sites [9–13].

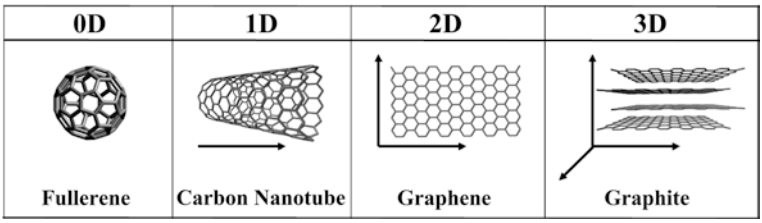

Fig. 2.1 Examples for 0D, 1D, 2D, and 3D carbon nanostructures

2.2 Structure, Morphology, and Adsorption Properties of Carbon Nanoadsorbents

The textural properties such as surface area, pore volume, and average pore diameter (for a better understanding of the different types of pores of the carbon nanostructures, see Sect. 4.2) of the carbon nanostructures are the main factors that determine the adsorption capacity [7, 14].

Further, the adsorption surface sites or dangling bonds of the structures can also play an important role in the adsorption process because, in general, are highly reactive [7]. The carbonaceous nanomaterials surface can also be considered amphoteric, where they can be protonated (positively charged) or deprotonated (negatively charged) [14] (this feature will be detailed in Sect. 4.4). Furthermore, other functional groups can be added with oxygen, which can provide new sites for chemical adsorption [14].

In this context, this section aims to provide information on the adsorption properties of graphene, carbon nanotubes, fullerene, and its related materials.

2.2.1 Adsorption Properties of Fullerene

The fullerenes are carbon-based zero-dimensional (0D) materials, with sp^2-like hybridization due to the curvature effect. The C_{60} molecule has approximately 7 Å of diameter and is composed of 12 pentagons and 20 hexagons of carbon atoms [5]. The number of carbon atoms on a fullerene can range from 20, 60, 70, 82, 100, 180 to 960 (always an even number) [15]. As the number of hexagons is greater than 20 (in case of C_{60}), the stability of the molecule decreases as pentagons occupy increasingly tensioned position and therefore more susceptible to chemical attack.

The fullerenes can be synthesized by laser ablation [5], through the carbon vaporization or from the graphite rod heated at high temperatures and by arc discharge between graphite electrodes [16]. Other routes of production can also be used via synthesis in combustion [17], hybrid plasma [18], and thermal plasma [19], among others.

The thermal and chemical properties of fullerene, including their possibility to be an electron acceptor, attract commercial and scientific interest for environmental applications [20].

Table 2.1 Surface area of some samples of fullerenes reported in the literature

Fullerene type	BET surface area ($m^2\ g^{-1}$)	Reference
Fullerene	85.05	[22]
Fullerene	1.10	[23]
Fullerene	85.00	[24]
Fullerene	42.00	[25]
Fullerene soot	176.00	[21]
Fullerene soot CO_2 (850 °C, 5 h) treated	345.00	[21]
Fullerene soot argon (850 °C, 5 h) treated	346.00	[21]

The specific surface area (by Brunauer, Emmett, Teller–BET method) of fullerene obtained experimentally vary from approximately 1.1–176 $m^2\ g^{-1}$ [21–25]. This discrepancy can be attributed to the different methods of syntheses. Table 2.1 shows that physical and chemical treatments [21] on fullerene surface can change the resulting properties of the systems. The heat treatment with CO_2, for example, leads to the corrosion of carbon and the result of this reaction is carbon monoxide production and the elimination of –OH and $–CH_3$ surface groups. Results of BET (Table 2.1) show that these phenomena lead to an increase of the surface area of fullerene. Besides the chemical modifications, the heat treatment may also lead to an opening of small pores located inside the carbon particles which results in an increase of the total surface area [21].

The characteristics of fullerenes structures, as the inner and outer surface covered with homogeneous π electrons, allow a strong interaction with organic molecules such as endocrine disrupting chemicals through π–π stacking [20]. In fullerene clusters there are distinct adsorption sites that can contribute significantly to the overall adsorption. As seen in Fig. 2.2, adsorption on fullerene aggregates can occur at three different sites [20]: adsorption areas of surface (*A*), groove (*B*) formed at the contact between adjacent fullerene, and interstitial spaces (*C*) between the fullerenes in aggregates.

The adsorptive activity of fullerenes for organic pollutants such as organic and organometallic compounds [26], polycyclic aromatic hydrocarbon [27] and naphthalene and 1,2-dichlorobenzene [28] in aqueous solutions have been investigated. In addition, organochlorine compounds adsorption in aqueous solutions was investigated and compared with activated carbon and mixed with and without fullerenes [29]. The adsorption behavior of fullerene was found to be higher to that of activated carbon. It has been concluded that adsorption on fullerenes proceeds mainly by physical adsorption through dispersive interaction forces [27]. Some examples of pollutants adsorption on fullerenes will be discussed in Chaps. 5 and 6.

2.2.2 Adsorption Properties of Carbon Nanotubes

Similar to fullerenes, carbon nanotubes (CNT) are carbon allotropes with an aromatic surface when the carbon atoms are in a sp^2-like hybridization rolled up in a tubular structure (1D system) [8]. This carbon allotrope is a unique nanostructure

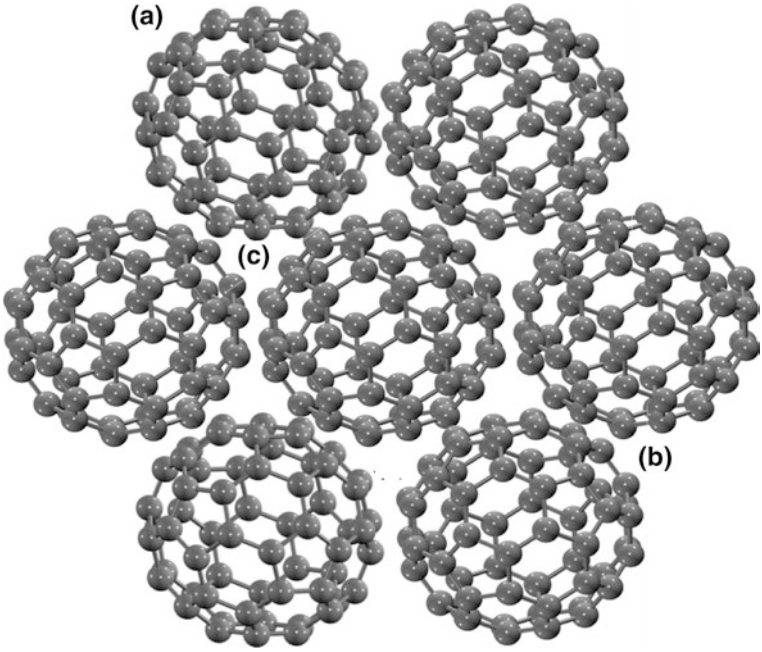

Fig. 2.2 Schematic model for the possible adsorption sites of fullerene aggregates: surface area (**a**), groove at interstitial spaces (**b**), and between aggregates (**c**)

with remarkable electronic and mechanical properties that depend directly to their chirality and diameter [30]. These exceptional properties combined with unusual morphology, become extremely attractive for many practical applications, such as, the development of devices for energy storage [10] and adsorption, with high sensitivity, selectivity, and efficiency [7, 13].

The main techniques to obtain CNT can be basically divided into high temperature methods which include arc discharge and laser ablation synthesis; and methods at moderate temperatures, which correspond mainly to chemical vapor deposition (CVD) [30].

With regard to the adsorption properties of CNT it is pertinent to consider their outer and inner surfaces. In particular, the rolling up of the graphene sheet to form the tube causes a rehybridization of carbon orbital (nonplanar sp^2 configuration), changing the charge surface compared with the original graphene sheet [9]. This curvature can result in unlikely thermodynamical properties for the adsorption process with the CNT compared with the flat carbon sheet [9].

Several studies highlight the porous nature of the CNT [31–34]. In MWCNTs the nature of the porous can be classified as inner hollow cavities of small diameter (ranging from 3 to 6 nm in a narrow distribution of sizes) and aggregated pores (widely distributed, 20–40 nm), formed by interaction between the CNTs [34]. The aggregated pores are formed by entanglement of several MWCNTs, which are adhered to each other as a result of van der Waals forces [35].

Many methods of characterization have shown the microporous preferable nature of SWCNTs and the mesoporous preferable nature of MWCNT (for a better understanding of the pore size denomination, see Sect. 4.2) [9]. Consequently, the first one (SWCNT) often exhibits a specific surface area higher than the others. Experimentally (see Table 2.2), it is reported that the surface area of as-grown SWCNT ranges between 370 [44] to 1587 $m^2\ g^{-1}$ [10] (micropore volume of 0.15–0.3 $cm^3\ g^{-1}$), less than the theoretically expected specific surface area for an isolated SWCNT (2600 $m^2\ g^{-1}$) [36]. The as-grown MWCNT has a surface area between 180.9 and 507 $m^2\ g^{-1}$ (mesopore volume of 0.5–2 $cm^3\ g^{-1}$) (see Table 2.2).

Due to the van der Waals interactions, the SWCNT adhere to each other and form bundles as shown in Fig. 2.3. For SWCNT, the diameter of the tubes and the number of tubes in the bundle will affect mainly the textural properties values, since in bundle the adsorption sites are different to those expected for an individual nanotube [11, 13]. As seen in Fig. 2.3, the adsorption on SWCNT bundle can occur at four different sites: (i) the grooves formed at the contact between adjacent tubes; (ii) outside of the bundles; (iii) the interstitial channels between the tubes in bundles; and (iv) inside of the nanotubes (pores) with open ends [9, 13].

The interstitial channels formed between the SWCNTs in bundles have good potential for the small molecules adsorption, such as gases [10]. In contrast to the SWCNT, the MWCNTs are not in the bundles form and their adsorption sites consist of pores aggregated in the inner MWCNT surface with open ends and on the outer walls, as shown in Fig. 2.4 [34, 37]. In this last case, also the presence of defects should be considered as reactive sites for adsorption. Particularly, the aggregated pores play a significant role in the adsorption of large biological contaminants such as bacteria and viruses [35].

The structural properties of CNT allow a strong interaction with organic molecules through noncovalent forces such as hydrogen bonding, π–π stacking, electrostatic forces, van der Waals forces, and hydrophobic interactions [38]. Furthermore, the CNT structure permits the incorporation of one or more chemical functional groups, which may increase the selectivity and the stability of the resulting system [39–41]. The chemical functional groups may be anchored to the CNT surface through functionalization or purification processes [39–41]. Chemical purification methods can alter significantly the specific CNT surface area, as well as its micropores and mesopores volume and the pore diameter average. The chemical purification, also named oxidative purification, can be carried out, for example, by acid solutions (such as HCl, HNO_3, and H_2SO_4), basic compounds (such as KOH and NH_3), and gaseous compounds (such as O_2, CO_2, and O_3) [30]. Thermal purification processes may also modify the textural properties of the CNT. Table 2.2 shows the textural properties, i.e., surface area (BET), total pore volume, and pore diameter average (by Barret, Joyner, and Halenda method—BJH) of various samples of CNT reported in the literature, as well as the influence of some purification—functionalization processes.

As seen in Table 2.2, the purification or functionalization process can alter significantly the textural properties of CNTs. They increase or decrease the specific surface area (BET), total volume pore, or even resulting in the modification of the

Table 2.2 Characteristics and textural properties of SWCNT and MWCNT

CNT type	Characteristics	BET surface area ($m^2\ g^{-1}$)	Total pore volume ($cm^3\ g^{-1}$)	Average pore diameter (nm)	Reference
SWCNT	Pristine	1587.0	–	–	[10]
SWCNT	Pristine	577.0	1.15	7.98	[42]
SWCNT	Pristine	580.0	1.30	1.72	[43]
SWCNT	Pristine	370.7	0.41	5.0	[44]
SWCNT HCl treated	Removing the support oxide	387.7	0.66	6.83	[12]
SWCNT HNO_3 treated	–COOH functional groups are added to the defect and end sites of SWCNTs	820.0	0.629	2.7	[45]
SWCNT O_3 treated	Opens end caps, introduces holes presence and functional groups in surface	320.0	0.81	1.83	[43]
SWCNT O_3/H_2O_2 treated	Opens end caps, introduces holes presence and functional groups in surface	480.0	0.58	1.67	[43]
SWCNT NaClO treated	Oxygen-containing functional groups are added on the surface of SWCNT	397.0	0.46	4.62	[42]
MWCNT	Pristine	448.0	1.10	8.26	[42]
MWCNT	Pristine	180.9	0.345	7.62	[37]
MWCNT	Pristine	195.0	–	10.3	[46]
MWCNT	Pristine	507.0	1.06	7.84	[47]
MWCNT $H_2SO_3/KMnO_4$ treated	Adding functional groups such as carbonyl, carboxyl, and hydroxyl groups	110.0	–	–	[48]
MWCNT KOH treated	Increases micropores and mesopores and the greater the KOH/CNT ratio, the higher the pore volume	785.0	–	2.0–4.0	[49]
MWCNT NH_3 treated	Treatment with NH_3 removes hydroxyl and carboxyl groups	195.0	–	9.2	[46]
MWCNT CO_2 treated	CO_2-activated MWCNT have large micropore volume	429	–	1.2–4.0	[49]
MWCNT heat treated	Functional groups blocking pore entrances are thermally decomposed enhancing external surface area	550.0	1.15	7.77	[47]

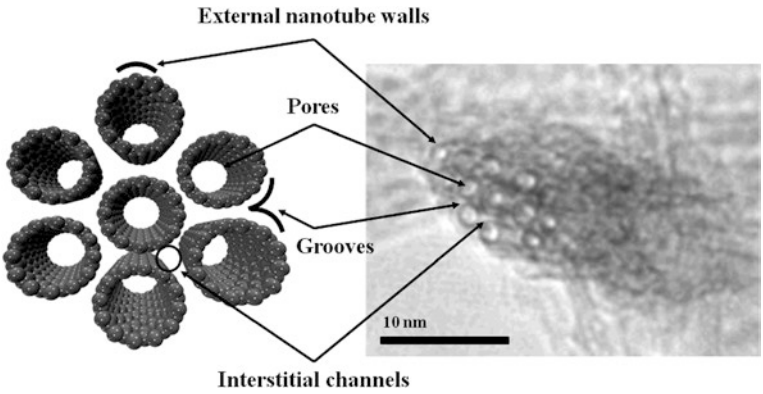

Fig. 2.3 Schematic model for the possible adsorption sites of SWCNT bundle (*left*) and TEM image of SWCNT bundle (*right*)

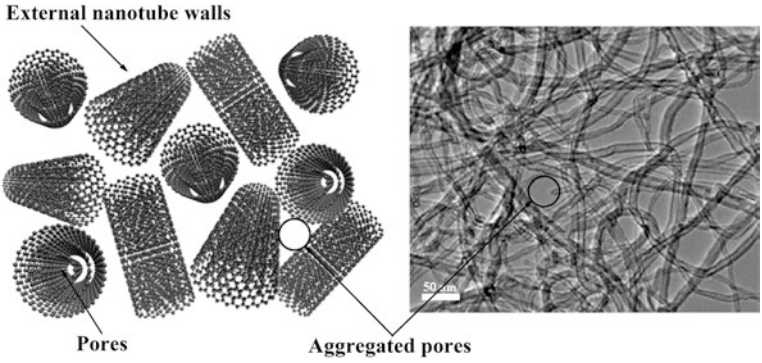

Fig. 2.4 Schematic model for the pores aggregated of MWCNT (*left*) and TEM image of aggregated MWCNTs (*right*)

chemical surface of these nanostructures. The range of the values for the surface area, total volume pore, and pore diameter average can be attributed to the changes not only in morphology of the samples, but also on the type of purification—functionalization used. The oxygen content (OH, COOH, C=O) on CNTs influences the maximum adsorption capacity and can depend on the synthesis and purification steps or intentionally generated by oxidation with acids, plasma, ozone or removed by thermal treatment [50]. Moderate oxidation of CNTs increases their capability to adsorb aromatic compounds through π–π interactions, however, strong oxidations lead to amorphous carbon formation, which is deleterious for availability of sites for π–π interactions [51]. It was also observed that once oxygen concentration on MWCNTs reach 18 %, effects like electron polarizability, solution pH, and solute pKa become negligible. However, even though CNTs with lower surface oxidation are more sensitive to environmental conditions than those

that were functionalized (these are more selective than pristine ones), CNTs with more oxygen content can lead to different mechanisms: yield lower adsorption capacity due to decrease of surface area and less accessible area for adsorption [50, 51] or by contrast lead to hydrogen bonding, dispersive and electrostatic interactions [50, 51]. In some cases, the presence of impurities on the CNT such as catalyst particles and amorphous carbon can facilitate the surface coating of SWCNT bundle and influence directly the adsorption on the outer surface [10].

2.2.3 Adsorption Properties of Graphene Family

The graphene family, such as, graphene, graphene oxide (GO), and reduced graphene oxide (rGO) have been exhaustively studied since their discovery due to their unique physical–chemical properties [1, 8], which refer to the various practical applications. With the growing demand for potable water, the feasibility, and the suitability of using this vast family of nanomaterials, primarily consisting of carbon atoms, as potential alternative for the prevention, control and reduction of water pollution adsorbents is being considered. Graphene, GO, and rGO have distinct morphological and chemical characteristics as shown in Fig. 2.5. These differences derive mainly from the different methods of synthesis [52], inferring in diverse properties and applications.

Graphene (Fig. 2.5a) can be obtained either by top-down or by bottom-up methodology. Top-down approaches usually refer to the mechanical exfoliation of graphite to obtain a single or few-layer graphene (FLG). The oxidation and exfoliation of the graphite can also be obtained by the application of strong oxidizing agents to give the GO, followed by chemical reduction or thermal exfoliation to produce graphene. Several top-down techniques are described in the literature for obtaining graphene, ranging from electrochemical exfoliation [53] to liquid-phase exfoliation [54]. Top-down approaches offer the opportunity to inexpensively produce large quantities of graphene, however, is difficult to achieve graphene sheets with high quality due to the introduction of defects during exfoliation. On the other hand, the bottom-up approach can produce defect-free graphene sheets with exceptional physical properties, but this involves high production costs. Examples of this approach are techniques such as CVD [55] and epitaxial growth [58], involving the direct synthesis of graphene from organic precursors.

As to textural properties of graphene, many authors emphasize the high surface area (by BET method) as that obtained experimentally, which may vary from approximately 295.6–1205.8 $m^2\ g^{-1}$ (see Table 2.3) [57, 58]. It is significant that the surface area is much smaller than the theoretical value of a single layer of graphene, of 2630 $m^2\ g^{-1}$ [59]. This difference can be attributed to incomplete exfoliation of graphene oxide during synthesis, agglomerations of layers during the reduction process, and to overlapping of nanolayers due van der Waals interactions between the graphene sheets [6, 60]. Defects as wrinkling and folding of graphene sheets, as well as the presence of curled sheets also contribute to the decreased surface area [57].

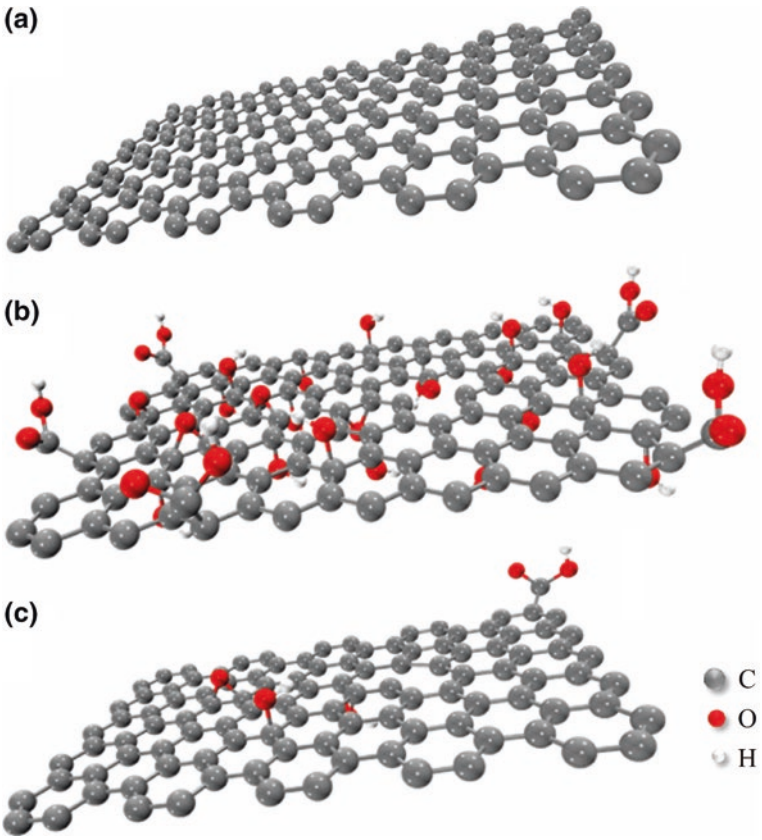

Fig. 2.5 Schematic illustrating the chemical structure of a single sheet of **a** graphene, **b** GO, and **c** rGO

With regard to pore size, is highlighted the presence of slit pore between the parallel layers of graphene [57, 61] (this characteristic will be elucidated in Sect. 4.2). The distribution of porosity (BJH) in graphene as synthesized reveals the presence of a large amount of micro and mesopores, which explains the large surface area of this nanomaterial [57]. However, the value of the average pore diameter (BJH) indicates that graphene is a mesoporous material [60–62]. Table 2.3 has the textural properties of some graphene samples found in the literature and their production methods.

The different values of textural properties presented in Table 2.3 can be assigned to the different routes for obtaining graphene. In fact, the textural properties, especially the surface area, depend on the number of graphene nanolayers sample. The agglomeration and the stacking of graphene layers result in a number of areas inaccessible on surface, which explains the lower surface area [68, 69]. Production methods are capable of synthesizing samples with fewer layers of material to produce larger surface area [57, 60].

Table 2.3 Synthesis methods and textural properties of graphene

Samples	Synthesis method	Surface area ($m^2\ g^{-1}$)	Pore volume ($cm^3\ g^{-1}$)	Average pore size (nm)	Reference
Graphene	Modified hummers method followed hydrazine reduction	295.56	–	3.49	[60]
Graphene	Modified hummers' method followed by heating at 1050 °C for 30 s	455.6	1.34	11.81	[63]
Nitrogen-doped graphene	Heating graphene under high purity ammonia mixed with Ar at 900 °C	595.6	1.82	12.20	[64]
Nitrogen-doped graphene sheets	Modified hummer addition of melamine and microwave	446.00	1.62	–	[65]
FLG	Modified hummers method and expansion and exfoliation with thermal method	560.6	0.263	18.76	[66]
FLG	Modified Hummers' method followed by reducing exfoliated GO with glucose	1205.8	–	–	[56]
FLG	Modified Hummers' method and then rapidly exfoliated at high temperatures under N_2 atmosphere	492.5	2.28	–	[61]
Functionalized graphene sheets	Hummers method and thermal exfoliation under air atmosphere	404.00	1.87	18.5	[67]
Functionalized graphene sheets	Hummers method followed by thermal exfoliation under air atmosphere and treated at 900 °C in N_2	737	3.63	19.7	[60]

The incorporation of nanoparticles and functional groups on the surface of graphene can increase their selectivity, sensitivity, and detection limit, which opens up new opportunities to further explore their potential application as nanoadsorbents to remove organic pollutants from water resources and to treat industrial wastewater containing synthetic dyes [6, 60]. Besides the textural and adjustable chemical properties, the large number of π electrons delocalized make the graphene extremely attractive for environmental decontamination applications [6].

As it is still difficult to obtain pure and individually isolated graphene sheets for large-scale applications, much attention has been diverted to their oxidized forms such as the GO and rGO [70].

The GO, which is composed of high-oxidized stacked graphene sheets, has also drawn the attention due to its unique properties [70]. This important material which can be used as a promising precursor graphene [71] can be obtained by various techniques such as top-down methods proposed by Brodie [72], Staudenmaier [73], and Hummer [74], and also by variations of these methods [71]. Such methods utilize graphite as precursor material and produce graphite oxide, which is exfoliated for the production of GO [52]. These techniques use graphite, which is oxidized with the aid of strong oxidizing acids as precursor material [71]. The oxidation of graphite breaks up the π-conjugation of the stacked graphene sheets into nanoscale graphitic sp^2 domains surrounded by highly disordered oxidized domains (sp^3 C–C) as well as defects of carbon vacancies [75].

The Brodie and Staudenmaier methods use hydrochloric acid, which releases chlorine dioxide, a highly toxic gas during the reaction. In addition, both methods require more than 24 h reactions. Moreover, a smaller quantity of gas can be released during the reaction suggested by Hummer, which uses sulfuric acid. Furthermore, this reaction terminates within so short a time as 2 h [71]. Taking into account the productivity and also the safety, Hummer method is considered the most suitable for the production of graphite oxide [71].

The GO has irregular edges, rough surface, and lots of crumpling resulted from the scrolling of GO sheets. On the surface of GO (see Fig. 2.5b), there is a large amount of functional oxygen-containing groups such as carboxyl groups (–COOH) and carbonyl (–C=O), located at the edges of the sheet, and epoxy groups (C–O–C), and hydroxyl (–OH), preferentially located in the basal plane [76]. As graphene, GO has also attracted considerable attention for applications such as nanoadsorbent due to their textural properties (Table 2.4), high water solubility, and functional groups containing oxygen. These functional groups are also responsible for the formation of stable aqueous colloid that is obtained through sonication [77]. In addition, these functional groups provide the GO high negative charge density and can provide reactive sites for the adsorption of a variety of adsorbates, especially those with a positive charge, for example, heavy metal ions [14, 78] and synthetic dyes [79], mainly cationic dyes [77]. Furthermore, because of its aromatic structure similar to the graphene, the GO can easily adsorb organic compounds such as antibiotics [80] and endocrine disrupting [81] on its surface due to interactions of the π–π stacking.

The smaller surface area of GO samples (Table 2.4) in comparison to graphene (Table 2.3) can be assigned to: (i) clusters of layers during the drying steps because of the inevitable attractions through van der Waals between each single

Table 2.4 Synthesis methods and textural properties of graphene oxide

Samples	Synthesis method	Surface area ($m^2\ g^{-1}$)	Pore volume ($cm^3\ g^{-1}$)	Average pore size (nm)	Reference
GO	Modified hummers	23.00	–	–	[82]
GO	Modified hummers	32.00	0.11	17.3	[83]
GO	Modified staudenmaier	8.80	–	–	[70]
GO nanosheets	Modified hummers	26.76	0.03	4.97	[84]
GO nanosheets	Modified hummers	39.5	–	–	[85]

sheet of GO and (ii) defects, such as vacancy and folded sheets [85]. Like graphene, the average pore diameter of GO (Table 2.4) indicates that this is a mesoporous material [82]. It is noteworthy that the method of production of GO can also affect the properties of textures obtained [83, 85].

The adsorption properties of the rGO also have recently been studied, and evaluated for environmental applications [77, 86, 87]. In fact, this nanomaterial has revealed an effective and low-cost alternative for water purification—treatment [77, 86, 87].

The rGO can be synthesized through top-down approaches such as chemical and thermal reduction of GO to reduce its oxygen content [52]. The chemical reduction method is based on preparation of a stable colloidal dispersion of GO sheet exfoliated followed by reduction with a variety of chemical means. The GO can be chemically reduced with the aid of hydrazine [88, 89], sodium borohydride [90, 91], hydroquinone [92], and dimethylhydrazine [76], among others. On the other hand, the thermal reduction of GO consists of heating it to high temperature under an inert gas atmosphere. Thermal treatment of GO at temperatures ranging from 300 to 1100 °C for a period as short as 30 s up to 2 h promotes the reduction and exfoliation of the oxide, producing graphene sheets thermally reduced [84, 93]. The microwave, photothermal, photochemical, and microbial/bacterial methods can also be used to reduce the GO [52].

The processes of reduction of GO result in the partial deoxygenation and also, the gradual decrease of the hydrophilic character of rGO, often leading to irreversible agglomeration [93, 94]. The rGO sample may also be prepared by hydrothermal process [95]. In this process, the pH value of the reaction solution influences directly the material properties, since the number of layers tends to decrease with increasing pH of the reaction solution [95]. Furthermore, the samples prepared at acidic pH tend to agglomerate [95].

With respect to the morphology and textural properties, rGO possess many defects, a high wrinkling degree, and some remaining functional groups containing oxygen (Fig. 2.4c) due to the reduction process [93, 94]. Such remaining functional groups can improve the dispersion of rGO in various organic solvents [71]. The surface functional groups of rGO also can be modified by well-known chemical reactions into other groups for further applications [96, 97].

The rGO has a wide surface area and also high amounts of micro and mesopores as shown in Table 2.5. These characteristics make the rGO a promising

Table 2.5 Synthesis methods and textural properties of reduced graphene oxide

Samples	Synthesis method	Surface area ($m^2\ g^{-1}$)	Pore volume ($cm^3\ g^{-1}$)	Average pore size (nm)	Reference
rGO	Modified hummers and hydrazine-reduced	487.00	–	–	[88]
rGO	Modified hummers, reduced by hydrothermal dehydration and acidic pH(~2)	265.20	–	–	[95]
rGO	Modified hummers, reduced by hydrothermal dehydration and neutral pH(~7)	342.90	–	–	[95]
rGO	Modified hummers, reduced by hydrothermal dehydration and basic pH(~10)	479.55	–	–	[95]
rGO	Modified hummers and reduced by pyrolysis	303.00	0.493	6.5	[64]
rGO	Modified hummers reduced by continuous thermal expansion machine at 1100 °C	400–600	–	0.8–1.3	[71]
rGO	Modified hummers, and thermal reduction	450–550	–	–	[66]
rGO	Modified hummers, reduced by thermal annealing at 300 °C	234.7	–	0.52	[93]
rGO	Modified hummers, reduced by thermal annealing at 400 °C	403.7	–	0.67	[93]
rGO	Modified hummers, reduced by thermal annealing at 600 °C	213.0/0	–	0.80	[93]

adsorbent for treatment of effluents containing radionuclides [87], oil and organic solvent [98], metallic ions [99, 100], and synthetic dyes [77, 86]. The π–π stacking between sp^2 regions of rGO and aromatic structure of dyes, as well as the electrostatic interactions between charged dye and the surface oxygen-containing groups of rGO may also assist in the adsorption of dyes [101]. When compared to its precursor GO, the rGO does not have as high negative surface charge which candidate this material to be an interesting adsorbent for anionic dyes [77]. In addition, rGO can have their adsorption properties easily regenerated [86].

2.3 Electronic and Optical Properties of Carbon Nanoadsorbents

Carbon Nanoadsorbents capability are greatly influenced by their potential to form π–π interactions and other charge-transfer induced mechanisms. In its turn, the π–π interactions and other charge transfer-induced mechanisms are affected by environmental conditions (pH and ionic strength), oxygen content, or doping of the carbon nanostructure, as well as the adsorbate specie nature (charge, presence of aromatic rings, etc.).

2.3.1 Effect of Electronic Properties in the Adsorption Capability

Fullerene, CNT, and graphene are known to exhibit charge-transfer interaction with diverse molecules. Raman spectroscopy is widely used to access information about characteristics of carbon nanomaterials, including molecular charge transfer in graphene or CNTs. The energy of the excitation light can be scanned to obtain Raman maps that can infer information about the adsorption of species onto carbon nanoadsorbents or its potential for it. Accordingly to the type of charge transfer between a given molecule and the CNTs or graphene (electron donor or acceptor induced mechanism), there would be a shift on G or 2D band frequencies between before and after contact with the specific molecule [102]. When electron donors species are adsorbed a shift of Raman G band position to lower frequency positions is observed, while once electron acceptors are adsorbed, it shifts to high frequency position [103]. The occurrence of charge transfer gives rise to mid-gap molecular levels with tuning of band gap region near Dirac point. Organic molecules containing aromatic rings can also modify the electronic structure of graphene through π–π interactions. Electron donor molecules interact selectively with semiconducting SWCNTs, while electron acceptor with metallic ones, giving rise to possible metal–semiconductor transitions.

For instance, π–π interactions (depend on number of aromatic rings, as well as size and shape of aromatic system and substitution units of molecules) were

reported as cause of enhance of sorption affinity of phenolic compounds on MWCNTs with the increase of number of aromatic rings [51]. Species and magnitude of interaction affects adsorption and they can be related to the polarity and charge distribution for example. Free electrons in CNTs make them possible to form strong chemical bonds with other radionuclides.

Environmental conditions such as pH and ionic strength can also affect the electronic states and thus interactions between given molecule or ion and the carbon nanospecie. At high pH (pH > pKa) the negative surface charge provides electrostatic interaction favorable for adsorbing cations, while the decrease of pH leads to neutralization of surface charge [13].

Metal/nonmetal doping also can affect CNT adsorption properties [13]. For instance, B- and N-doped decrease hydrogen molecular adsorption energy on CNTs. B-doped form an electron deficient structure and a coordination-like B–H bond would be formed with H adsorption. N-doped form an electron rich structure and decrease H atomic adsorption energy. It was reported that both N-doped and B-doped CNTs increased the Pt adsorption, but through different mechanisms. In the N-doped the increase of Pt adsorption was attributed to activation of nitrogen neighbor carbon atoms, while at the B-doped case, the enhancement was related to strong hybridization between Pt *d* orbital and boron *p* orbital.

2.3.2 Effect of Adsorption in the Optoelectronic Properties

The adsorption of atoms on SWCNTs can distort the structure of SWCNT causing also changes on its electronic states and metal to semiconductor or semiconductor to a semiconductor with different band gaps can be achieved [104]. As it can be expected, tube–molecule distance can significantly affect partial charge of C atom and its gap energy [105]. Significant changes in the density of states (DOS) near Fermi level can render potential candidates for sensor applications, for instance. While low binding energies (<0.5 eV) suggest that the type of interaction is most likely physisorption, high binding energies can cause significant changes of electronic states around Fermi energy for both zigzag and armchair of the SWCNT after interaction with a given specie [106]. For instance, semiconducting Zigzag SWCNTs transform into metals upon adsorption of Ti. In general, the *d* orbitals of the transition metal atoms are responsible for relatively higher binding energies, which cause a change of the number of filled *d* states [107].

However, sometimes even strong adsorption (chemisorption) of some molecules is unable to render dramatic changes in the density of states near the Fermi level [108].

Photoluminescence imaging was already used to image exciton quenching in semiconducting SWCNT [109]. Additionally, depending on changes of Fermi level and DOS near the Fermi level, adsorption of a given molecule can affect the field emission current from CNT tips [110]. If the adsorption of a given molecule causes the Fermi level shifts toward the conduction band, one can expect that the

field emission current would increase if DOS becomes available near the Fermi level, but this not occurs if there is no available state near the Fermi level.

Photocurrent measurements can also be used to probe the adsorbed gas molecules in carbon nanoadsorbents [111]. If molecules are adsorbed on CNTs, optically excited carriers interact with the molecules and affect the decay time of the persistent current. For instance, CNT DOS is sensitive to the adsorption of NO_2, with a peak close to the CNT valence band maximum, leading to a p-type conductivity that can be detected by an increase of electrical response of the CNT film upon NO_2 exposure [112].

2.4 Concluding Remarks

As shown in this chapter, carbon nanomaterials can play an important role in water treatment—purification. These nanomaterials, such as fullerene, CNT, and graphene family have extremely interesting structure, morphology and adsorption properties, which make them promising for industrial use as nanoadsorbents, with elevated affinity, capacity, and selectivity.

Acknowledgments The authors acknowledge funding from Brazilian agencies Conselho Nacional de Desenvolvimento Científico e Tecnológico - CNPq and INCT Nanomateriais de Carbono.

References

1. Novoselov KS, Geim AK, Morozov SV et al (2004) Electric field effect in atomically thin carbon films. Science 306:666–669
2. Iijima S, Ichihashi T (1993) Single-shell carbon nanotubes of 1-nm diameter. Nature 363:603–605
3. Bethune DS, Klang CH, De Vries MS et al (2003) Cobalt-catalysed growth of carbon nanotubes with single-atomic-layer walls. Nature 363:605–607
4. Iijima S (1991) Helical microtubules of graphitic carbon. Nature 354:56–58
5. Kroto HW, Heath JR, Obrien SC, Curl RF, Smalley RE (1985) C_{60}: buckminsterfullerene. Nature 318:162–163
6. Chowdhury S, Balasubramanian R (2014) Recent advances in the use of graphene-family nanoadsorbents for removal of toxic pollutants from wastewater. Adv Colloid Interface Sci 204:35–56
7. Gupta VK, Saleh TA (2013) Sorption of pollutants by porous carbon, carbon nanotubes and fullerene - An overview. Environ Sci Pollut Res 20:2828–2843
8. Terronesa M, Botello-Méndezb AR, Campos-Delgadoc J et al (2010) Graphene and graphite nanoribbons: morphology, properties, synthesis, defects and applications. Nano Today 5(4):351–372
9. Serp P, Corrias M, Kalck P (2003) Carbon nanotubes and nanofibers in catalysis. Appl Catal A Gen 253:337–358
10. Agnihotri S, Mota JPB, Rostam-Abadi M, Rood MJ (2006) Structural characterization of single-walled carbon nanotube bundles by experiment and molecular simulation. Langmuir 21:896–904

11. Babaa MR, Dupont-Pavlovsky N, McRae E, Masenelli-Varlot K (2004) Physical adsorption of carbon tetrachloride on as-produced and on mechanically opened single walled carbon nanotubes. Carbon 42:1549–1554
12. Machado FM, Bergmann CP, Lima EC et al (2012) Adsorption of reactive blue 4 dye from water solutions by carbon nanotubes: experiment and theory. Phys Chem Chem Phys 14:11139–11153
13. Ren X, Chen C, Nagatsu M, Wang X (2011) Carbon nanotubes as adsorbents in environmental pollution management: a review. Chem Eng J 170:395–410
14. Ren X, Li J, Tan X, Wang X (2013) Comparative study of graphene oxide, activated carbon and carbon nanotubes as adsorbents for copper decontamination. Dalton Trans 42:5266–5274
15. Inagaki M, Kang F (2014) Materials science and engineering of carbon: fundamentals, 2nd edn. Elsevier, Oxford
16. Krätschmer W, Lamb LD, Fostiropoulos K, Huffman DR (1990) Solid C_{60}: a new form of carbon. Nature 347:354–358
17. Howard JB, Lafleur AL, Makarovsky Y, Mitra S, Pope CJ, Yadav TK (1992) Fullerenes synthesis in combustion. Carbon 30:1183–1201
18. Yoshida T, Tani T, Nishimura H, Akashi K (1983) Characterization of a hybrid plasma and its application to a chemical synthesis. J Appl Phys 54:640–646
19. Wang C, Imahori T, Tanaka Y, Sakuta T, Takikaw H, Matsuo H (2001) Synthesis of fullerenes from carbon powder by using high power induction thermal plasma. Thin Solid Films 390:31–36
20. Pan B, Lin D, Mashayekhi H, Xing B (2008) Adsorption and hysteresis of bisphenol a and 17#-Ethinyl estradiol on carbon nanomaterials. Environ Sci Technol 42(15):5480–5485
21. Silva SAM, Pereza J, Torresia RM, Luengob CA, Ticianellia EA (1999) Surface and electrochemical investigations of a fullerene soot. Electrochim Acta 44:3565–3574
22. Meng Z-D, Zhu L, Ullah K, Ye S, Oh W-C (2014) Detection of oxygen species generated by WO_3 modification fullerene/TiO_2 in the degradation of 1,5-diphenyl carbazide. Mater Res Bull 56:45–53
23. Papirer E, Brendle E, Ozil F, Balard H (1999) Comparison of the surface properties of graphite, carbon black and fullerene samples, measured by inverse gas chromatography. Carbon 37:1265–1274
24. Meng Z-D, Zhang F-J, Zhu L (2012) Synthesis and characterization of M-fullerene/TiO_2 photocatalysts designed for degradation azo dye. Mater Sci Eng C 32:2175–2182
25. Apostolopoulou V, Vakros J, Kordulis C, Lycourghiotis A (2009) Preparation and characterization of [60] fullerene nanoparticles supported on titania used as a photocatalyst. Colloids Surf A 349:189–194
26. Ballesteros E, Gallego M, Valcarcel M (2000) Analytical potential of fullerene as adsorbent for organic and organometallic compounds from aqueous solutions. J Chromatogr 869:101–110
27. Yang K, Zhu L, Xing B (2006) Adsorption of polycyclic aromatic hydrocarbons by carbon nanomaterials. Environ Sci Technol 40:1855–1861
28. Cheng X, Kan AT, Tomson MB (2005) Uptake and sequestration of naphthalene and 1,2-dichlorobenzene by C_{60}. J Nanoparticle Res 7:555–567
29. Berezkin VI, Viktorovski LV, Vul AY (2002) A comparative study of the sorption capacity of activated charcoal, soot, and fullerenes for organochlorine compounds. Tech Phys Lett 28:885–888
30. O'Connell JM (ed) (2006) Carbon nanotubes properties and applications. CRC Press, New York
31. Yang C-M, Kaneko K, Yudasaka M, Iijima S (2002) Surface chemistry and pore structure of purified HiPco single-walled carbon nanotube aggregates. Phys B 323:140–142
32. Niu JJ, Wang JN, Jiang Y, Su LF, Ma J (2007) An approach to carbon nanotubes with high surface area and large pore volume. Microporous Mesoporous Mater 100:1–5
33. Li F, Wang Y, Wang D, Wei F (2004) Characterization of single-wall carbon nanotubes by N_2 adsorption. Carbon 42:2375–2383

34. Yang QH, Hou PX, Bai S, Wang MZ, Cheng HM (2001) Adsorption and capillarity of nitrogen in aggregated multi-walled carbon nanotubes. Chem Phys Lett 345:18–24
35. Upadhyayula VKK, Deng S, Mitchell MC, Smith GB (2009) Application of carbon nanotube technology for removal of contaminants in drinking water: a review. Sci Total Environ 408:1–13
36. Tanaike O, Futaba DN, Hata K, Hatori H (2009) Supercapacitors using pure single-walled carbon nanotubes. Carbon Lattes 10(2):90–93
37. Machado FM, Bergmann CP, Fernandes THM et al (2011) Adsorption of reactive red M-2BE dye from water solutions by multi-walled carbon nanotubes and activated carbon. J Hazard Mater 192:1122–1131
38. Rengaraj S, Jei-Won Y, Younghun K, Won-Ho K (2007) Application of Mg-mesoporous alumina prepared by using magnesium stearate as a template for the removal of nickel: kinetics, isotherm and error analysis. Ind Eng Chem Res 46:2834–2842
39. Tarun KN, Ashim KB, Sudip KD (2009) Adsorption of Cd(II) and Pb(II) from aqueous solutions on activated alumina. J Colloid Interface Sci 333:14–26
40. Pyrzynska K (2008) Carbon nanotubes as a new solid-phase extraction material for removal and enrichment of organic pollutants in water. Sep Purif Rev 37:372–389
41. Sze MFF, Lee VKC, McKay G (2008) Simplified fixed bed column model for adsorption of organic pollutants using tapered activated carbon columns. Desalination 218:323–333
42. Lu C, Liu C (2006) Removal of nickel(II) from aqueous solution by carbon nanotubes. J Chem Technol Biotechnol 81:1932–1940
43. Benny TH, Bandosz TJ, Wong SS (2008) Effect of ozonolysis on the pore structure, surface chemistry, and bundling of single walled carbon nanotubes. J Colloid Interface Sci 317:375–382
44. Yan C, Zou L, Short R (2013) Single-walled carbon nanotubes and polyaniline composites for capacitive deionization. Desalination 290:125–129
45. Kang J, Wen J, Jayaram SH, Wang X, Chen S-K (2013) Electrochemical characterization and equivalent circuit modeling of single-walled carbon nanotube (SWCNT) coated electrodes. J Power Sources 234:208–216
46. Liao Q, Sun J, Gao L (2008) Adsorption of chlorophenols by multi-walled carbon nanotubes treated with HNO_3 and NH_3. Carbon 46:544–561
47. Lu C, Su F (2007) Adsorption of natural organic matter by carbon nanotubes. Sep Purif Technol 58:113–121
48. Pillaya K, Cukrowska EM, Coville NJ (2009) Multi-walled carbon nanotubes as adsorbents for the removal of parts per billion levels of hexavalent chromium from aqueous solution. J Hazard Mater 166:1067–1075
49. Chen Y, Liu C, Li F, Cheng HM (2006) Pore structures of multi walled carbon nanotubes activated by air, CO_2 and KOH. J Porous Mater 13:141–146
50. Kayiran SB, Lamari DF, Levesque D (2004) Adsorption properties and structural characterization of activated and nano-carbons. J Phys Chem B 108:15211–15215
51. Chin C-JM, Shih M-W, Tsai H-J (2010) Adsorption of nonpolar benzene derivatives on single-walled carbon nanotubes. Appl Surf Sci 256(20):6035–6039
52. Bianco A, Cheng H-M, Enoki T et al (2013) All in the graphene family—a recommended nomenclature for two-dimensional carbon materials. Carbon 65:1–6
53. Sun Y, Wu Q, Shi G (2011) Graphene based new energy materials. Energy Environ Sci 4:1113–1132
54. Hernandez Y, Nicolosi V, Lotya M et al (2008) High-yield production of graphene by liquid-phase exfoliation of graphite. Nat Nanotechnol 3:563–568
55. Negishi R, Hirano H, Ohno Y, Maehashi K, Matsumoto K, Kobayashi Y (2011) Layer-by-layer growth of graphene layers on graphene substrates by chemical vapor deposition. Thin Solid Films 519:6447–6452
56. Park J, Mitchel WC, Grazulis L et al (2010) Epitaxial graphene growth by carbon molecular beam epitaxy (CMBE). Adv Mater 22:4140–4145
57. Seresht RJ, Jahanshahi M, Rashidi A, Ghoreyshi AA (2013) Synthesize and characterization of graphene nanosheets with high surface area and nano-porous structure. Appl Surf Sci 276:672–681

58. Yuan W, Li B, Li L (2011) A green synthetic approach to graphene nanosheets for hydrogen adsorption. Appl Surf Sci 257:10183–10187
59. Stoller MD, Park S, Zhu Y, An J, Ruoff RS (2008) Graphene-based ultracapacitors. Nano Lett 8:3498–3502
60. Liu T, Li Y, Du Q et al (2012) Adsorption of methylene blue from aqueous solution by graphene. Colloid Surf B 90:197–203
61. Lian P, Zhu X, Liang S, Li Z, Yang W, Wang H (2010) Large reversible capacity of high quality graphene sheets as an anode material for lithium-ion batteries. Electrochim Acta 55:3909–3914
62. Li H, Zou L, Pan L, Sun Z (2010) Using graphene nano-flakes as electrodes to re-move ferric ions by capacitive deionization. Sep Purif Technol 75:8–14
63. Geng D, Yang S, Zhang Y et al (2011) Nitrogen doping effects on the structure of graphene. Appl Surf Sci 257:9193–9198
64. Zang J, Qian H, Wei Z et al (2014) Reduced graphene oxide supported MnO nanoparticles with excellent lithium storage performance. Electrochim Acta 118:112–117
65. Zhang L, Ji B, Wang K, Song J (2014) Synthesis of nitrogen-doped graphene via solid microwave method. Mater Sci Eng B 185:129–133
66. Krishnan D, Kim F, Luo J et al (2012) Energetic graphene oxide: challenges and opportunities. Nano Today 7:137–152
67. Du Q, Zheng M, Zhang L et al (2010) Preparation of functionalized graphene sheets by a low-temperature thermal exfoliation approach and their electrochemical supercapacitive behaviors. Electrochim Acta 55:3897–3903
68. Zhu Y, Murali S, Cai W et al (2010) Graphene and graphene oxide: synthesis, properties, and applications. Adv Mater 22(35):3906–3924
69. Ma LP, Wu ZS, Li J, Wu ED, Ren WC, Cheng HM (2009) Hydrogen adsorption behavior of graphene above critical temperature. Int J Hydrogen Energy 34:2329–2332
70. Tsoufis T, Tuci G, Caporali S, Gournis D, Giambastiani G (2013) *p*-Xylylenediamine intercalation of graphene oxide for the production of stitched nanostructures with a tailored interlayer spacing. Carbon 59:100–108
71. Lee S, Eom SH, Chung JS, Hur SH (2013) Large-scale production of high-quality reduced graphene oxide. Chem Eng J 233:297–304
72. Brodie BC (1859) On the atomic weight of graphite. Philos Trans R Soc London Ser A 149:249–259
73. Staudenmaier L (1898) Verfahren zur darstellung der graphitsaure. Ber Deut Chem Ges 31:1481–1487
74. Hummers WS, Offeman RE (1958) Preparation of graphitic oxide. J Am Chem Soc 80:1339
75. Terzopoulou Z, Kyzas GZ, Bikiaris DN (2015) Recent advances in nanocomposite materials of graphene derivatives with polysaccharides. Materials 8(2):652–683
76. Stankovich S, Dikin DA, Dommett GHB et al (2006) Graphene-based composite materials. Nature 442:282–286
77. Ramesha GK, Kumara AV, Muralidhara HB, Sampath S (2011) Graphene and graphene oxide as effective adsorbents toward anionic and cationic dyes. J Colloid Interface Sci 361:270–277
78. Mishra AK, Ramaprabhu S (2011) Removal of metals from aqueous solution and sea water by functionalized graphite nanoplatelets based electrodes. J Hazard Mater 185:322–328
79. Yang S-T, Chen S, Chang Y, Cao A, Liu Y, Wang H (2011) Removal of methylene blue from aqueous solution by graphene oxide. J Colloid Interface Sci 359:24–29
80. Gao Y, Zhang L, Huang H, Hu J, Shah S, Su X (2012) Adsorption and removal of tetracycline antibiotics from aqueous solution by graphene oxide. J Colloid Interface Sci 368:540–546
81. Xu J, Zhu Y-F (2013) Elimination of bisphenol A from water via graphene oxide adsorption. Acta Phys Chim Sin 29:829–836
82. Yang Q, Lia Q, Yan Z et al (2014) High performance graphene/manganese oxide hybrid electrode with flexible holey structure. Electrochim Acta 129:237–244

83. Li Y, Du Q, Wang J et al (2013) Defluoridation from aqueous solution by manganese oxide coated graphene oxide. J Fluorine Chem 148:67–73
84. Lee Y-C, Chang S-J, Choi M-H, Jeon T-J, Ryu T, Huh YS (2013) Self-assembled graphene oxide with organo-building blocks of Fe-aminoclay for heterogeneous fenton-like reaction at near-neutral pH: a batch experiment. Appl Catal B 142–143:494–503
85. Sun G, Zheng L, Zhan Z, Zhou J, Liu X, Li L (2014) Actuation triggered exfoliation of graphene oxide at low temperature for electrochemical capacitor applications. Carbon 68:748–754
86. Tiwari JN, Mahesh K, Le NH et al (2013) Reduced graphene oxide-based hydrogels for the efficient capture of dye pollutants from aqueous solutions. Carbon 56:173–182
87. Pan N, Deng J, Guan D, Jin Y, Xia C (2013) Adsorption characteristics of Th(IV) ions on reduced graphene oxide from aqueous solutions. Appl Surf Sci 287(2013):478–483
88. Park S, An J, Potts JR, Velamakanni A, Murali S, Ruoff RS (2011) Hydrazine-reduction of graphite- and graphene oxide. Carbon 49:3019–3023
89. Guo H-L, Wang X-F, Qian Q-Y, Wang F-B, Xia X-H (2009) A green approach to the synthesis of graphene nanosheets. ACS Nano 3:2653–2659
90. Chua CK, Martin Pumera M (2013) Reduction of graphene oxide with substituted borohydrides. J Mater Chem A 1:1892–1898
91. Si Y, Samulski ET (2008) Synthesis of water soluble graphene. Nano Lett 8:1679–1682
92. Wang G, Yang J, Park J et al (2008) Facile synthesis and characterization of graphene nanosheets. J Phys Chem C 112:8192–8195
93. Kim JM, Hong WG, Lee SM et al (2014) Energy storage of thermally reduced graphene oxide. Int J Hydrogen Energ 39:3799–3804
94. Liu S, Chen K, Fu Y, Yu S, Bao Z (2012) Reduced graphene oxide paper by supercritical ethanol treatment and its electrochemical properties. Appl Surf Sci 258:5299–5303
95. Bai Y, Rakhi RB, Chen W, Alshareef HN (2013) Effect of pH-induced chemical modification of hydrothermally reduced graphene oxide on supercapacitor performance. J Power Sources 233:313–319
96. Feng R, Zhou W, Guan G et al (2012) Surface decoration of graphene by grafting polymerization using graphene oxide as the initiator. J Mater Chem 22:3982–3989
97. Bourlinos AB, Gournis D, Petridis D, Szabó T, Szeri A, Dékány I (2003) Graphite oxide: chemical reduction to graphite and surface modification with primary aliphatic amines and amino acids. Langmuir 19:6050–6055
98. Bi H, Xie X, Yin K et al (2012) Spongy graphene as a highly efficient and recyclable sorbent for oils and organic solvents. Adv Funct Mater 22:4421–4425
99. Wang YK, Gao ST, Ma JJ, Li JC (2012) Application of graphene as a sorbent for simultaneous preconcentration and determination of trace amounts of cobalt and nickel in environmental water and vegetable samples. J Chin Chem Soc 59:1468–1477
100. Wang Y, Gao S, Zang X, Li J, Ma J (2012) Graphene-based solid phase extraction combined with flame atomic absorption spectrometry for a sensitive determination of trace amounts of lead in environmental water and vegetable samples. Anal Chim Acta 716:112–118
101. Bai S, Shen X, Zhu G et al (2013) The influence of wrinkling in reduced graphene oxide on their adsorption and catalytic properties. Carbon 60:157–168
102. Das B, Voggu R, Rout CS, Rao CNR (2008) Changes in the electronic structure and properties of graphene induced by molecular charge-transfer. Chem Commun 5155–5157
103. Rao CN, Voggu R (2010) Charge-transfer with graphene and nanotubes. Mater Today 13:34–40
104. Yang X, Ni J (2005) Metal-semiconductor and semiconductor-semiconductor transitions in carbon nanotubes induced by intercalating alkali atoms. Phys Rev B 71:165438-1–165438-5
105. Rafati AA, Hashemianzaded SM, Nojini ZB (2008) Electronic properties of adsorption nitrogen monoxide on inside and outside of the armchair single wall carbon nanotubes: a density functional theory calculations. J Phys Chem C 112:3597–3604
106. Yang C-K, Zhao J, Lu JP (2002) Binding energies and electronic structures of adsorbed titanium chains on carbon nanotubes. Phys Rev B 66:041403(R)

107. Durgun E, Dag S, Bagci VMK, Gülseren O, Yildirim T, Ciraci S (2003) Systematic study of adsorption of single atoms on a carbon nanotube. Phys Rev B 67:201401(R)
108. An W, Turner CH (2009) Electronic structure calculations of gas adsorption on boron-doped carbon nanotubes sensitized with tungsten. Chem Phys Lett 482:274–280
109. Crochet JJ, Duque JD, Werner JH, Doorn SK (2012) Photoluminescence imaging of electronic-impurity-induced exciton quenching in single-walled carbon nanotubes. Nat Nanotechnol 7:126–132
110. Kim C, Choi YS, Lee SM, Park JT, Kim B, Lee YH (2002) The effect of gas adsorption on the field emission mechanism of carbon nanotubes. J Am Chem Soc 124:9906–9911
111. Kang D, Park C, Park N, Park W (2008) Photocurrent measurements of carbon nanotube networks with physical adsorption of oxygen molecules. J Korean Phys Soc 53:3343–3347
112. Santucci S, Picozzi S, Di Gregorio F et al (2003) NO_2 and CO gas adsorption on carbon nanotubes: Experiment and theory. J Chem Phys 119:10904–10910

Chapter 3
Kinetic and Equilibrium Models of Adsorption

Éder Cláudio Lima, Matthew Ayorinde Adebayo and Fernando Machado Machado

Abstract In adsorption study, isotherms and kinetics of adsorption process provide pieces of information underlying the mechanisms and dynamics of the process. Several equilibrium and kinetic models are usually employed for performing the experimental design of an adsorption system. In this chapter, the Langmuir, Freundlich, Sips, Liu, Redlich–Peterson nonlinear equations, as well as other unusual isotherm models (Hill, Khan, Radke–Prausnitz, Toth) are discussed. For the kinetics of adsorption, the pseudo-first-order, pseudo-second-order, general-order, Avrami fractionary order, and Elovich chemisorption models are explained. The importance of statistical parameters such as coefficient of determination (R^2), adjusted coefficient of determination (R^2_{adj}), and standard deviation (root of mean square error) are highlighted. The usage of linearized and nonlinearized equations are illustrated and explained. Some common mistakes commonly committed in the literature using linearized equilibrium and kinetic adsorption models as well as other polemic points in adsorption research are pointed out. Analytical techniques together with thermodynamical data of enthalpy and entropy changes are needed to ascertain if an adsorption process is a chemical or a physical process.

É.C. Lima (✉)
Instituto de Química, Universidade Federal do Rio Grande do Sul,
Porto Alegre, RS 91501970, Brazil
e-mail: profederlima@gmail.com

M.A. Adebayo
Department of Chemistry, Federal University of Agriculture,
Abeokuta 110008, Ogun State, Nigeria
e-mail: adebayomao@gmail.com

F.M. Machado
Centro de Desenvolvimento Tecnológico, Universidade Federal de Pelotas,
Pelotas, RS 96010610, Brazil
e-mail: fernando.machado@hotmail.com.br

C.P. Bergmann and F.M. Machado (eds.), *Carbon Nanomaterials as Adsorbents for Environmental and Biological Applications*, Carbon Nanostructures,
DOI 10.1007/978-3-319-18875-1_3

Keywords Nonlinear equilibrium and kinetic adsorption models · Thermodynamic calculation of enthalpy and entropy changes · Distribution constant · Equilibrium constant · Temperature values

Abbreviations

DB-53	Direct Blue 53
DOF	Degree of freedom
FTIR	Fourier transform infrared
MWCNT	Multi-walled carbon nanotube
SWCNT	Single-walled carbon nanotube
RB-4	Reactive Blue 4
RO-16	Reactive Orange-16
R	Correlation coefficient
R^2	Coefficient of determination
R^2_{adj}	Adjusted coefficient of determination
SD	Standard deviation (root of mean square error)
TGA	Thermogravimetric analysis
q_e	Adsorption capacity at the equilibrium (mg g^{-1}) or amount adsorbed by the adsorbent at the equilibrium
q_t	Amount adsorbed by the adsorbent at any time (mg g^{-1})
C_e	Concentration of the adsorbate at the equilibrium (mg L^{-1})
C_o	Initial adsorbate concentration (mg L^{-1})
Q_{max}	Maximum amount adsorbed (mg g^{-1})
K_L	Langmuir equilibrium constant (L mg^{-1})
K_F	The Freundlich equilibrium constant (mg g^{-1}(mg $L^{-1})^{-1/n}$)
n_F	The Freundlich exponent (dimensionless)
K_S	The Sips equilibrium constant (mg $L^{-1})^{-1/ns}$
n_S	The Sips exponent (dimensionless)
K_g	The Liu equilibrium constant (L mg^{-1})
n_L	Dimensionless exponent of the Liu equation
K_{RP}	Redlich–Peterson constants (L g^{-1})
a_{RP}	Redlich–Peterson constant (mg $L^{-1})^{-g}$
g	The Redlich–Peterson exponent (dimensionless)
K_H	The Hill equilibrium isotherm constant [(mg $L^{-1})^{nH}$]
n_H	The Hill exponent (dimensionless)
K_K	The Khan equilibrium isotherm constant (L mg^{-1})
n_K	The Khan exponent (dimensionless)
K_{RAP}	The Radke–Prausnitz equilibrium isotherm constant (L mg^{-1})
n_{RP}	The Radke–Prausnitz exponent (dimensionless)
K_T	The Toth equilibrium isotherm constant (L mg^{-1})
n_T	The Toth exponent (dimensionless)
dq	Differential of q (adsorption capacity)

dt	Differential of time
k_f	The pseudo-first-order rate constant (min^{-1})
t	Contact time (min)
k_s	The pseudo-second-order rate constant (g mg^{-1} min^{-1})
h_o	Initial sorption rate (mg g^{-1} min^{-1})
k_N	The rate constant for the order N
n	The order of adsorption with respect to the effective concentration of the adsorption active sites present on the surface of adsorbent
θ_t	Number of the active sites available on the surface of adsorbent for adsorption
α	The initial adsorption rate (mg g^{-1} min^{-1})
β	Related to the extent of surface coverage and the activation energy involved in chemisorption (g mg^{-1})
k_{AV}	The Avrami kinetic constant (min^{-1})
n_{AV}	Is a fractional adsorption order
k_{id}	The intraparticle diffusion rate constant (mg g^{-1} $min^{-0.5}$)
C	A constant related to the thickness of boundary layer (mg g^{-1})
A	The Arrhenius constant
E_a	Is the activation energy (kJ mol^{-1})
R	The universal gas constant (8.314 J K^{-1} mol^{-1})
T	The absolute temperature (K)
K_D	The distribution equilibrium constant (dimensionless)

3.1 Introduction

At a constant temperature, an adsorption isotherm describes the relationship between the amount of adsorbate adsorbed by the adsorbent (q_e) and the adsorbate concentration remaining in solution after equilibrium is reached (C_e). The parameters from the adsorption equilibrium models provide useful pieces of information on the surface properties, adsorption mechanism and interaction between the adsorbent and adsorbate. There are numerous equations for describing the adsorption equilibrium of an adsorbate on an adsorbent. The most employed and discussed in the literature is the Langmuir equation [1]. Other isotherm models such as Freundlich isotherm [2], Sips isotherm [3], Liu isotherm [4], Redlich–Peterson isotherm [5] are also well discussed in the literature.

Adsorption kinetic studies are important in treatment of aqueous effluents because they provide valuable information on the mechanism of the adsorption process. Many kinetic models were developed in order to find intrinsic kinetic adsorption constants. In this chapter we will discuss the adsorption kinetic models based on the chemical reaction (pseudo-first order equation [6], pseudo-second-order equation [7], general-order equation [8]), and the empiric models (Avrami fractionary model [9], and Elovich chemisorption model [9]).

3.2 Equilibrium Isotherm Models

3.2.1 Langmuir Isotherm Model

The Langmuir [1] isotherm is based on the following assumptions:

- adsorbates are chemically adsorbed at a fixed number of well-defined sites;
- a monolayer of the adsorbate is formed over the surface of the adsorbent when it gets saturated;
- each site can hold only one adsorbate species;
- all sites are energetically equivalent;
- interactions between the adsorbate species do not exist.

The Langmuir isotherm equation is depicted by Eq. 3.1:

$$q_e = \frac{Q\max \cdot K_L \cdot C_e}{1 + K_L \cdot C_e} \tag{3.1}$$

where q_e is the amount of adsorbate adsorbed at the equilibrium (mg g^{-1}), C_e is the supernatant adsorbate concentration at the equilibrium (mg L^{-1}), K_L is the Langmuir equilibrium constant (L mg^{-1}), and Q_{max} is the maximum adsorption capacity of the adsorbent (mg g^{-1}) assuming a monolayer of adsorbate uptake by the adsorbent.

It is pertinent to use an example to describe the Langmuir model. Figure 3.1 presents the data of adsorption of Direct Blue 53 (DB-53) onto multi-walled carbon nanotubes (MWCNT) adsorbent [10]. In this section of the chapter, only nonlinear equations will be considered. An explanation for this will be given at the subsequent sections in the chapter, which will show the main problems that occur with the linearization of equilibrium and kinetic models of adsorption. Figure 3.1,

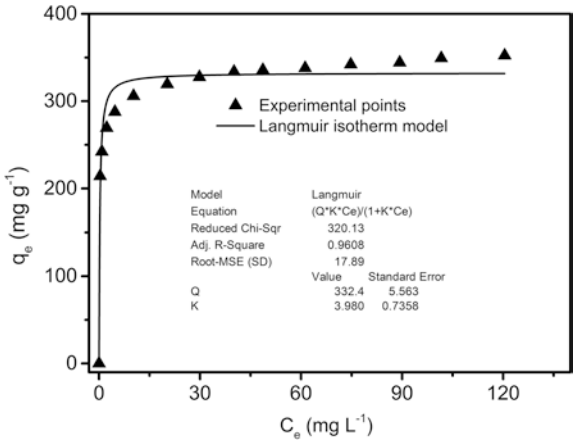

Fig. 3.1 Langmuir adsorption equilibrium isotherm of DB-53 dye using MWCNT at 50 °C and pH 2.0

therefore, shows the nonlinearized Langmuir isotherm plot for the adsorption of DB-53 dye using MWCNT as adsorbent [10].

The R^2_{adj} for nonlinear Langmuir isotherm was 0.9608, the Q_{max} was 332.4 mg g^{-1} and the Langmuir equilibrium constant was 3.980 L mg^{-1}. The total standard deviation (SD-root of mean square error) of the fitting was 17.89 mg g^{-1}.

3.2.2 Freundlich Isotherm Model

Freundlich [2] isotherm model is an exponential equation, and assumes that the concentration of adsorbate on the adsorbent surface increases as the adsorbate concentration increases. Theoretically, using this expression, an infinite amount of adsorption will occur. Similarly, the model assumes that the adsorption could occur via multiple layers instead of a single layer. The equation has a wide application in heterogeneous systems. Equation 3.2 shows the Freundlich isotherm model;

$$q_e = K_F \cdot C_e^{1/n_F} \tag{3.2}$$

where K_F is the Freundlich equilibrium constant (mg g^{-1}(mg L^{-1})$^{-1/n}$), and n_F is the Freundlich exponent (dimensionless). Figure 3.2 shows the nonlinearized Freundlich isotherm plot for the adsorption of DB-53 dye using MWCNT as adsorbent [10].

The R^2_{adj} for nonlinear Freundlich isotherm was 0.9946 while the Freundlich equilibrium constant was 249.1 (mg g^{-1}(mg L^{-1})$^{-1/n_F}$). The total SD of the fitting was 13.21 mg g^{-1}. When compared with Langmuir isotherm, the Freundlich isotherm model with R^2_{adj} is closer to unity and a lower SD presented a better fit.

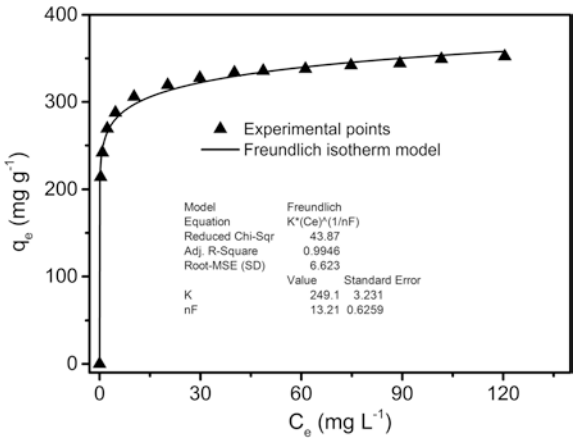

Fig. 3.2 Freundlich adsorption equilibrium isotherm of DB-53 dye using MWCNT at 50 °C and pH 2.0

3.2.3 Sips Isotherm Model

Sip model, an empirical model, consists of the combination of the Langmuir and Freundlich isotherm models. The Sips [3] model takes the following form:

$$q_e = \frac{Q\max \cdot K_S \cdot C_e^{1/n_S}}{1 + K_S \cdot C_e^{1/n_S}} \quad \text{where } 0 < 1/n_s \leq 1 \tag{3.3}$$

In Eq. 3.3, K_S is the Sips equilibrium constant $(\text{mg L}^{-1})^{-1/n}$, Q_{max} is the Sips maximum adsorption capacity (mg g^{-1}), and n_S is the exponent. It is assumed that the $1/n_S$ should be ≤ 1 for integration purpose [3].

Although several works in the literature using Sips isotherm really do not take into account this consideration. The nonlinearized Sips isotherm curve for the adsorption of DB-53 dye using MWCNT as adsorbent is shown in Fig. 3.3 [10].

At low adsorbate concentrations, Sips equation relatively reduces to the Freundlich isotherm, but it predicts a monolayer adsorption capacity characteristic of the Langmuir isotherm at high adsorbate concentrations.

It was observed that the Sips exponent was restricted to 1 [3], in this manner, this isotherm model has the same parameters as the Langmuir isotherm, however, the R^2_{adj} and the SD of the Sips isotherm were worse than those of the Langmuir isotherm. In that case, when $n_s = 1$, the Langmuir expression is preferred because the Sips isotherm has three parameters while Langmuir isotherm has just two. This parametric difference worsens the values of R^2_{adj} and SD of the Sips isotherm. More details of the statistical analysis (reduced chi-squared; SD; coefficient of determination—R^2 and Adjusted coefficient of determination—R^2_{adj}) will be provided later in this chapter after the kinetic models.

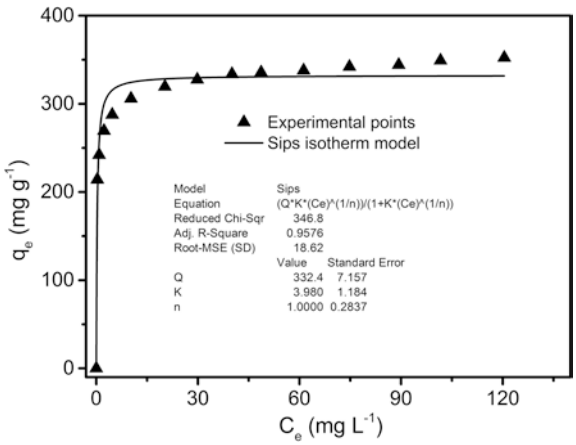

Fig. 3.3 Sips adsorption equilibrium isotherm of DB-53 dye using MWCNT at 50 °C and pH 2.0

3.2.4 Liu Isotherm Model

The Liu isotherm model [4] is a combination of the Langmuir and Freundlich isotherm models, but the monolayer assumption of Langmuir model and the infinite adsorption assumption that originates from the Freundlich model are discarded. The Liu model predicts that the active sites of the adsorbent cannot possess the same energy.

Therefore, the adsorbent may present active sites preferred by the adsorbate molecules for occupation [4], however, saturation of the active sites should occur unlike in the Freundlich isotherm model. Equation 3.4 defines the Liu isotherm model.

$$q_e = \frac{Q\max \cdot \left(K_g \cdot C_e\right)^{n_L}}{1 + \left(K_g \cdot C_e\right)^{n_L}} \tag{3.4}$$

where K_g is the Liu equilibrium constant (L mg^{-1}); n_L is dimensionless exponent of the Liu equation, and Q_{max} is the maximum adsorption capacity of the adsorbent (mg g^{-1}). Contrary to the Sips isotherm, n_L could assume any positive value.

Figure 3.4 shows the nonlinearized Liu isotherm plot for the adsorption of DB-53 dye using MWCNT as adsorbent [10].

From the fit, the R^2_{adj} obtained was 0.9998, which is very good for a nonlinear isotherm. Similarly, the SD for Liu isotherm model was only 1.143 mg g^{-1}. This value was 15.65, 11.56, and 16.29 times lower than the SD values of Langmuir, Freundlich, and Sips isotherms models, respectively, indicating that this isotherm model was a better fit to the experimental equilibrium data [10]. The advantages of Liu isotherm model (a 3-parameter isotherm) over the Sips isotherm model is that the exponent of Liu isotherm could admit any positive value unlike the exponent of Sips that is limited to $1/n \leq 1$.

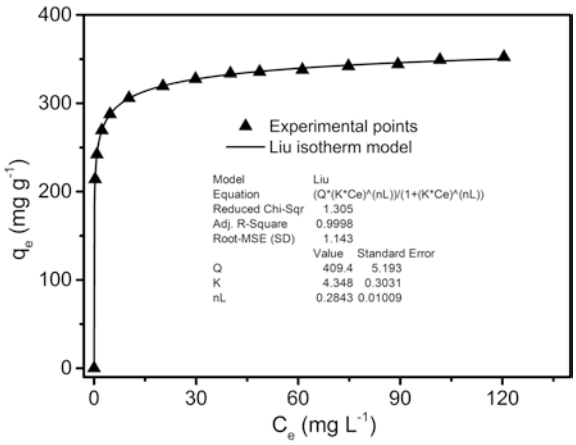

Fig. 3.4 Liu adsorption equilibrium isotherm of DB-53 dye using MWCNT at 50 °C and pH 2.0

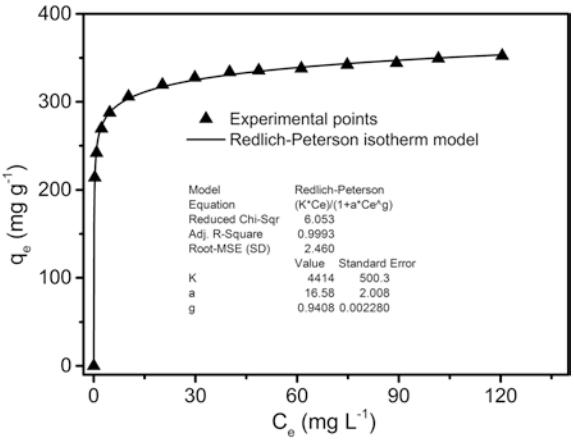

Fig. 3.5 Redlich–Peterson adsorption equilibrium isotherm of DB-53 dye using MWCNT at 50 °C and pH 2.0

3.2.5 Redlich–Peterson Isotherm Model

This is an empirical equation that describes an equilibrium isotherm as shown in Eq. 3.5 [5].

$$q_e = \frac{K_{RP} \cdot C_e}{1 + a_{RP} \cdot C_e^g} \quad \text{where} \quad 0 < g \leq 1 \tag{3.5}$$

where K_{RP} and a_{RP} are Redlich–Peterson constants with the respective units of L g^{-1} and (mg L^{-1})$^{-g}$, and g is the Redlich–Peterson exponent (dimensionless) whose value should be ≤ 1. This equation becomes linear at a low surface coverage ($g = 0$) and reduces to a Langmuir isotherm when $g = 1$. Figure 3.5 presents the nonlinearized Redlich–Peterson isotherm curve for the adsorption of DB-53 dye using MWCNT as adsorbent [10].

The R^2_{adj} and the SD obtained with the Redlich–Peterson model were better than those of Langmuir, Freundlich, and Sips isotherm models, being just a little bit worse than the Liu isotherm model. This model has three parameters, and the exponent is limited to ≤ 1.

3.2.6 Other Unusual Isotherm Models

Apart from equilibrium models commonly described in the literature, there are other models that can be used to describe how an adsorbate is adsorbed onto an adsorbent [11, 12]. Mathematical expressions of some of these adsorption equilibrium models are given in Table 3.1 [11, 12].

Table 3.1 Unusual equilibrium adsorption isotherms

Isotherm	Equation	Parameters
Hill	$q_e = \frac{Q\max \cdot C_e^n H}{KH + C_e^n H}$	– Q_{max} is the maximum sorption capacity (mg g^{-1}) – K_H is the Hill equilibrium isotherm constant [(mg L^{-1})^{nH}] – n_H is the Hill exponent (dimensionless)
Khan	$q_e = \frac{Q\max \cdot K_K \cdot C_e}{(1+K_K \cdot C_e)^{n_k}}$	– Q_{max} is the maximum sorption capacity (mg g^{-1}) – K_K is the Khan equilibrium isotherm constant (L mg^{-1}) – n_K is the Khan exponent (dimensionless)
Radke–Prausnitz	$q_e = \frac{Q\max \cdot K_{RAP} \cdot C_e}{(1+K_{RAP} \cdot C_e)^{1/n_{RP}}}$	– Q_{max} is the maximum sorption capacity (mg g^{-1}) – K_{RAP} is the Radke–Prausnitz equilibrium isotherm constant (L mg^{-1}) – n_{RP} is the Radke–Prausnitz exponent (dimensionless)
Toth	$q_e = \frac{Q\max \cdot K_T \cdot C_e}{[1+(K_T \cdot C_e)^{1/n_T}]^{n_T}}$	– Q_{max} is the maximum sorption capacity (mg g^{-1}) – K_T is the Toth equilibrium isotherm constant (L mg^{-1}) – n_T is the Toth exponent (dimensionless)

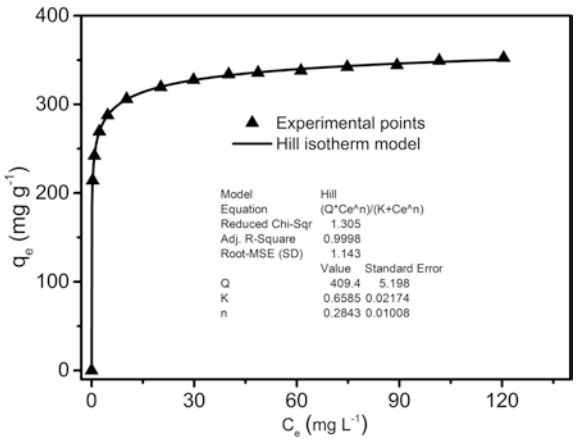

Fig. 3.6 Hill adsorption equilibrium isotherm of DB-53 dye using MWCNT at 50 °C and pH 2.0

Figures 3.6, 3.7, 3.8, and 3.9 shows the nonlinearized isotherms of Hill, Khan, Radke–Prausnitz, and Toth, respectively, for the adsorption of DB-53 dye using MWCNT as adsorbent [10].

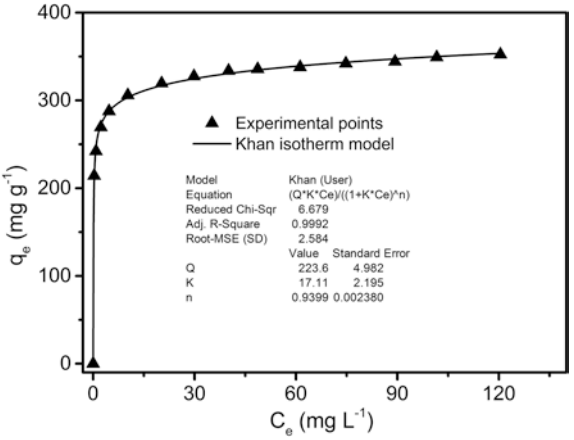

Fig. 3.7 Khan adsorption equilibrium isotherm of DB-53 dye using MWCNT at 50 °C and pH 2.0

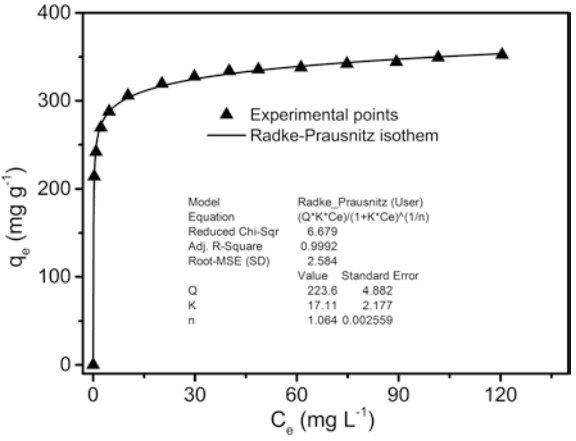

Fig. 3.8 Radke–Prausnitz adsorption equilibrium isotherm of DB-53 dye using MWCNT at 50 °C and pH 2.0

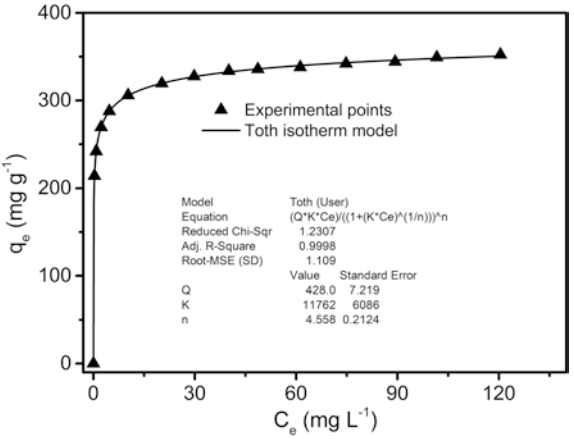

Fig. 3.9 Toth adsorption equilibrium isotherm of DB-53 dye using MWCNT at 50 °C and pH 2.0

3.2.7 General Comments About the Isotherm Models

Examining all the set of isotherm parameters, the R^2_{adj} as well as the SD, it is observed that Liu and Hill isotherm models are identical, except for their equilibrium constants ($K_L \neq K_H$). The Liu isotherm is actually derived from Hill isotherm model [4]. The R^2_{adj}, SD and the isotherm parameters for Khan isotherm model and Radke–Prausnitz are also similar. Therefore, there is no significant difference in the Khan and Radke–Prausnitz isotherm models. The only difference between these two equations (see Table 3.1) is the exponent ($n_K = 1/n_{RP}$). This observation confirms that several isotherms that are reported in the literature are exactly the same isotherm model with slightly differences. The Toth isotherm model has the lowest value of SD of all the nine models described in this chapter (Langmuir, Freudlich, Sips, Liu, Redlich–Peterson, Hill, Khan, Radke–Prausnitz, and Toth). Mathematically, Toth is the best fit isotherm model. On the other hand, the value of the equilibrium constant and the value of maximum amount adsorbed may not correspond to the correct values. An examination of just one temperature value may not provide a realistic conclusion. It is necessary to use different isotherm models with different temperature values. The model with the best values of R^2_{adj} and the lowest values of SD for the majorities of temperature values should be taken as the best isotherm model to describe the adsorption behavior of an adsorbate on a given adsorbent. The Khan and Radke–Prausnitz isotherm models are three-parameter isotherm models, whose parameter values are completely different from other isotherm models; however, they exhibited good values of R^2_{adj} and SD. Therefore, according to the authors' experience, the statistical analysis is to guide the adsorption researcher to employ a good isotherm model; however, it is necessary to check if the obtained parameters have physical meaning, and also verify the behavior of each isotherm model at different temperature values. Based on the nine values of the parameters, and the experience of the authors, the best results are the Liu and the Hill isotherm values, where the maximum sorption capacity of the adsorbent was 409.4 mg g^{-1} for adsorption of DB-53 dye onto MWCNT [10]. The complete analysis of different isotherms for the same adsorbent and adsorbate [10] intends to attract the attention of the reader to use different isotherm models (Liu, Sips, Redlich–Peterson, besides Langmuir and Freundlich) for explaining the equilibrium data obtained in the laboratory during adsorption experiment. Another critical issue is that some isotherm models present equilibrium constant values and maximum sorption capacities that do not sometimes correspond to the actual values of these parameters.

3.3 Kinetic Adsorption Models

3.3.1 Kinetic Models Based on the Order of Reaction

The study of adsorption kinetic is important in the treatment of aqueous effluents using nanomaterials because it provides valuable pieces of information on the reaction pathways and the mechanism of adsorption reactions.

Many kinetic models were developed to evaluate the intrinsic kinetic adsorption constants. Traditionally, the kinetics of adsorption of an adsorbate is described using the expressions originally given by Lagergren [6]. A simple kinetic analysis of adsorption is the pseudo-first-order equation in the form of Eq. 3.6:

$$\frac{dq}{dt} = k_f \cdot (q_e - q_t) \tag{3.6}$$

where q_t is the amount of adsorbate adsorbed at time t (mg g^{-1}), q_e is the equilibrium adsorption capacity (mg g^{-1}), k_f is the pseudo-first-order rate constant (min^{-1}), and t is the contact time (min). The integration of Eq. 3.6 with initial conditions, $q_t = 0$ at $t = 0$, and $q_t = q_t$ at $t = t$ leads to Eq. 3.7:

$$\ln(q_e - q_t) = \ln(q_e) - k_f \cdot t \tag{3.7}$$

A nonlinear rearrangement of Eq. 3.7 gives Eq. 3.8:

$$q_t = q_e \cdot \left[1 - \exp\left(-k_f \cdot t\right)\right] \tag{3.8}$$

Equation 3.8 is known as pseudo-first-order kinetic adsorption model.

In addition, a pseudo-second-order equation [7] based on equilibrium adsorption capacity is shown in Eq. 3.9:

$$\frac{dq_t}{dt} = k_s \cdot (q_e - q_t)^2 \tag{3.9}$$

where, k_s is the pseudo-second-order rate constant (g mg^{-1} min^{-1}). The integration of Eq. 3.9 with initial conditions, $q_t = 0$ at $t = 0$, and $q_t = q_t$ at $t = t$ leads to Eq. 3.10:

$$q_t = \frac{k_s \cdot q_e^2 \cdot t}{1 + q_e \cdot k_s \cdot t} \tag{3.10}$$

Equation 3.10 is known as pseudo-second-order kinetic adsorption model.

The initial sorption rate (h_o, expressed in mg g^{-1} min^{-1}) can be obtained when t approaches zero [13] as shown in Eq. 3.11:

$$h_o = k_s \cdot q_e^2 \tag{3.11}$$

The pseudo-first-order and pseudo-second-order are the most commonly employed kinetic models for describing adsorption process based on chemical reactions kinetic. Another approach to this theme is described below.

The exponents of rate laws of chemical reactions are usually independent of the coefficients of chemical equations, but are sometimes related. This assertion implies that the order of a chemical reaction depends solely on the experimental data. Adsorption process, which is considered to be the rate determining step, helps in establishing the general rate law equation of adsorption process [12, 14]. Attention is now focused on the change in the effective number of active sites at the surface of adsorbent during adsorption instead of concentration of adsorbate in the bulk solution. Applying reaction rate law to Eq. 3.12 gives adsorption rate expression.

$$\frac{dq}{dt} = k_N \cdot (q_e - q_t)^n \tag{3.12}$$

where k_N is the rate constant, q_e is the amount of adsorbate adsorbed by adsorbent at equilibrium, q_t is the amount of adsorbate adsorbed by adsorbent at a given time, t, and n is the order of adsorption with respect to the effective concentration of the adsorption active sites present on the surface of adsorbent [8]. Application of universal rate law to adsorption process led to Eq. 3.12, which can be used without assumptions. Theoretically, the exponent n in Eq. 3.12 can be an integer or noninteger rational number [8, 12, 14].

Equation 3.13 describes the number of the active sites (θ_t) available on the surface of adsorbent for adsorption [12, 14].

$$\theta_t = 1 - \frac{q_e}{q_t} \tag{3.13}$$

Equation 3.14 describes the relationship between the variable (θ_t) and rates of adsorption.

$$\frac{d\theta_t}{dt} = -k\theta_t^n \tag{3.14}$$

where $k = k_N(q_e)^{n-1}$. $\theta_t = 1$ if an adsorbent has not adsorbed. The value of θ_t decreases during adsorption process. θ_t approaches a fixed value when adsorption process reaches equilibrium. $\theta_t = 0$ for a saturated adsorbent [8]. Equation 3.14 gives Eq. 3.15 after integration:

$$\int_1^{\theta} \frac{d\theta_t}{\theta_t^n} = -k \int_0^t dt \tag{3.15}$$

Equation 3.15 also gives Eq. 3.16:

$$\frac{1}{1-n} \cdot \left[\theta_t^{1-n} - 1\right] = -kt \tag{3.16}$$

Rearrangement of Eq. 3.16 gives Eq. 3.17.

$$\theta_t = [1 - k(1-n) \cdot t]^{1/1-n} \tag{3.17}$$

Substituting Eq. 3.13 into Eq. 3.17, and put $k = k_N(q_e)^{n-1}$ yields Eq. 3.18.

$$q_t = q_e - \frac{q_e}{\left[k_N(q_e)^{n-1} \cdot t \cdot (n-1) + 1\right]^{1/1-n}} \tag{3.18}$$

Equation 3.18 is regarded as the general-order kinetic equation of adsorption process, which is valid for $n \neq 1$ [8]. A special case of Eq. 3.14 is the pseudo-first-order kinetic model ($n = 1$) [12, 14].

$$\frac{d\theta_t}{dt} = -k\theta_t^1 \tag{3.19}$$

Integration of Eq. 3.19 gives Eq. 3.20.

$$\theta_t = \exp\left(-k \cdot t\right) \tag{3.20}$$

Substitution of Eq. 3.13 into Eq. 3.20, and put $k = k_1$ gives pseudo-first-order kinetic model as shown in Eq. 3.21.

$$q_t = q_e\left[1 - \exp\left(-k_1 \cdot t\right)\right] \tag{3.21}$$

Pseudo-first-order kinetic equation is a special case of general kinetic model of adsorption. It must be noted that Eq. 3.21 is the same as Eq. 3.8 using the adsorption rate expression. When $n = 2$, the pseudo-second-order kinetic model is a special case of Eq. 3.18 [8].

$$q_t = q_e - \frac{q_e}{\left[k_2(q_e) \cdot t + 1\right]} \tag{3.22}$$

Equation 3.22 on rearrangement gives Eq. 3.23.

$$q_t = \frac{q_e^2 k_2 t}{\left[k_2(q_e) \cdot t + 1\right]} \tag{3.23}$$

Equation 3.23 is the pseudo-second-order kinetic adsorption model, which is exactly the same as Eq. 3.10. Therefore, the general-order adsorption Eq. 3.18 could give rise to pseudo-second-order when $n = 2$, while the pseudo-first order is obtained from Eq. 3.12 (adsorption rate expression).

3.3.2 Empiric Models

The Elovich equation is generally applied to chemisorption kinetics [9]. The equation has been used satisfactorily for some chemisorption processes [15] and has been found to cover a wide range of slow adsorption rates. The same equation is often valid for systems in which the adsorbing surface is heterogeneous. The Elovich equation is given in Eq. 3.24.

$$\frac{\mathrm{d}q_t}{\mathrm{d}t} = \alpha \exp(-\beta q_t) \tag{3.24}$$

Integrating Eq. 3.24 using boundary conditions; $q_t = 0$ at $t = 0$ and $q_t = q_t$ at $t = t$ gives Eq. 3.25:

$$q_t = \frac{1}{\beta}\ln\left(t + t_o\right) - \frac{1}{\beta}\ln\left(t_o\right) \tag{3.25}$$

where α is the initial adsorption rate (mg g^{-1} min^{-1}) and β is related to the extent of surface coverage and the activation energy involved in chemisorption (g mg^{-1}) and $t_o = 1/\alpha\beta$.

If t is much larger than t_o, the kinetic equation can be simplified as Eq. 3.26.

$$q_t = \frac{1}{\beta} \ln (\alpha \cdot \beta) + \frac{1}{\beta} \ln (t) \tag{3.26}$$

Equation 3.26 is known as Elovich–chemisorption kinetic adsorption model.

The determination of some kinetic parameters, possible changes of the adsorption rates as function of the initial concentration and the adsorption time as well as the determination of fractional kinetic orders, still lacks in the kinetic adsorption models [16]. In this way, an alternative Avrami kinetic equation to find a correlation between good experimental and calculated data was early proposed [16]. The adsorption should now be visualized using Avrami's exponential function, which is an adaptation of kinetic thermal decomposition modeling [16].

$$\alpha = 1 - \exp\left[(-k_{\mathrm{AV}} \cdot t)\right]^{n_{\mathrm{AV}}} \tag{3.27}$$

where α is adsorption fraction (q_t/q_e) at time t, k_{AV} is the Avrami kinetic constant (min^{-1}), and n_{AV} is a fractional adsorption order, which is related to the adsorption mechanism [16]. By inputting α in Eq. 3.27, the Avrami kinetic equation could be written as Eq. 3.28.

$$q_t = q_e \cdot \left\{1 - \exp\left[-(k_{\mathrm{AV}} \cdot t)\right]^n\right\} \tag{3.28}$$

After describing the pseudo-first order, pseudo-second-order, general-order, Elovich chemisorption, and Avrami fractionary order equations, we will illustrate these models using nonlinear fit of the data. Figure 3.10 shows the pseudo-first-order kinetic curve of the Reactive Blue 4 dye (RB-4) using SWCNT as adsorbent at pH 2.0 and 25 °C [17].

Figure 3.11 presents the pseudo-second-order kinetic plot of the RB-4 dye using SWCNT as adsorbent at pH 2.0 and 25 °C [17].

The general-order kinetic curve of the RB-4 dye using SWCNT as adsorbent at pH 2.0 and 25 °C is presented in Fig. 3.12 [17].

Figure 3.13 presents the Elovich Chemisorption kinetic plot of the RB-4 dye using SWCNT as adsorbent at pH 2.0 and 25 °C [17].

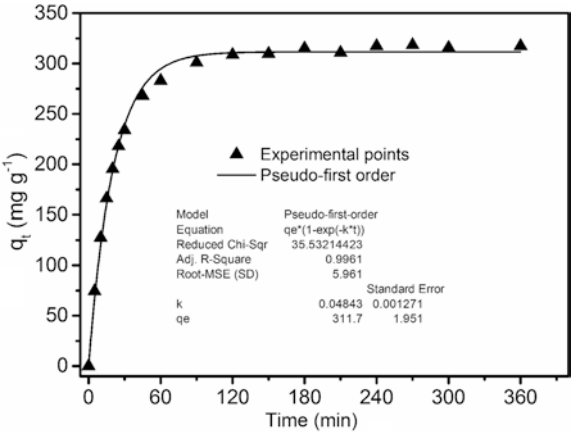

Fig. 3.10 Pseudo-first-order kinetic adsorption model of RB-4 dye using SWCNT. Initial pH, 2.0; temperature, 25 °C; initial concentration of the adsorbate, 800.0 mg L^{-1}

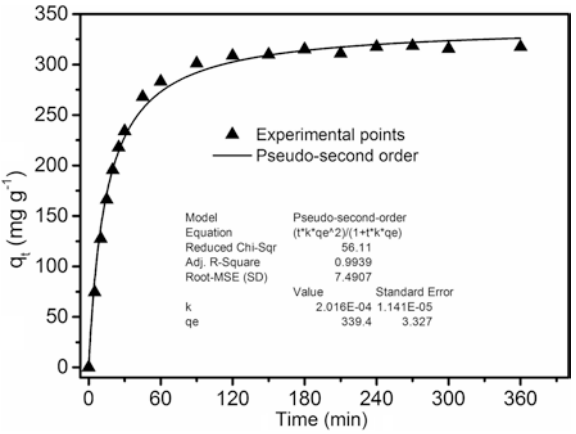

Fig. 3.11 Pseudo-second-order kinetic adsorption model of RB-4 dye using SWCNT. Initial pH, 2.0; temperature, 25 °C; initial concentration of the adsorbate, 800.0 mg L^{-1}

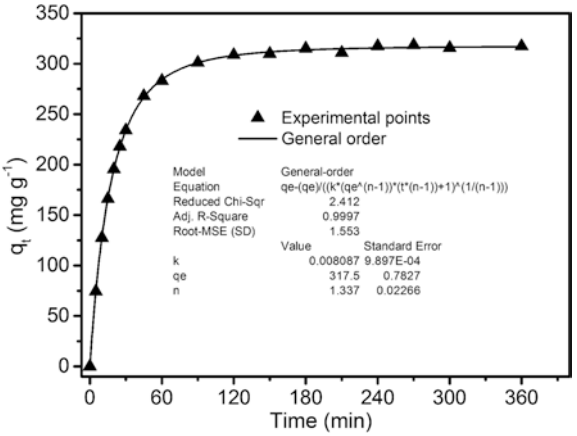

Fig. 3.12 General-order kinetic adsorption model of RB-4 dye using SWCNT. Initial pH, 2.0; temperature, 25 °C; initial concentration of the adsorbate, 800.0 mg L^{-1}

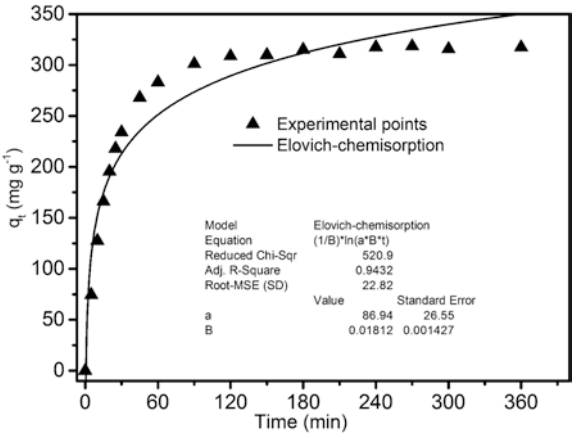

Fig. 3.13 Elovich chemisorption kinetic adsorption model of RB-4 dye using SWCNT. Initial pH, 2.0; temperature, 25 °C; initial concentration of the adsorbate, 800.0 mg L^{-1}

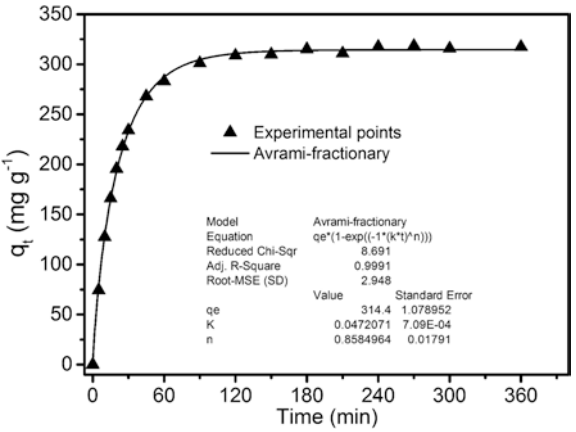

Fig. 3.14 Avrami fractionary kinetic adsorption model of RB-4 dye using SWCNT. Initial pH, 2.0; temperature, 25 °C; initial concentration of the adsorbate, 800.0 mg L^{-1}

Figure 3.14 shows the Avrami-fractional kinetic plot of the RB-4 dye using SWCNT as adsorbent at pH 2.0 and 25 °C [17].

Figures 3.10, 3.11, 3.12, 3.13, and 3.14 present kinetic curves of the adsorption of RB-4 dye onto SWCNT adsorbent [17] for pseudo-first-order, pseudo-second-order, general-order, Elovich chemisorption, and Avrami fractionary models, respectively. The best fit model is the one with the lowest value of SD and the one in which the value of R^2_{adj} is closer to unity. Equations 3.29–3.32 depict the expressions of reduced chi-square, SD, R^2, and R^2_{adj}, respectively.

$$\text{Reduced Chi-squared} = \sum_{i}^{n} \frac{\left(q_{i,\text{exp}} - q_{i,\text{model}}\right)^2}{n_\text{p} - p} \tag{3.29}$$

$$\text{SD} = \sqrt{\left(\frac{1}{n_\text{p} - p}\right) \cdot \sum_{i}^{n} \left(q_{i,\text{exp}} - q_{i,\text{model}}\right)^2} \tag{3.30}$$

$$R^2 = \left[\frac{\sum_i^{\text{np}} \left(q_{i,\text{exp}} - \bar{q}_\text{exp}\right)^2 - \sum_i^{\text{np}} \left(q_{i,\text{exp}} - q_{i,\text{model}}\right)^2}{\sum_i^{n} \left(q_{i,\text{exp}} - \bar{q}_\text{exp}\right)^2}\right] \tag{3.31}$$

$$R^2_{\text{adj}} = 1 - \left(1 - R^2\right) \cdot \left(\frac{n_\text{p} - 1}{n_\text{p} - p - 1}\right) \tag{3.32}$$

where q_i, model is each value of q predicted by the fitted model, $q_{i,\text{ exp}}$ is each value of q measured experimentally, $\bar{q}_\text{exp}$ is the average of q experimentally measured, n_p is the number of experiments performed, and p is the number of parameters of the fitted model.

The reduced chi-square is the residual sum of squares divided by the degree of freedom (DOF) (np-p) (Eq. 3.29). The SD is the square root of reduced chi squared (Eq. 3.30). Both Eqs. 3.29 and 3.30 are very useful for evaluation of point to point of a given kinetic or equilibrium adsorption model, this is because for each experimental point there is a point in the model that corresponds exactly to the point on the curve (model). The lower the reduced chi-square and the SD, the lower the difference between the values of experimental q and theoretical q; therefore, the best fit is expected. However, it should be taken into account that it is not possible to compare the values of reduced chi-squared and SD among several kinetic and equilibrium isotherms that present other different concentrations or other conditions since the values of SD and chi-square tend to increase as the concentration increases. On the contrary, for the same set of experimental data, the values of reduced chi-square and SD are useful to ascertain the best model since R^2 and R^2_{adj} are of low sensitivity (their values are limited to unity) [18].

The R^2 and R^2_{adj} in Eqs. 3.31 and 3.32, respectively, are very useful parameters to evaluate kinetic and equilibrium adsorption fits. Limitedly, their values are between 0 and 1. Values of R^2 and R^2_{adj} that are closer to 1 means that the model has a better fit. It is important to note that $\bar{q}_{exp}$ of Eq. 3.31 is the average of all experimental data (q). If the range of q values is too large, $\bar{q}_{i,exp}$ could distort the interpretation of the fit. If there is equidistant values of $q_{i,exp}$ from the average value, the values of R^2 tend to 1. Therefore, the analysis of a kinetic and equilibrium isotherm could not only be based on the values of R^2 [18]. In the same way, comparison of two-parameter models (pseudo-first order, pseudo-second-order, Elovich chemisorption) with three-parameter models (general order, Avrami fractionary order) is not possible because the equations with higher number of parameters have the tendency to exhibit R^2 values closer to 1. In these cases, it is recommended to use R^2_{adj} [18]. This statistical parameter is used to penalize the models with more parameters in order to really know if the best fitting (R^2_{adj}) is due to the advantage of presenting more terms in the equation (mathematical advantage), or alternatively, the equation is physically closer to the reality of the system. R^2_{adj} is, therefore, a very good parameter for evaluating a given kinetic and equilibrium of adsorption [18].

Based on the explanation above, we really recommend evaluation of SD and R^2_{adj} to decide the best fitting model. In addition, it should be stressed that it is necessary to interpret the values of the obtained parameters to really know if the model is a suitably fitting model, as it was done in the adsorption equilibrium studies described above. For the graphs depicted in Figs. 3.10, 3.11, 3.12, 3.13, and 3.14, the general-order kinetic adsorption model (the best fitting model) showed the lowest values of SD, and the highest values of R^2_{adj}. Sequentially, Avrami fractionary kinetic model was the second best kinetic model followed by pseudo-first order (third best fitting model), pseudo-second-order (4th), and then the Elovich chemisorption model (5th). Taking into consideration that the general-order kinetic of adsorption model was the best fitting model, its parameters can now be discussed. The capacity of adsorption at equilibrium (q_e) is 317.5 mg g^{-1}, which is closer to the values of saturation attained in the Fig. 3.13. The kinetic

adsorption rate constant is $8.087.10^{-3}$ ($min^{-1}(g\ mg^{-1})^{0.337}$) and the order of kinetic model (n) is 1.337. What could be the reason for n not being 1 (pseudo-first order) or 2 (pseudo-second-order)? The order should be determined experimentally and not as previously stipulated as described above. The fractional number could be a change in the order of kinetic adsorption that took place during the adsorption process. Similarly, it was observed that pseudo-first-order kinetic model gave a better fit than pseudo-second-order. This phenomenon could be analyzed in the following way: 1.337 is closer to 1 (0.337) than 2 (0.663). Therefore, an n value of 1.337 could also be attributed to a change in the kinetics of adsorption, changing from pseudo-first-order to pseudo-second-order during the contact of the adsorbate with the adsorbent. Therefore, the general-order kinetic model represents a more detailed mechanism of adsorption between the adsorbent and adsorbate, when a change in the order of kinetic process is possible to occur during the adsorption process. This assertion explains why fractional numbers are obtained as the orders of adsorption processes.

3.3.3 Diffusive Mechanisms

The process of sorption falls into four basic stages: (1) transport of the adsorbate from the bulk solution to the film of solvent around the particles of the adsorbent, usually this stage is too fast for agitated systems, (2) diffusive mass transfer of the adsorbate through the film, (3) intraparticle diffusion of the adsorbate through the pores of the adsorbent, (4) binding of the adsorbate to the active sites in the pores of the adsorbent [19], this stage is usually faster than the diffusion of the adsorbate by the film and intraparticle diffusion; therefore, it is assumed that this stage does not limit mass transfer.

The possibility of intraparticle diffusion resistance affecting adsorption process could be explored using the intraparticle diffusion model as given in Eq. 3.33 [20]:

$$q_t = k_{id} \cdot \sqrt{t} + C \tag{3.33}$$

where q_t is the amount of adsorbate adsorbed by adsorbent at a given time, t (min), k_{id} is the intraparticle diffusion rate constant (mg g^{-1} $min^{-0.5}$), and C is a constant related to the thickness of boundary layer (mg g^{-1}) [20]. In order to illustrate the intraparticle diffusion, Fig. 3.15 presents the Weber-Morris intraparticle kinetic plot of the RB-4 dye using SWCNT as adsorbent at pH 2.0 and 25 °C [17].

The intraparticle diffusion constant, k_{id} (mg g^{-1} $min^{-0.5}$), can be obtained from the slope of the plot of q_t versus the square root of time. Figure 3.15 shows the plot of q_t versus $t^{1/2}$, with multilinearity for RB-4 dye using SWCNT adsorbent. These results imply that the adsorption process involves more than a single kinetic stage (or adsorption rate) [17]. The adsorption process showed three zones which could be attributed to each linear portion as shown in Fig. 3.15. The first linear portion (1st zone) was assigned to the diffusional process of the dye on the adsorbent surface [17]; hence, it was the fastest sorption stage. The second portion (2nd zone)

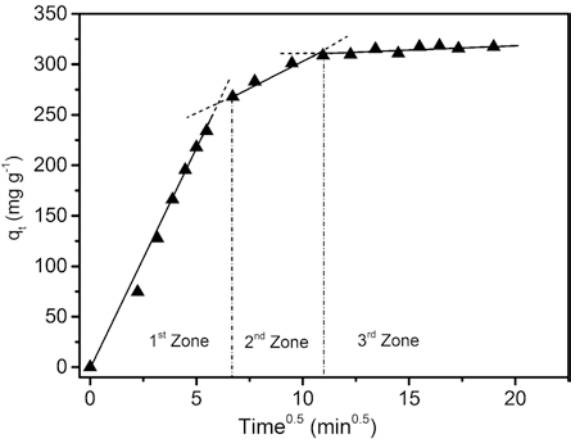

Fig. 3.15 Weber-Morris intraparticle kinetic adsorption curve of RB-4 dye using SWCNT. Initial pH, 2.0; temperature, 25 °C; initial concentration of the adsorbate, 800.0 mg L^{-1}

was ascribed to intraparticle diffusion, a delayed process [17]. The third stage (3rd zone) could be regarded as the diffusion through smaller pores, which is followed by the establishment of equilibrium [17]. From the slope of the linear portion of the second zone it was possible to determine k_{id} which is 9.583 mg g^{-1} $min^{-0.5}$.

3.4 Problems with the Linearization of Equilibrium and Kinetic Equations Usually Employed in the Adsorption Studies

The misuse of linearization is probably the most common error in data analysis of adsorption studies. It was largely used some decades ago when computers and statistical software were not available. Presently, linearization in data analysis is on the increase because the authors usually employ the simplest tool to analyze their experimental data. One of the reasons for using linear equations is the possibility of performing less experimental points to define a line (that is the major problem of using nonlinear equations, which require more experimental points to define a curve) or alternatively, discard some points to increase the R^2 values. The main problem is that some points are discarded to increase the R^2 values, and the authors are not concerned about the values of the parameters of the equilibrium and kinetic of adsorption models.

There are problems associated with linearizing an inherently nonlinear equation using various transformations. The main concern when transforming data to obtain a linearized equation is the knowledge of the error structure of the data and how this structure is affected by the mathematical manipulation of the data [21]. Linearization is based on the fact that the variance of all q values (Y variable of the graph; dependent variable; amount of adsorbate adsorbed by the adsorbent) is equal for all range of the data. By assuming homoscedasticity of the data

(assuming equal variance for all q values throughout the range of the data) when it is actually heteroscedastic (the variance of all q values are not equal in the full range of the data), may result in overestimating the goodness of fit as measured by the correlation coefficient (R), which translates into error in the coefficient of determination (R^2) and also in the adjusted coefficient of determination [21]. Therefore, higher R^2 values do not necessarily mean better fit of the experimental data.

In practice, authors have to delete some points from their curves to justify the linearization procedure. This adjustment decreases the DOF of the fitting model, which consequently decreases the number of independent ways by which a dynamic system can move without violating any constraint imposed on it. The DOF can be defined as the minimum number of independent coordinates that can specify the position of a system completely. In order to make it clear to the readers, some case studies will be discussed below.

3.4.1 Equilibrium Isotherms

We start with the equilibrium isotherms. Taking into account that the majority of the published articles used the Langmuir model, this equilibrium model will be given extensive study in this chapter.

Let us consider the adsorption of RB-4 dye on SWCNT at 308 K [17]. According to Kumar 2007 [22], there are four linearized equations of the Langmuir as presented in Table 3.2.

Let us also consider the following experimental data [17] as depicted on Table 3.3.

It should be noted that in manipulating the parameters the parametric units changed, and this change is not considered by many authors. The nonlinear isotherm directly uses experimental data: concentrations of the RB-4 left in the supernatant after adsorption process (abscissa axis) and the amount adsorbed (ordinate axis), which were calculated according to Eq. 3.34:

$$q = \frac{(C_o - C_f)}{m} \cdot V \tag{3.34}$$

Table 3.2 Langmuir equilibrium isotherms

Isotherm model	Linear form	Plot
$q_e = \frac{Q\max \cdot K_L \cdot C_e}{1+K_L \cdot C_e}$ Langmuir	$\frac{C_e}{q_e} = \frac{1}{K_L \cdot Q\max} + \frac{1}{Q\max} C_e$ Langmuir-1	$\frac{C_e}{q_e}$ versus C_e
	$\frac{1}{q_e} = \frac{1}{Q\max} + \left(\frac{1}{K_L \cdot Q\max}\right) \frac{1}{C_e}$ Langmuir-2	$\frac{1}{q_e}$ versus $\frac{1}{C_e}$
	$q_e = Q\max - \left(\frac{1}{K_L}\right) \frac{q_e}{C_e}$ Langmuir-3	q_e versus $\frac{q_e}{C_e}$
	$\frac{q_e}{C_e} = K_L \cdot Q\max - K_L \cdot q_e$ Langmuir-4	$\frac{q_e}{C_e}$ versus q_e

Table 3.3 Experimental data of the adsorption of RB-4 on SWCNT at 308 K [17]

Experimental values		Manipulated values			
C_e (mg L^{-1})	q_e (mg g^{-1})	C_e/q_e (g L^{-1})	$1/q_e$ (g mg^{-1})	$1/C_e$ (L mg^{-1})	q_e/C_e (L g^{-1})
0.0000	0.0000	–	–	–	–
1.4533	316.6852	0.004589	0.003158	0.688089	217.9077
1.7050	330.2201	0.005163	0.003028	0.586510	193.6775
2.1329	350.6311	0.006083	0.002852	0.468845	164.3917
3.6110	392.1553	0.009208	0.002550	0.276932	108.6002
9.3290	449.3022	0.020763	0.002226	0.107193	48.16188
13.3310	467.5717	0.028511	0.002139	0.075013	35.07402
29.2659	494.3358	0.059202	0.002023	0.034169	16.89119
45.7345	510.2976	0.089623	0.001960	0.021865	11.15783
69.1810	509.7880	0.135705	0.001962	0.014455	7.368902
94.9172	506.9212	0.187243	0.001973	0.010535	5.340667
120.4673	522.7081	0.230468	0.001913	0.008301	4.339004
154.6583	519.8411	0.297511	0.001924	0.006466	3.361223
188.6690	520.4519	0.36251	0.001921	0.005300	2.758545

where q is the amount of adsorbate adsorbed by the adsorbent (mg g^{-1}), C_o is the initial adsorbate concentration in contact with the adsorbent (mg L^{-1}), C_f is the final adsorbate concentration after adsorption process (mg L^{-1}), m is the mass of adsorbent (g), and V is the volume of adsorbate solution (L).

The nonlinear, Langmuir-1, Langmuir-2, Langmuir-3, and Langmuir-4 linearized isotherms are presented in Fig. 3.16.

Table 3.4 presents the statistical analysis of all isotherms presented in Fig. 3.16. As can be observed, Langmuir-1 linearized equation was the only model that showed the best values of R^2 and R^2_{adj}, smaller SD, and reduced Chi-square and residual sum of squares, and with this model, it was not necessary to delete any manipulated point. However, for linearized Langmuir-2, linearized Langmuir-3, and linearized Langmuir-4, it was necessary to delete some data points to improve the statistical analysis. Usually, the authors are only worried about the value of R^2 but not concerned about the other statistical parameters. When the points on an isotherm are deleted, the slope and intercept of the plot will be modified, which will invariably affect the values of Q_{max}, and K_L, apart from decreasing the values of DOF. It should also be stressed that reduced Chi-square and SD altered the units of dependent variable (Y-axis). Only linearized Langmuir-3 equation presents the same units for the statistical parameters compared with nonlinear Langmuir equation. Therefore, it is not possible to infer that linearized Langmuir-1 equation provides more accurate results than nonlinear equation since all the statistical parameters (Chi-squared, SD, residual sum of squares) presented in Table 3.3 reflect different situations (Y-axis of each graph) for nonlinear and linearized Langmuir-1 equations. Considering the fact that the nonlinear fit is the best fitting method of equilibrium isotherm, the values of Q_{max} and K_L obtained by nonlinear

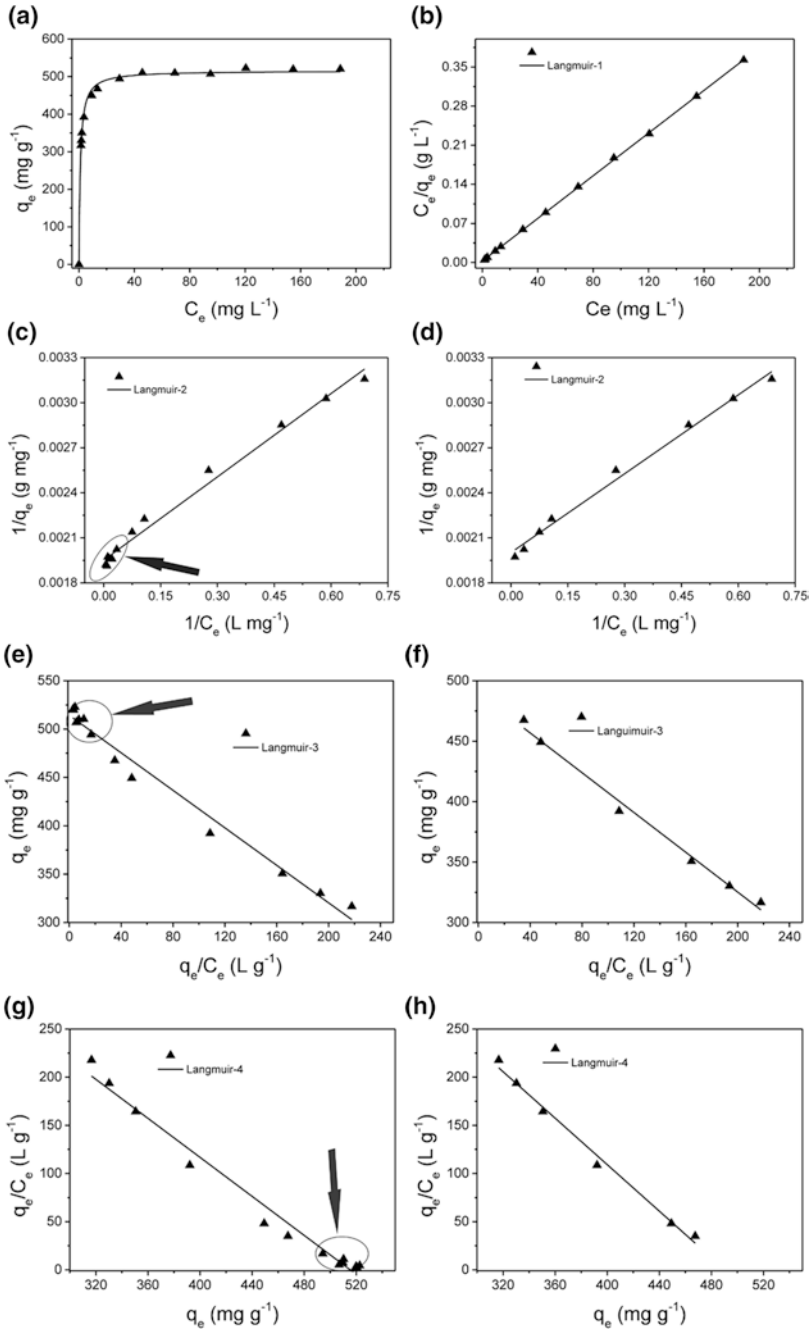

Fig. 3.16 **a** Nonlinearized Langmuir equation; **b** linearized Langmuir-1 equation; **c** linearized Langmuir-2 equation; **d** linearized Langmuir-2 equation after deleting some points; **e** linearized Langmuir-3 equation; **f** linearized Langmuir-3 equation after deleting some points; **g** linearized Langmuir-4 equation; **h** linearized Langmuir-4 equation after deleting some points. *Arrows* indicate the set of point that need to be deleted to improve the values of R^2

Table 3.4 Statistical analysis of data presented in Fig. 3.16

Parameter	Value	Parameter	Value
Nonlinear	Figure 3.16a	Langmuir-1	Figure 3.16b
Q_{max} (mg g^{-1})	515.8	Q_{max} (mg g^{-1})	523.7
K_L (L mg^{-1})	0.9966	K_L (L mg^{-1})	0.7252
Number of points	14	Number of points	13
Degrees of freedom	12	Degrees of freedom	11
Reduced Chi-Sqr (mg g^{-1})	84.13	Reduced Chi-Sqr (g L^{-1})	1.818×10^{-6}
Res. sum of squ. (mg $g^{-1})^2$	1009	Res. sum of squ. (g $L^{-1})^2$	1.999×10^{-5}
R (COC)	0.9981	R (COC)	0.9999
R^2 (COD)	0.9962	R^2 (COD)	0.9999
R^2_{adj}	0.9959	R^2_{adj}	0.9999
SD (mg g^{-1})	9.172	SD (g L^{-1})	1.348×10^{-3}
Langmuir-2	Figure 3.16c	Langmuir-2	Figure 3.16d
Q_{max} (mg g^{-1})	512.5	Q_{max} (mg g^{-1})	499.6
K_L (L mg^{-1})	1.055	K_L (L mg^{-1})	1.143
Number of points	13	Number of points	8
Degrees of freedom	11	Degrees of freedom	6
Reduced Chi-Sqr (g mg^{-1})	2.601×10^{-9}	Reduced Chi-Sqr (g mg^{-1})	2.060×10^{-9}
Res. sum of squ. (g $mg^{-1})^2$	2.861×10^{-8}	Res. sum of squ. (g $mg^{-1})^2$	1.236×10^{-8}
R (COC)	0.9943	R (COC)	0.9960
R^2 (COD)	0.9886	R^2 (COD)	0.9920
R^2_{adj}	0.9876	R^2_{adj}	0.9907
SD (g mg^{-1})	5.100×10^{-5}	SD (g mg^{-1})	4.538×10^{-5}
Langmuir-3	Figure 3.16e	Langmuir-3	Figure 3.16f
Q_{max} (mg g^{-1})	514.2	Q_{max} (mg g^{-1})	489.7
K_L (L mg^{-1})	1.032	K_L (L mg^{-1})	1.216
Number of points	13	Number of points	6
Degrees of freedom	11	Degrees of freedom	4
Reduced Chi-Sqr (mg g^{-1})	125.9	Reduced Chi-Sqr (mg g^{-1})	41.72
Res. sum of squ. (mg $g^{-1})^2$	1385	Res. sum of squ. (mg $g^{-1})^2$	166.9
R (COC)	0.9905	R (COC)	0.9958
R^2 (COD)	0.9810	R^2 (COD)	0.9916
R^2_{adj}	0.9793	R^2_{adj}	0.9895
SD (mg g^{-1})	11.22	SD (mg g^{-1})	6.459
Langmuir-4	Figure 3.16g	Langmuir-4	Figure 3.16h
Q_{max} (mg g^{-1})	515.4	Q_{max} (mg g^{-1})	490.6
K_L (L mg^{-1})	1.012	K_L (L mg^{-1})	1.206
Number of points	13	Number of points	6
Degrees of freedom	11	Degrees of freedom	4
Reduced Chi-Sqr (L g^{-1})	131.5	Reduced Chi-Sqr (L g^{-1})	61.17

(continued)

Table 3.4 (continued)

Langmuir-4	Figure 3.16g	Langmuir-4	Figure 3.16h
Residual sum of squ. $(L\ g^{-1})^2$	1446	Residual sum of squ. $(L\ g^{-1})^2$	244.7
R (COC)	0.9905	R (COC)	0.9958
R^2 (COD)	0.9810	R^2 (COD)	0.9916
R^2_{adj}	0.9793	R^2_{adj}	0.9895
SD ($L\ g^{-1}$)	11.47	SD ($L\ g^{-1}$)	7.821

and linearized Langmuir-1, Langmuir-2, Langmuir-3, and Langmuir-4 were compared. Table 3.5 presents the relative differences of the parameters of the isotherm plots depicted on Fig. 3.16. As observed, the Langmuir-1 linearized equation produced the worst values of K_L when compared with nonlinear Langmuir equation. Another important observation is that in all cases when points of isotherms were deleted, although the R^2 values improved in all cases for linearized Langmuir-2, Langmuir-3, and Langmuir-4 equations, but the relative values of Q_{max} and K_L became worse compared with the nonlinear reference values. The analyses of plots in Fig. 3.16 as shown in Tables 3.4 and 3.5 clearly indicate that R^2 values close to unity did not indicate that the model was properly fitted, and, in addition, did not prove that the obtained values of Q_{max} and K_L reflect the reality of the system.

Table 3.5 Relative differences of Q_{max} and K_L isotherm parameters of linearized Langmuir-1, Langmuir-2, Langmuir-3 and Langmuir-4 in relation to nonlinear Langmuir equation

Isotherm Langmuir-1	% difference		
Q_{max}	−1.532		
K_L	27.23		
	Figure 3.16b		
Isotherm Langmuir-2	% difference	Isotherm Langmuir-2	% difference
Q_{max}	0.6398	Q_{max}	3.141
K_L	−5.860	K_L	−14.69
	Figure 3.16c		Figure 3.16d
Isotherm Langmuir-3	% difference	Isotherm Langmuir-3	% difference
Q_{max}	0.3102	Q_{max}	5.060
K_L	−3.552	K_L	−22.01
	Figure 3.16e		Figure 3.16f
Isotherm Langmuir-4	% difference	Isotherm Langmuir-4	% difference
Q_{max}	0.07755	Q_{max}	4.894
K_L	−1.545	K_L	−20.99
	Figure 3.16g		Figure 3.16h

The values are expressed as percentage

Considering that K_L values are very important equilibrium parameters for estimating equilibrium constants (determination of thermodynamic parameters) [10, 23–26], the use of Langmuir-1 linearized isotherms could lead to erroneous estimation of Gibb's free energy change ($\Delta G°$), enthalpy change ($\Delta H°$), and entropy change ($\Delta S°$) of adsorption.

3.4.2 Kinetics of Adsorption

The mostly employed pseudo-first-order and pseudo-second-order kinetic equations are given in Table 3.6 in nonlinear and linearized forms [26, 27]. Let us consider the kinetics of adsorption of DB-53 dye on MWCNT [10]. The experimental kinetic data of adsorption of DB-53 on MWCNT are presented in Table 3.7. The nonlinear pseudo-first-order and linearized pseudo-first-order plots are shown in Fig. 3.17, while nonlinear pseudo-second-order, and linearized pseudo-second-order-1, pseudo-second-order-2, pseudo-second-order-3 and pseudo-second-order-4 plots are presented in Fig. 3.18. It is observed from Table 3.7 that the manipulation of the data alters the units of the variables. The analysis of pseudo-first-order kinetics necessitated deletion of five experimental points to achieve a good value of R^2; however, the DOF decreases from 18 to 13.

The analysis of pseudo-second-order linearized models indicates that the linearized pseudo-second-order-1 equation apparently provides the best values of R^2 for the four linearized models. However, it is necessary to highlight that this analysis did not put into consideration the units of SD and reduced Chi-square, which are not the same for nonlinearized model. Therefore, different incidents are being compared; however, some authors use the value of R^2 to infer that a model is a good fit.

Only linearized pseudo-second-order-3 presents the same units as nonlinearized kinetic equation (Table 3.7), however, the statistical analysis of this equation (SD and reduced Chi squared) is worse than the nonlinearized equation, even after deleting 10 experimental points.

Table 3.6 Kinetics of adsorption

Kinetic model	Linear form	Plot
$q_t = q_e\left[1 - \exp(-k_1 \cdot t)\right]$ Pseudo-first order	$\ln(q_e - q_t) = \ln(q_e) - kt$	$\ln(q_e - q_t)$ versus t
$q_t = \frac{q_e^2 k_2 t}{[k_2(q_e)\cdot t+1]}$ Pseudo second-order	$\frac{t}{q_t} = \frac{1}{k\times q_e^2} + \frac{1}{q_e}t$ Pseudo-second-1	$\frac{t}{q_t}$ versus t
	$\frac{1}{q_t} = \frac{1}{q_e} + \left(\frac{1}{k\cdot q_e^2}\right) \times \frac{1}{t}$ Pseudo-second-2	$\frac{1}{q_t} =$ versus $\frac{1}{t}$
1	$q_t = q_e - \left(\frac{1}{k\cdot q_e}\right)\frac{q_t}{t}$ Pseudo-second-3	q_t versus $\frac{q_t}{t}$
	$\frac{q_t}{t} = k\cdot q_e^2 - k\cdot q_e \cdot q_t$ Pseudo-second-4	$\frac{q_t}{t}$ versus q_t

Table 3.7 Experimental data of the adsorption of DB-53 onto MWCNT at 298 K [10]

Experimental data		Manipulated data				
t (min)	q_t (mg g^{-1})	Ln($q_e - q_t$)	t/q_t (min g mg^{-1})	$1/q_t$ (g mg^{-1})	1/t (min^{-1})	q_t/t (mg g^{-1} min^{-1})
0	0.0000	4.7643	–	–	–	–
5	25.5363	4.5186	0.1958	0.0392	0.2000	5.1073
10	45.1580	4.2779	0.2214	0.0221	0.1000	4.5158
15	60.4185	4.0400	0.2483	0.0166	0.0667	4.0279
20	72.2459	3.8066	0.2768	0.0138	0.0500	3.6123
25	80.5830	3.6017	0.3102	0.0124	0.0400	3.2233
30	87.5292	3.3917	0.3427	0.0114	0.0333	2.9176
45	101.1273	2.7799	0.4450	0.0099	0.0222	2.2473
60	108.7337	2.1413	0.5518	0.0092	0.0167	1.8122
90	113.8832	1.2124	0.7903	0.0088	0.0111	1.2654
120	116.1828	0.0600	1.0329	0.0086	0.0083	0.9682
150	117.0870	−1.8477	1.2811	0.0085	0.0067	0.7806
180	117.0279	−1.5292	1.5381	0.0085	0.0056	0.6502
210	116.4573	−0.2391	1.8032	0.0086	0.0048	0.5546
240	115.8487	0.3335	2.0717	0.0086	0.0042	0.4827
270	116.8314	−0.8838	2.3110	0.0086	0.0037	0.4327
300	117.2445	−9.2103	2.5588	0.0085	0.0033	0.3908
360	116.3430	−0.1036	3.0943	0.0086	0.0028	0.3232

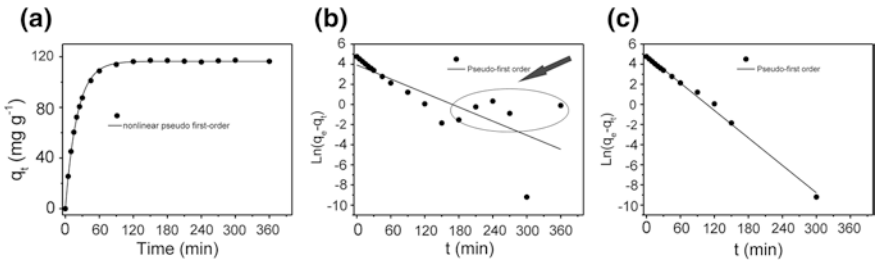

Fig. 3.17 **a** Nonlinearized pseudo-first-order equation; **b** linearized pseudo-first order with all experimental points; **c** linearized pseudo-first-order equation after deleting some points. *Arrows* indicate the region of points that were deleted just to improve the values of R^2

Considering that the kinetics of adsorption is nonlinear equation, the parameter values (q_e and k_1 or k_2) of this model were taken as a reference for computing the relative differences of the linearized models in relation to the nonlinearized equations; these values are depicted in Table 3.9. It is observed that the strategy of deleting some points to improve the values of R^2 causes a serious error in the values of q_e and k_1 or k_2. The activation energy is calculated based on the values of kinetic rate constants of the Arrhenius equation (Eq. 3.35), [23]:

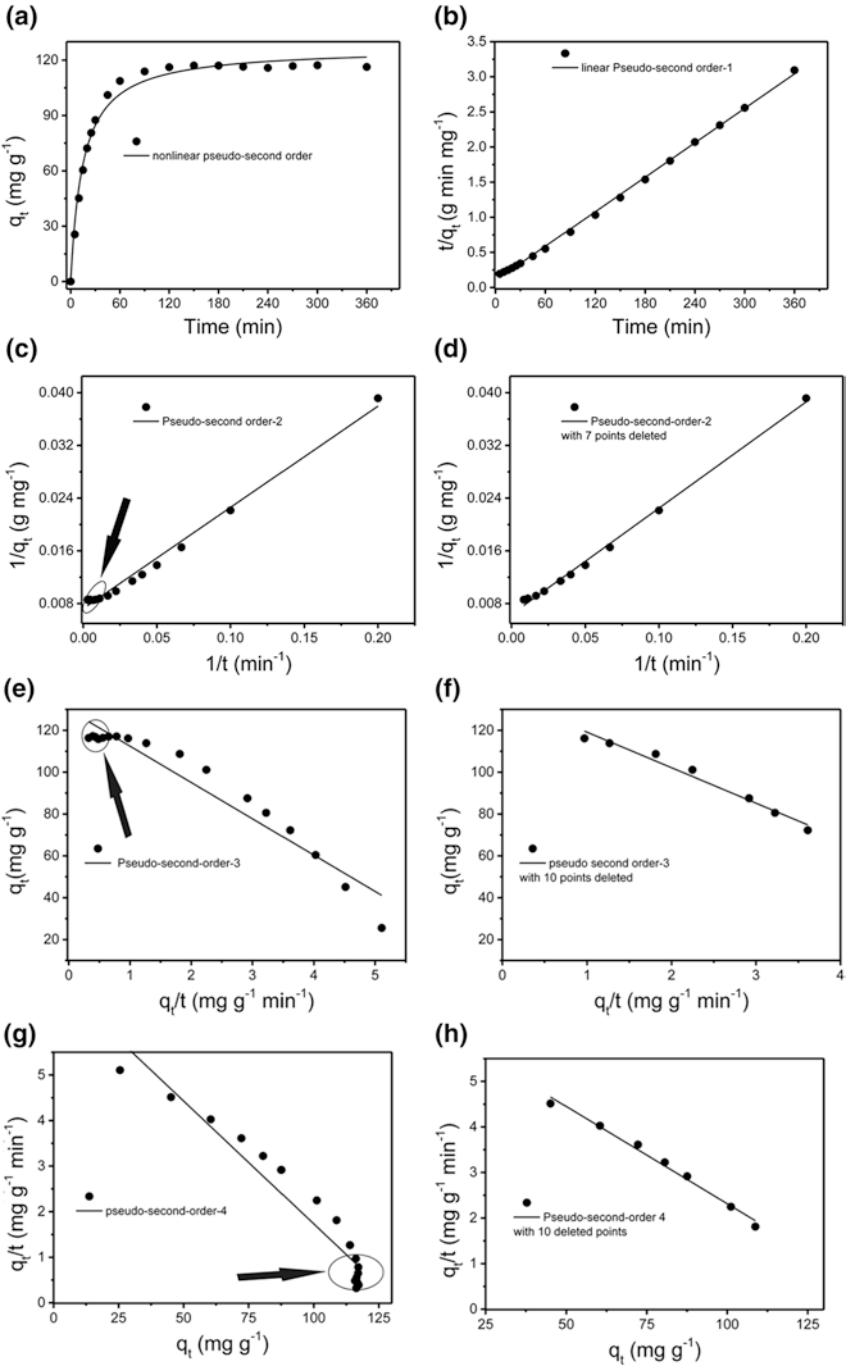
(a)
nonlinear pseudo-second order
q_t (mg g^{-1})
Time (min)
(b)
linear Pseudo-second order-1
t/q_t (g min mg^{-1})
Time (min)
(c)
Pseudo-second order-2
$1/q_t$ (g mg^{-1})
1/t (min^{-1})
(d)
Pseudo-second-order-2
with 7 points deleted
$1/q_t$ (g mg^{-1})
1/t (min^{-1})
(e)
Pseudo-second-order-3
q_t(mg g^{-1})
q_t/t (mg g^{-1} min^{-1})
(f)
pseudo second order-3
with 10 points deleted
q_t(mg g^{-1})
q_t/t (mg g^{-1} min^{-1})
(g)
pseudo-second-order-4
q_t/t (mg g^{-1} min^{-1})
q_t (mg g^{-1})
(h)
Pseudo-second-order 4
with 10 deleted points
q_t/t (mg g^{-1} min^{-1})
q_t (mg g^{-1})

◀ **Fig. 3.18** **a** Nonlinearized pseudo-second-order equation; **b** linearized pseudo-second order-1; **c** linearized pseudo-second order-2; **d** linearized pseudo-second-order-2 after deleting some experimental points; **e** linearized pseudo-second-order-3; **f** linearized pseudo-second-order-3 after deleting some experimental points; **g** linearized pseudo-second-order-4; **h** linearized pseudo-second-order-4 after deleting some experimental points. The *arrows* indicate region of experimental points that were deleted just to improve the values of R^2

$$\ln k_{\text{kinetic}} = \ln A - \frac{E_a}{RT} \tag{3.35}$$

where k_{kinetic} is the kinetic rate constant of adsorption, A is the Arrhenius constant, E_a is the activation energy (kJ mol^{-1}), R is the universal gas constant (8.314 J K^{-1} mol^{-1}), and T is the absolute temperature (K). If the values of k_{kinetic} are biased, the values of calculated activation energy will also be compromised.

We have demonstrated using the given examples (Figs. 3.16, 3.17, and 3.18; Tables 3.4, 3.5 3.8, and 3.9) the existing problems in using linear equations for Langmuir isotherm, pseudo-first-order, and pseudo-second-order kinetics of adsorption. Remarkably, although linearized Langmuir-1 and linearized

Table 3.8 Statistical analysis of data presented in Fig. 3.17

Parameter	Value	Parameter	Value
Nonlinear pseudo-first order	Figure 3.17a	Pseudo-first order-1	Figure 3.17b
k_1 (min^{-1})	0.04766	k_1 (min^{-1})	0.02329
q_e (mg g^{-1})	116.4	q_e (mg g^{-1})	50.83
Number of points	18	Number of points	18
Degrees of freedom	16	Degrees of freedom	16
Reduced Chi-Sqr (mg g^{-1})	0.7032	Reduced Chi-Sqr (min g mg^{-1})	4.621
Residual sum of squ. (mg g^{-1})^2	11.25	Resid. sum of sq. min g mg^{-1})^2	73.94
R value	0.9997	R value	0.7907
R-square (COD)	0.9995	R-square (COD)	0.6252
Adj. R-square	0.9995	Adj. R-square	0.6018
SD (mg g^{-1})	0.8386	SD (min g mg^{-1})	2.150
Linear pseudo-first order-2	Figure 3.17c		
k_1 (min^{-1})	0.04549		
q_e (mg g^{-1})	128.3		
Number of points	13		
Degrees of freedom	11		
Reduced Chi-Sqr (min g mg^{-1})	0.08455		
Residual sum of squ. (min g mg^{-1})^2	0.9301		
R value	0.9974		
R-square (COD)	0.9947		
Adj. R-square	0.9942		
SD (min g mg^{-1})	0.2908		

Table 3.9 Statistical analysis of data presented in Fig. 3.18

Parameter	Value	Parameter	Value
Nonlinear pseudo-second order	Figure 3.18a	Linear pseudo-second order-1	Figure 3.18b
k_2 (min g mg^{-1})	5.306×10^{-4}	k_2 (min g mg^{-1})	6.899×10^{-4}
q_e (mg g^{-1})	126.7	q_e (mg g^{-1})	122.2
Number of points	18	Number of points	17
Degrees of freedom	16	Degrees of freedom	15
Reduced Chi-Sqr (mg g^{-1})	18.02	Red. Chi-Sqr (min g mg^{-1})	0.001193
Res Sum of squ. (mg g^{-1})^2	288.2	Res. sum of squ (min g mg^{-1})^2	0.01789
R value (COC)	0.9935	R value (COC)	0.9994
R-square (COD)	0.9871	R-square (COD)	0.9987
Adj. R-square	0.9862	Adj. R-square	0.9987
SD (mg g^{-1})	4.244	SD (min g mg^{-1})	0.03454
Linear pseudo-second order-2	Figure 3.18c	Linear pseudo-second order-2	Figure 3.18d
k_2 (min g mg^{-1})	3.408×10^{-4}	k_2 (min g mg^{-1})	2.508E-04
q_e (mg g^{-1})	138.2	q_e (mg g^{-1})	157.3
Number of points	17	Number of points	10
Degrees of freedom	15	Degrees of freedom	8
Reduced Chi-Sqr (g mg^{-1})	6.490×10^{-7}	Reduced Chi-Sqr (g mg^{-1})	3.203×10^{-7}
Res. l sum of squ. (g mg^{-1})^2	9.735×10^{-6}	Res. sum of squ. (g mg^{-1})^2	2.562×10^{-6}
R value (COC)	0.9950	R value (COC)	0.9984
R-square (COD)	0.9900	R-square (COD)	0.9968
Adj. R-square	0.9894	Adj. R-square	0.9964
SD (g mg^{-1})	8.056×10^{-4}	SD (g mg^{-1})	5.659×10^{-4}
Linear pseudo-second order-3	Figure 3.18e	Linear pseudo-second order-3	Figure 3.18f
k_2 (min g mg^{-1})	4.437×10^{-4}	k_2 (min g mg^{-1})	4.334×10^{-4}
q_e (mg g^{-1})	129.8	q_e (mg g^{-1})	136.1
Number of points	17	Number of points	7
Degrees of freedom	15	Degrees of freedom	5
Reduced Chi-Sqr (mg g^{-1})	57.27	Reduced Chi-Sqr (mg g^{-1})	8.453
Residual sum of squ. (mg g^{-1})^2	859.1	Residual sum of squ. (mg g^{-1})^2	42.27
R value	0.9679	R value	0.9881
R-square (COD)	0.9368	R-square (COD)	0.9762
Adj. R-square	0.9326	Adj. R-square	0.9715
SD (mg g^{-1})	7.568	SD (mg g^{-1})	2.907
Linear pseudo-second order-4	Figure 3.18g	Linear pseudo-second order-4	Figure 3.18h
k_2 (min g mg^{-1})	4.084×10^{-4}	k_2 (min g mg^{-1})	2.769×10^{-4}
q_e (mg g^{-1})	132.1	q_e (mg g^{-1})	154.2
Number of points	17	Number of points	7
Degrees of freedom	15	Degrees of freedom	5
Reduced Chi-Sqr. (mg g^{-1} min^{-1})	0.1780	Reduced Chi-Sqr. (mg g^{-1} min^{-1})	0.01228

(continued)

Table 3.9 (continued)

Parameter	Value	Parameter	Value
Res. sum of squ. $(\text{mg g}^{-1}\ \text{min}^{-1})^2$	2.669	Resid. sum of squ. $(\text{mg g}^{-1}\ \text{min}^{-1})^2$	0.06140
R value	0.9679	R value	0.9944
R-square (COD)	0.9368	R-square (COD)	0.9888
Adj. R-square	0.9326	Adj. R-square	0.9866
SD ($\text{mg g}^{-1}\ \text{min}^{-1}$)	0.4218	SD. ($\text{mg g}^{-1}\ \text{min}^{-1}$)	0.1108

pseudo-second-order-1 equations provide values of R^2 close to unity, an assumption of a good fit of any model but the values of the parameters (equilibrium and kinetics) differ from those of the nonlinear equations. Similarly, it should be stressed that with the manipulation of data to convert a nonlinear equation to linear formats, the units of the Y and X axes changed remarkably. Therefore, the reduced Chi-square and SD should be taken into consideration while evaluating the fit of a model. Only the linearized model that presents the same Y-axis (q_e and q_t for equilibrium and kinetic equations, respectively) could be directly compared with the nonlinear equations. The linearized equations exhibited different units, although those values could be glancingly better when compared with nonlinear equations, but the numerical values do not correspond to the values of reduced Chi-square and SD of nonlinear equations, and therefore, they are incomparable. We do hope that the perusal of the figures and tables presented in this section will make it clearer to the readers that the nonlinear usage of equilibrium and kinetics of adsorption models give values that are reliable and statistical relevant to the modeling of an isotherm and kinetic of adsorption curve. We do not recommend the usage of linearized equilibrium and kinetics of adsorption models, even in the cases of linearized Langmuir-1 and linearized pseudo-second-order-1 equations.

Table 3.10 shows the relative difference on the kinetic parameters of pseudo-first order and pseudo-second order. In some cases, where experimental data points were deleted to increase the values of R^2 (see Table 3.10), the relative difference of the kinetic parameters became worse compared to parameters before experimental data points were deleted. Therefore, we reiterated that linearization of equilibrium and kinetic of adsorption models could make the parameter values of the models meaningless.

Other point that was not taken into account in this analysis is that for linearization, almost all manuscripts described that linearized pseudo-second-order-1 model is followed. Perusing through Table 3.9, this observation can be erroneously concluded. However, the linearized pseudo-first-order model is not always a good fit. If one compares R^2_{adj} and SD values for nonlinearized kinetic models, in the example given in this chapter (Tables 3.8 and 3.9), one will observe that the kinetic data fit better to nonlinear pseudo-first-order (R^2_{adj} 0.9995; SD 0.8386) than the nonlinear pseudo-second-order (R^2_{adj} 0.9862; SD 4.244). It is important to stress that the SD of nonlinearized pseudo-second order is 5.1 times higher than the nonlinearized pseudo-first order. Therefore, it is evident that the kinetic should follow pseudo-first order in preference. However, using the distorted linearized

Table 3.10 Relative differences of q_e and k_1 or k_2 kinetic parameters of linearized pseudo-first order, linearized pseudo-second order-1, pseudo-second order-2, pseudo-second order-3, and pseudo-second order-4 in relation to nonlinear pseudo-first order and nonlinear pseudo-second order equations

Pseudo-first order 1	% difference		% difference
k_1	4.55	k_1	51.13
q_e	−10.22	q_e	56.33
	Figure 3.17b		Figure 3.17c
Pseudo-second order-1	% difference		
k_2	−30.02		
q_e	3.55		
	Figure 3.18b		
Pseudo-second order-2	% difference		% difference
k_2	35.77	k_2	52.73
q_e	−9.08	q_e	−24.15
	Figure 3.18c		Figure 3.18d
Pseudo-second order-3	% difference		% difference
k_2	16.38	k_2	18.32
q_e	−2.45	q_e	−7.42
	Figure 3.18e		Figure 3.18f
Pseudo-second order-4	% difference		% difference
k_2	23.03	k_2	47.81
q_e	−4.26	q_e	−21.70
	Figure 3.18g		Figure 3.18h

Values are expressed in percentage

equations, the opposite is obtained. This should be one of the reasons majorities of the papers reported in the literature used linearized equations, almost all, suggest that the kinetic should follow pseudo-second order in disadvantage of pseudo-first order. However, if the nonlinearized equations were employed, the opposite could be obtained. This is one of the reasons that the authors of this chapter do not recommend the use of linearized equations for the equilibrium and kinetic of adsorption, and we also reiterate that there are so many errors committed in the published literatures of adsorption research.

3.4.3 Other Common Mistakes in Adsorption Works

It is very common in the adsorption literature that the authors attribute that a mechanism of adsorption is chemisorption based only on the fitting parameters of kinetic data of the linearized pseudo-second-order-1 equation. As visibly seen in the above example, this is the mathematical model that provides the best fitting result (higher R^2, R^2_{adj}, lower SD, among others). In this case the authors committed two errors: first, using linearized equations; only linearized pseudo-second-order-1 equation

fits with good values of R^2, even better than nonlinearized equation; however, the authors did not take into account that the values of k_2 and q_e could be completely compromised (see Table 3.10). Second, using nonlinearized equations; other kinetic models could give better fits than the linearized pseudo-second-order-1 model (see Tables 3.8 and 3.9). Given that the pseudo-second-order kinetic model is the best fitting model (using nonlinear equations) does not mean that adsorption process is a chemical adsorption. The early works of pseudo-second-order model [7, 28] used the sorption of metallic ions with adsorbents that could form complexes with the metallic ions. In this case, the sorption process should be the formation of covalent bond between the adsorbate and the adsorbent. However, this specific case of a pseudo-second-order kinetic model being followed does not imply that the sorption process is a chemisorption. To establish if an adsorption process is chemical or physical, it is necessary to prove the formation of some chemical bonds using some analytical techniques (FTIR, Raman spectroscopy, TGA, and so on) combined with thermodynamical data of changes in enthalpy (ΔH) and changes in entropy (ΔS). It is expected that large organic molecules would be adsorbed by physical interactions and small inorganic ions could be complexed with nitrogen or oxygen atoms of amine, amide, phenols, alcohols, and so on, being an interaction with adsorbent, which is a chemical adsorption process. This chapter will not discuss the errors committed in the literature, where authors attribute adsorption process inadvertently to chemical sorption based just on the kinetic data as explained above.

Another problem that is always commented in almost all adsorption researches is the calculation of the thermodynamic parameters (Enthalpy and Entropy changes) using the equilibrium data. Majority of authors use the following equations for the determination of the thermodynamic parameters:

$$K_D = \frac{(C_o - C_e)}{C_e} \tag{3.36}$$

$$\Delta G^0 = \Delta H^0 - T\Delta S^0 \tag{3.37}$$

$$\Delta G^0 = \mathrm{RT}\,\mathrm{In}(K_D) \tag{3.38}$$

Equation 3.39 is obtained from Eqs. 3.37 and 3.38.

$$\mathrm{In}(K_D) = \frac{\Delta S^0}{R} - \frac{\Delta H^0}{R} \cdot \frac{1}{T} \tag{3.39}$$

where R is the universal gas constant (8.314 J K^{-1} mol^{-1}); T is the absolute temperature (Kelvin); and K_D is the distribution equilibrium constant (dimensionless).

By plotting a graph of $\ln(K_D)$ versus $1/T$, a straight line is obtained. From the intercept and slope of the plot, it is possible to calculate the changes in Entropy $\Delta S°$ and changes in enthalpy ($\Delta H°$), respectively. Until this point, everything seems to be regular. However, some authors usually do not mention how initial concentrations (C_o) and equilibrium concentrations (C_e) they had employed in the calculation of K_D were arrived at. In addition, most authors did not report in their papers that K_D decreases exponentially as C_e and C_o increase, as shown in Fig. 3.19.

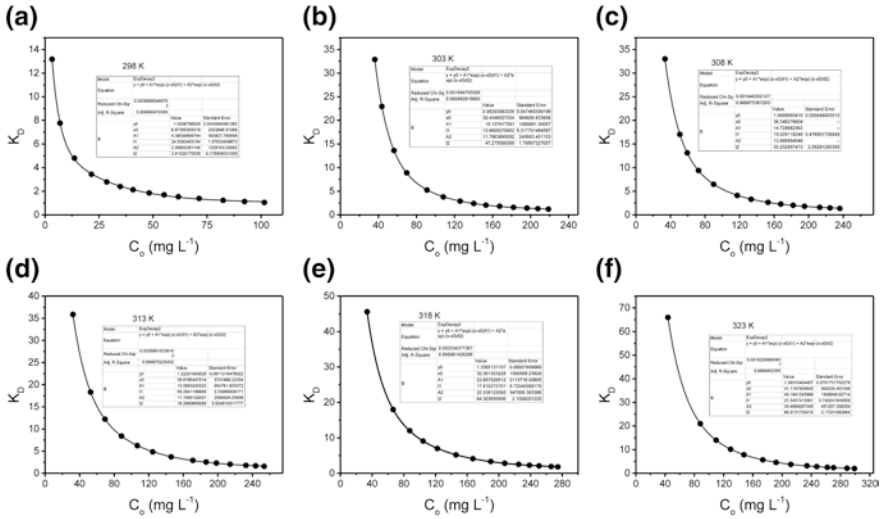

Fig. 3.19 Distribution constant K_D as function of equilibrium concentrations C_e. **a** 298 K; **b** 303 K; **c** 308 K; **d** 313 K; **e** 318 K; **f** 323 K. These data were culled from the adsorption of Reactive Orange-16 (RO-16) dye onto coffee wastes carbon composite [12]

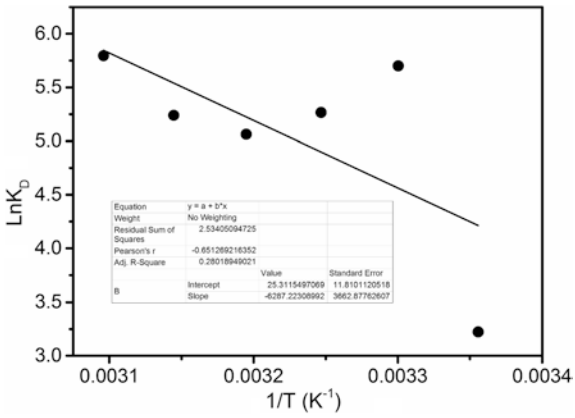

Fig. 3.20 ln (K_D) versus 1/T

As seen in Fig. 3.19, K_D has no fixed value at a given temperature. The most correct K_D value should therefore be calculated from infinite dilution (low values of C_o). By fitting the experimental data to an exponential decay equation, it is possible to evaluate the value of K_D for $C_o = 0$ (the value of K_D at infinite dilution). Using these considerations, it is possible to compute the values of K_D at each temperature value; subsequently, it is possible to calculate the thermodynamic parameters by employing Eq. 3.39. Figure 3.20 shows this graph.

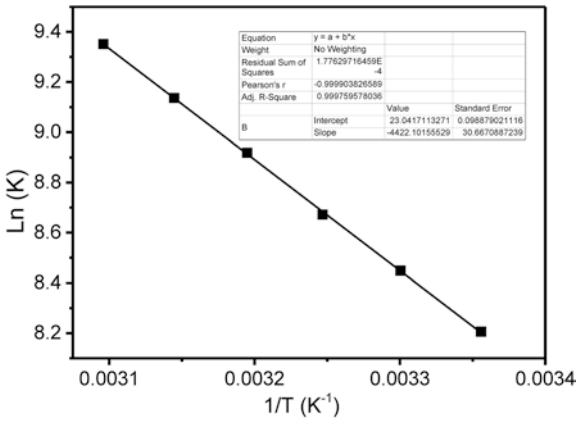

Fig. 3.21 ln K versus $1/T$

By observing Fig. 3.20, it is remarkable that $\ln(K_D)$ versus $1/T$ is not a linear relation (R^2_{adj} 0.2802). Therefore, if the authors calculate K_D at infinite dilution, it is quite impossible to determine correctly the values of $\Delta H°$ and $\Delta S°$ of adsorption process.

On the contrary, instead of calculating the equilibrium constant (K_D), it is possible to calculate the value of adsorption equilibrium constant from the value of the nonlinear isotherm equilibrium model that gives the best fit to the experimental data. Therefore, K is the equilibrium adsorption constants of the isotherm fits (for this specific case ($K = K_g$), K_g—Liu equilibrium constant, which must be converted to SI units using the molecular mass of the dye). Making a plot of $\ln(K)$ versus $1/T$, a linear graph should be obtained. It is possible to evaluate $\Delta S°$ and $\Delta H°$ from the respective intercept and slope of the plot [24].

From Fig. 3.21, it is observed that the equilibrium constants calculated from the Liu isotherm (from 298 to 323 K) [12] showed a linear relationship with the reciprocal of temperature. From this figure, $\Delta S°$ (177.3 J K^{-1} mol^{-1}) and $\Delta H°$ (30.4 kJ mol^{-1}) were calculated [24]. These values of adsorption enthalpy are in agreement with the electrostatic attraction of negatively charged dye reactive red 120 with the positively charged adsorbent at pH 2.0 as reported in the literature [24].

3.5 Concluding Remarks

In this chapter, the commonly employed and unpopular adsorption equilibrium isotherm models such as Langmuir, Freundlich, Sips, Liu, Redlich–Peterson, Hill, Khan, Radke–Prausnitz and Toth were discussed with suitable illustrations. Adsorption kinetic models such as pseudo-first-order, pseudo-second-order, general-order and empiric models (Avrami fractionary and Elovich chemisorption) were adequately described. The usage of different isotherm models at different temperature values was suggested in this chapter. The importance and consideration of statistical parameters such as R^2_{adj} and SD were emphasized. The statistical

analysis is a guidance for adsorption researchers to select the best adsorption isotherm and kinetic model for their work, which is coupled with obtainability of useful constants or parameters that are meaningful. The model with the best value of R^2_{adj} and the lowest value of SD should be considered as the best isotherm and kinetic model to describe the adsorption process. Based on the detailed analysis of linearized and nonlinearized models in this chapter, we do not recommend the use of linearized equations for the analysis of adsorption equilibrium and kinetic data. Analytical techniques together with thermodynamical data of enthalpy and entropy changes are needed to affirm if an adsorption process is a chemical or a physical process. It is advisable to evaluate the value of adsorption equilibrium constant (K) from the value of the best fit nonlinear isotherm equilibrium model instead of using calculated equilibrium constant (K_D) from initial and equilibrium concentrations of an adsorbate. Overall, this chapter proffered solutions to the common errors arising from usage of linearized equilibrium and kinetic adsorption models.

Acknowledgments The authors acknowledge funding from Brazilian agencies CNPq, CAPES, and TWAS.

References

1. Langmuir I (1918) The adsorption of gases on plane surfaces of glass, mica and platinum. J Am Chem Soc 40:1361–1403
2. Freundlich H (1906) Adsorption in solution. Phys Chem Soc 40:1361–1368
3. Sips R (1948) On the structure of a catalyst surface. J Chem Phys 16:490–495
4. Liu Y, Xu H, Yang SF, Tay JH (2003) A general model for biosorption of Cd^{2+}, Cu^{2+} and Zn^{2+} by aerobic granules. J Biotechnol 102:233–239
5. Redlich O, Peterson DL (1959) A useful adsorption isotherm. J Chem Phys 63:1024–1027
6. Largegren S (1898) About the theory of so-called adsorption of soluble substances. Kungliga Suensk Vetenskapsakademiens Handlingar 24:1–39
7. Blanachard G, Maunaye M, Martin G (1984) Removal of heavy metals from waters by means of natural zeolites. Water Res 18:1501–1507
8. Alencar WS, Lima EC, Royer B et al (2012) Application of aqai stalks as biosorbents for the removal of the dye Procion Blue MX-R from aqueous solution. Sep Sci Technol 47:513–526
9. Vaghetti JCP, Lima EC, Royer B et al (2009) Pecan nutshell as biosorbent to remove Cu(II), Mn(II) and Pb(II) from aqueous solutions. J Hazard Mater 162:270–280
10. Prola LDT, Machado FM, Bergmann CP et al (2013) Adsorption of Direct Blue 53 dye from aqueous solutions by multi-walled carbon nanotubes and activated carbon. J Environ Manage 130:166–175
11. Foo KY, Hameed BH (2010) Review—insights into the modelling of adsorption isotherm systems. Chem Eng J 156:2–10
12. Liu Y, Liu YJ (2008) Review—biosorption isotherms, kinetics and thermodynamics. Sep Purif Technol 61:229–242
13. Ho YS (2006) Review of second-order models for adsorption systems. J Hazard Mater 136:681–689
14. Liu Y, Shen L (2008) A general rate law equation for biosorption. Biochem Eng J 38:390–394
15. Vaghetti JCP, Lima EC, Royer B et al (2008) Application of Brazilian-pine fruit coat as a biosorbent to removal of Cr(VI) from aqueous solution. Kinetics and equilibrium study. Biochem Eng J 42:67–76

16. Lopes ECN, dos Anjos FSC, Vieira EFS, Cestari AR (2003) An alternative Avrami equation to evaluate kinetic parameters of the interaction of Hg(II) with thin chitosan membranes. J Colloid Interface Sci 263:542–547
17. Machado FM, Bergmann CP, Lima EC et al (2012) Adsorption of Reactive Blue 4 dye from water solutions by carbon nanotubes: experiment and theory. Phys Chem Chem Phys 14:11139–11153
18. Adebayo MA, Prola LDT, Lima EC et al (2014) Adsorption of Procion Blue MX-R dye from aqueous solutions by lignin chemically modified with aluminium and manganese. J Hazard Mater 268:43–50
19. Krowiak AW (2012) Analysis of temperature-dependent biosorption of Cu^{2+} ions on sunflower hulls: kinetics, equilibrium and mechanism of the process. Chem Eng J 192:13–20
20. Weber-Jr WJ, Morris JC (1963) Kinetics of adsorption on carbon from solution. J Sanit Eng Div Am Soc Civil Eng 89:31–59
21. El-Khaiary MI, Malash GF (2011) Common data analysis errors in batch adsorption studies. Hydrometallurgy 105:314–320
22. Kumar KV (2007) Optimum sorption isotherm by linear and non-linear methods for malachite green onto lemon peel. Dyes Pigm 74:595–597
23. Machado FM, Bergmann CP, Fernandes THM (2011) Adsorption of Reactive Red M-2BE dye from water solutions by multi-walled carbon nanotubes and activated carbon. J Hazard Mater 192:1122–1131
24. Prola LDT, Acayanka E, Lima EC et al (2013) Comparison of Jatropha curcas shells in natural form and treated by non-thermal plasma as biosorbents for removal of Reactive Red 120 textile dye from aqueous solution. Ind Crop Prod 46:328–340
25. Cardoso NF, Lima EC, Royer B (2012) Comparison of Spirulina platensis microalgae and commercial activated carbon as adsorbents for the removal of Reactive Red 120 dye from aqueous effluents. J Hazard Mater 241–242:146–153
26. Calvete C, Lima EC, Cardoso NF, Vaghetti JCP, Dias SLP, Pavan FA (2010) Application of carbon adsorbents prepared from Brazilian-pine fruit shell for the removal of reactive orange 16 from aqueous solution: kinetic, equilibrium, and thermodynamic studies. J Environ Manage 91:1695–1706
27. El-Khaiary MI, Malash GF, Ho YS (2010) On the use of linearized pseudo-second-order kinetic equations for modelling adsorption systems. Desalination 257:93–101
28. Ho YS, McKay G (2010) The kinetics of sorption of divalent metal ions onto sphagnum moss peat. Water Res 34:735–742

Chapter 4
Experimental Adsorption

Éder Cláudio Lima, Matthew Ayorinde Adebayo and Fernando Machado Machado

Abstract One of the major challenges of the technological driven society is the lingering environmental pollution as a result of toxic species. Adsorption is one of the versatile techniques employed for removal of toxic species from aqueous solutions. Several factors have been identified to influence adsorptive systems. Thus, it is pertinent to know the phenomena involved in the adsorption processes in order to improve the conditions for the interaction between adsorbent and adsorbate. In this context, we present in this chapter several factors and experimental conditions that could have effect on the batch adsorption method. The role of the morphology and textural properties of the adsorbents such as pore size, total pore volume and superficial area are developed in the text. Moreover, the effects of the initial adsorbate concentration and dosage of adsorbent in the adsorption process are explained. We also evaluate the importance of the major experimental conditions in the adsorption process, these being the pH of adsorbate solution, agitation speed, the temperature at which the adsorption process is carried out and the contact time between the adsorbent and adsorbate.

Keywords Textural properties · Adsorbate concentrations · pH of solution · Contact time · Temperature · Adsorbent dosage

É.C. Lima (✉)
Instituto de Química, Universidade Federal do Rio Grande do Sul, Porto Alegre, RS 91501970, Brazil
e-mail: profederlima@gmail.com

M.A. Adebayo
Department of Chemistry, Federal University of Agriculture, Abeokuta 110008, Ogun State, Nigeria
e-mail: adebayomao@gmail.com

F.M. Machado
Centro de Desenvolvimento Tecnológico, Universidade Federal de Pelotas, Pelotas, RS 96010610, Brazil
e-mail: machado@hotmail.com.br

C.P. Bergmann and F.M. Machado (eds.), *Carbon Nanomaterials as Adsorbents for Environmental and Biological Applications*, Carbon Nanostructures,
DOI 10.1007/978-3-319-18875-1_4

Abbreviations

IUPAC	International Union of Pure and Applied Chemistry
MWCNT	Multi-walled carbon nanotubes
pH_{ZPC}	Point of zero charge
PW	Pore width
SWCNT	Single-walled carbon nanotubes

4.1 Introduction

Water, a polar and basic substance, is needed by a living system for transportation of nutrients as well as waste products of metabolism. The water system is being polluted every day. There is a connection between pollution and diseases. Large amounts of pollutants are released to the hydric system annually due to industrial, agro-industrial and domestic activities. The discharge of untreated effluents from industries has direct or indirect adverse effects on aquatic organisms and human beings. Therefore, an improvement of methods for increasing the efficiency of effluent treatment is very important.

As a result of the strict regulations by the governmental organizations and agencies over the releases of pollutants to the environment, several methods for the treatment of effluents have been established. Out of the several methods for effluent treatment, the adsorption technique is the most promising procedure for effluent treatment because the method is easy, cheap and efficient for treatment of effluent. Utilization of nanomaterials as adsorbents for wastewater or effluent treatment has lessen human exposure to environmental risks. The pollutant is retained in a solid phase. This technique allows large amount of contaminated effluents to be treated with a small amount of an adsorbent, which reduces the quantity of the pollutant by a factor of between 100 and 1000 after treatment. One of advantages of adsorption method is that the adsorbent could be regenerated and stored for a reuse. It is germane to stress that the bioavailability of the pollutant retained in a solid phase is lower than the one present in aqueous medium. The treated water could be released into environment or reused in industrial processes that require water of low purity [1].

In this way it is very important to know the phenomena involved in the adsorption processes so that the interactive conditions between the adsorbent and adsorbate could be improved upon. There are several influential factors and experimental conditions of adsorptive systems. The main factors that could have influence on the adsorption processes are: morphology and textural properties of adsorbents, initial concentrations of adsorbate, pH of the adsorbate, contact time, temperature, adsorbent dosage and agitation speed.

4.2 Morphology and Textural Properties of Adsorbents

For a success of wastewater treatment, the correct choice of the adsorbent is a major determining factor. The sorption capacity of the chosen adsorbent, its mechanical and chemical resistance in the applied medium should be taken into consideration. Similarly, the ability to regenerate the loaded adsorbent should be considered.

The textural properties of the adsorbents such as pore size, total pore volume and superficial area are important factors that influence the adsorption process because adsorption is a surface phenomenon [2]. Adsorption of pollutants utilizing nanomaterials requires interaction between functional groups of an adsorbate and the active sites of a nanomaterial (adsorbent), which is influenced by the textural and structural properties of the adsorbent.

The adsorption efficiency depends on the pore size, since the adsorbate could be retained on the surface of the adsorbent and could diffused in the internal pores of the adsorbent (intra-particle diffusion). In the latter mechanism, the pore size is directly related to the rate of diffusion of adsorbate in the internal pores of the adsorbent and to the sorption capacity of the adsorbent [2, 3].

According to the International Union of Pure and Applied Chemistry (IUPAC), the total porosity of a material can be classified based on the pore width [2–4], as shown in Table 4.1.

The pore size is expressed in terms of the diameter of the aperture by presuming cylindrical or slit width as shown in Fig. 4.1, for a case of a single-walled carbon nanotube (SWCNT) (Fig. 4.1a) and two overlapping sheets of graphene (Fig. 4.1b).

The sorption capacity of an adsorbent is directly related to the pore size ratio of the adsorbent, which is a function of the dimension of the adsorbate specie. The adsorption of gases occurs meanly at the micropores of an adsorbent [5, 6], on the other hand, higher molecules such as synthetic dyes are mainly retained in the mesopores of an adsorbent [7, 8]. It is well known that the surface area is higher for microporous materials [9], therefore, higher surface area and higher pore volume of the adsorbent will yield adsorbents with high sorption capacity for small species such as gases and inorganic ions [7–10]. For larger adsorbates, the resistance to the diffusion is higher and part of the internal surface of the adsorbent is unavailable for adsorption. The accessibility to the active sites of the adsorbent is easier for adsorbents with wider pores and large particle sizes that would lead to

Table 4.1 Pore size denomination according to IUPAC

Classification	Pore width
Micropore	PW < 2 nm
Mesopore	2 nm < PW < 50 nm
Macropore	PW > 50 nm

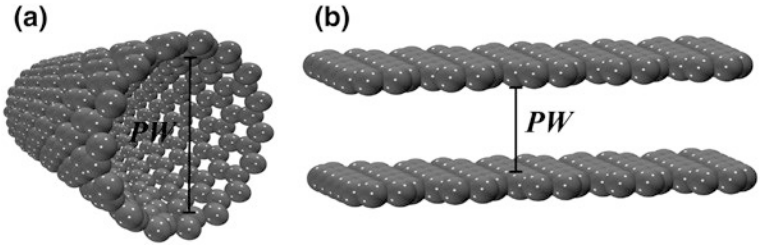

Fig. 4.1 Schematic diagram of representative pores in carbon nanomaterials: **a** cylindrical pore and **b** slit pore

higher sorption capacity of the adsorbent for larger adsorbates [6]. The volume of all breaks, cracks, holes and channels within the body of the adsorbent particles corresponds to the total pore volume [10]. This characteristic is also very important in the sorption capacity of an adsorbent. Adsorbent with higher total pore volume will have higher sorption capacity [10].

Besides the textural properties described above, the structural characteristic is also important. The arrangement of atoms and electronic properties of the adsorbent also present an important role in the adsorption process, mainly with the carbon nanoadsorbents, such as graphene-family as well as nanotubes. The highly hydrophobic property of these adsorbents is as a result of high π electron density of sp^2 carbons, donor–acceptor interactions between the surface carbonyl groups (electron donors) and the aromatic rings [11]. Furthermore, the nanosized structures of nanocarbon adsorbents also endow them some advantages such as rapid equilibrium rates, high adsorption capacity, and effectiveness over a broad pH range [12]. These characteristics were elucidated in Chap. 2.

4.3 The Initial Adsorbate Concentrations

The initial concentration (C_o) is an important parameter that gives information about the capacity of the adsorbent using a fixed amount of the adsorbent. Usually, increasing the initial adsorbate concentration would lead to an increase in the amount adsorbed, until the adsorbent gets saturated. Figure 4.2 shows an example of an adsorbent present in a fix amount while the initial concentration of the adsorbate was varied. The sorption capacity increases and then level-off when the surface of adsorbent gets saturated.

It is reported in the literature that the sorption capacities of some adsorbents, such as composite of multi-walled carbon nanotubes (MWCNT) increase with an increase of the adsorbate concentration [10, 13]. This is attributed to the greater driving force through a higher concentration gradient at high concentration levels [10, 14]. Besides that, for adsorbate solutions with lower concentration, the initial sorption rate is faster and an increase in the initial concentration leads to an

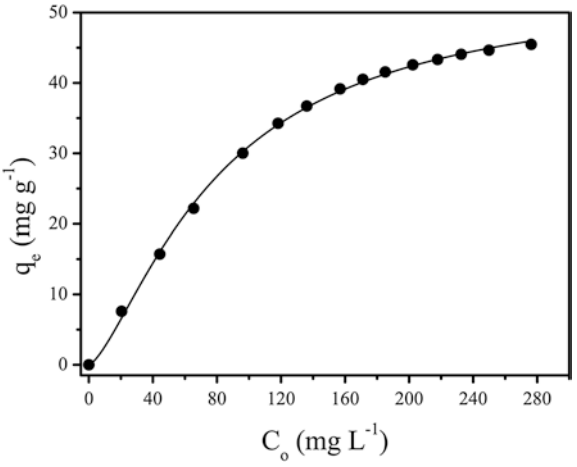

Fig. 4.2 Effect of initial adsorbate concentration on the sorption capacity of an adsorbent

increase in the time necessary to attain the equilibrium [14]. This is one of the reasons why authors use agitation time higher than the equilibrium time when investigating isotherms with higher concentrations of the adsorbate [1, 7, 8, 10, 15].

4.4 pH of the Solution

One of the most influential factors in adsorption studies is the effect of pH of the adsorbate solution. Different adsorbate have different suitable pH ranges, depending on the adsorbent used. The adsorption of contaminants molecules on carbon nanostructures is affected by surface charge of adsorbent and speciation of pollutant in solution, which in turn is influenced by solution pH [7, 8]. The pH of the solution influences the adsorption capacity and overall adsorption process [7, 8].

It is possible to know if the surface of an adsorbent is positively or negatively charged depending on pH. The point of zero charge (pH_{PZC}) is the pH value required for surface of adsorbent to have a net neutral charge. Figure 4.3 shows the influence of the pH_{PZC} of a natural adsorbent on the percentage of a reactive dye removal as a function of the initial pH of the dye solution [8]. The pH = 5.45 for the natural adsorbent. For illustration, using the Reactive Red 120 dye with six sulphonate groups as the adsorbate. These sulphonate groups are negative charged even in highly acidic solutions because their pKa values are lower than zero [8]. For pH values lower than pH_{PZC} the adsorbent presents a positive surface charge (see Fig. 4.3a) [8]. The dissolved Reactive Red 120 dye is negatively charged in aqueous solutions. The adsorption of the Reactive Red 120 dye takes place when the adsorbent present a positive surface charge (pH < 5.45). However, the lower the pH value from the pH_{PZC}, the more positive the surface of the adsorbent [8]. This phenomenon explains the high sorption capacity of Reactive Red 120 dye at pH = 2 using a natural adsorbent (see Fig. 4.3b).

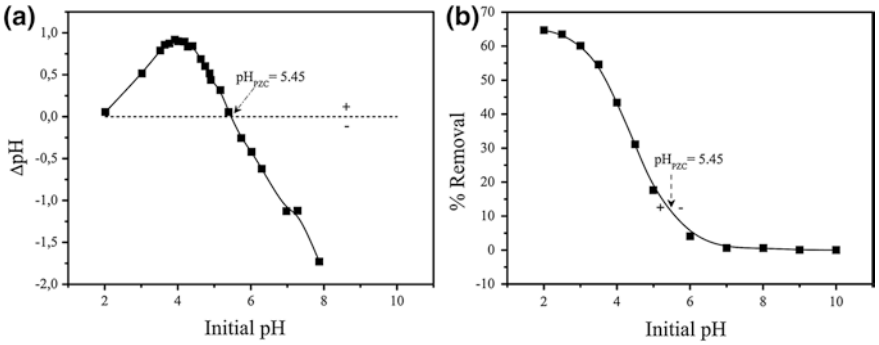

Fig. 4.3 **a** The point of zero charge of a natural adsorbent. **b** The influence of pH_{PZC} of a natural adsorbent on the percentage of removal of Reactive Red 120 dye from aqueous solutions at different pH values of the adsorbate solution. The symbol + and − stands for positively and negatively charged surface, respectively

This adsorbent can adsorb anions at pH < pH_{PZC} and adsorb cations at pH > pH_{PZC}. The adsorption of cations from adsorbate solution with pH values lower than the pH_{ZPC} is not favored because of the occurrence of the electrostatic repulsion between the positively charged adsorbent surface and the cations, as well as the competition between H^+ and cations. On the other hand, the adsorbent surface will be negative charged when pH of the adsorbate solution is greater than the pH_{ZPC} (alkaline pH), therefore, the functional groups on the adsorbent surface are deprotonated to form the negative charged surface, thereby favors adsorption of cations on the surface of the carbon adsorbent [15].

It is noteworthy that the pH_{PZC} of carbonaceous materials depends on acidic functional groups on their surface [16, 17]. The higher the concentration of acidic functional groups on the surface, the lower the pH_{PZC} value of carbonaceous materials [18].

4.5 Contact Time

During the kinetic adsorption studies it is possible to measure the minimum time to attain the equilibrium. After this time, it is assumed that the system attained the equilibrium. However, the adsorption user should take into account that the initial adsorbate concentration influences the adsorption rate. Therefore, after performing the kinetic experiments, and obtaining the minimum time to attain the equilibrium, it is wise to increase the contact time for the proper interaction between the adsorbent and adsorbate to guarantee proper equilibrium at higher concentration levels [1, 7, 8, 10, 15]. The effect of contact time on the adsorption of Direct Blue 53 (DB-53) dye [10] onto MWCNT is presented in Fig. 4.4.

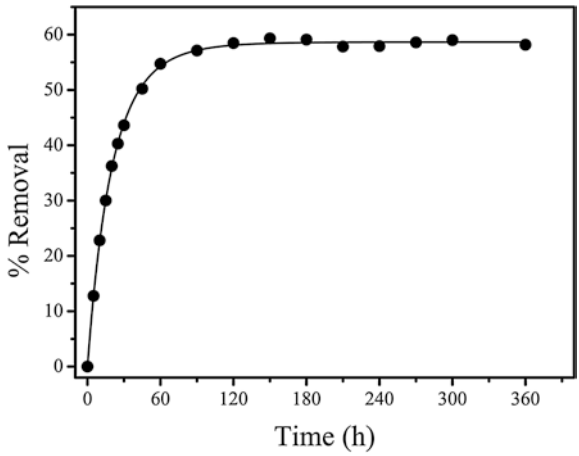

Fig. 4.4 Effect of contact time for the interaction between DB-53 dye and MWCNT. Initial concentration 300.0 mg L^{-1}, temperature 25 °C

4.6 Temperature

The temperature at which the adsorption process is carried out will influence both the rate of sorption and the degree in which sorption occurs. An increase in temperature may lead to an increase in the kinetic energy and mobility of the molecules of the adsorbate and also increase the rate of intra-particle diffusion of the adsorbate [19]. As the molecules increase beyond the mobility of the adsorbate, the viscosity of the solution decreases with the increase in temperature, which in turn aids diffusing of molecules into the pores surface [18].

It is reported in the literature that the adsorption capacity of metal ions, for example, of Zn(II) and Pb(II) increases considerably with an increase in temperature [20, 21]. Furthermore, the time required for the adsorption of about 50 % of maximum sorption capacity to take place is lower at higher temperatures in the case of Zn(II) [21]. Similar pattern is also observed for the adsorption of textile dyes [22, 23]. Therefore, changes in the temperature could alter the sorption capacity. This prediction, however, is not easy to obtain. An increase in temperature could increase or keep practically constant or decrease the sorption capacity of a given adsorbate on adsorbent.

In the adsorption process the effect of temperature on the system is reflected in the rate constant of adsorption. If adsorption studies are performed at different temperature values, one can obtain the value of the respective rate constants that can be used to evaluate the activation energy (E_a) of process using Eq. (4.1). Equation (4.1) is known as Arrhenius equation [24].

$$\ln k = \ln A - \frac{E_a}{RT} \tag{4.1}$$

where k is the rate constant of the adsorption process; A is the Arrhenius constant; and E_a is the Arrhenius activation energy (kJ mol^{-1}) of the adsorption

process, T is the absolute temperature (Kelvin) and R is the universal gas constant (8.314 J mol^{-1} K^{-1}). A plot of ln k versus 1/T should show a linear relationship with a slope $-E_a/R$, allowing the calculation of E_a of the process. This parameter is important because it describes the nature of the interactions between the adsorbate molecule and the adsorbent [24, 25].

Other activation parameters such as the variation of the activation enthalpy (ΔH^*) and the change in entropy of activation (ΔS^*) can be obtained from Eyring equation, Eq. (4.2).

$$\ln\left(\frac{k}{T}\right) = \ln\left(\frac{k_B}{\hbar}\right) + \frac{\Delta S^*}{R} - \frac{\Delta H^*}{R} \cdot \frac{1}{T} \tag{4.2}$$

where k_B (1.381 × 10^{-23} J mol^{-1}) and ħ (6.626 × 10^{-34} J s) are the Boltzmann and Planck constants, respectively. The linear relationship of ln (k/T) versus 1/T gives $\Delta H^*/R$ as the slope from which the activation enthalpy can be calculated. From the intercept the term ln (k_B/ħ) + $\Delta S^*/R$ from which the entropy of activation can be obtained. Using the activation parameters ΔH^* and ΔS^*, the free energy of activation ΔG^* can be calculated from the following relationship (Eq. 4.3) [24]:

$$\Delta G^* = \Delta H^* - T\Delta S^* \tag{4.3}$$

Another important change that occur when the temperature is increased is the equilibrium constants obtained from different isotherm models. An increase in temperature could decrease or increase the equilibrium constant of a pair of adsorbate/adsorbent. This observation affects the thermodynamics parameters of adsorption such as Gibb's free energy, enthalpy change and entropy change. The Gibb's free energy change ($\Delta G°$, kJ mol^{-1}), enthalpy change ($\Delta H°$, kJ mol^{-1}) and entropy change ($\Delta S°$, J mol^{-1} K^{-1}) can be evaluated with the aid of Eqs. 4.4–4.6, respectively.

$$\Delta G^0 = \Delta H^0 - T\Delta S^0 \tag{4.4}$$

$$\Delta G^0 = -RT \ln(K) \tag{4.5}$$

Equation 4.6 is obtained from Eqs. 4.4 and 4.5;

$$\ln(K) = \frac{\Delta S^0}{R} - \frac{\Delta H^0}{R} \cdot \frac{1}{T} \tag{4.6}$$

where R is the universal gas constant (8.314 J K^{-1} mol^{-1}); T is the absolute temperature (Kelvin); K represents the adsorption constants of the isotherm fits (K—the equilibrium constant, which must be converted to SI units, by using the molecular mass of the adsorbate) obtained from the isotherm plots. It is known that different adsorption equilibrium constants (K) can be obtained from different isotherm models [26–30]. Therefore, if an increase in temperature induce systematic increase in the equilibrium constant of an isotherm, the process of adsorption is endothermic. On the other hand, if an increase in temperature of the adsorption

experiments bring about a decrease in the equilibrium constant, the process is exothermic. Authors sometimes confound this concept with the increase of sorption capacity. An increase in sorption capacity (q_e) as a result of an increase in temperature does not means that the adsorption process is endothermic. It could be exothermic. The nature of the process depends if the equilibrium constant obtained from different isotherms (Langmuir, Sips, Liu, etc.) increases or decreases with an increment in temperature. In Tables 4.2, 4.3 and 4.4, it could be noticed that an increase in the temperature of adsorption induces an increment in the maximum sorption capacity (Q_{max}) but decreases the Liu equilibrium constant (exothermic process); an increase in temperature causes an increase in the Q_{max} and an increase in the Sips equilibrium constant (endothermic process); similarly in the third case, an increase in temperature led to a decrease in Q_{max} and a decrease in the values

Table 4.2 Isotherm parameters for Reactive Violet-5 dye adsorption using Cocoa shell activated carbon [31]

	298 K	303 K	308 K	313 K	318 K	323 K
Liu isotherm						
Q_{max} (mg g^{-1})	603.3	577.7	554.1	530.4	510.8	491.0
K_g (L mg^{-1})	0.3237	0.2756	0.2384	0.2049	0.1734	0.1471
n_L	0.3873	0.4704	0.5738	0.7017	0.8259	0.9099
R^2	0.9998	0.9998	0.9997	0.9996	0.9997	0.9997

Where K_g is the Liu equilibrium constant, n_L is dimensionless exponent of the Liu equation and R^2 is the determination factor

Table 4.3 Isotherm parameters for Reactive Red 120 dye adsorption, using Pìnõn activated carbon [32]

	298 K	303 K	308 K	313 K	318 K	323 K
Sips isotherm						
Q_{max} (mg g^{-1})	292	306	312	317	323	328
K_S [(g L^{-1})$^{-1/n_S}$]	0.173	0.195	0.221	0.251	0.283	0.318
n_S	1.25	1.33	1.46	1.59	1.93	2.15
R^2	1.000	1.000	1.000	1.000	1.000	1.000

Where K_S is the Sips equilibrium constant and n_S is dimensionless exponent of the Sips equation

Table 4.4 Isotherm parameters for Reactive red 120 dye adsorption, using *Spirulina platensis* microalgae adsorbent [30]

	298 K	303 K	308 K	313 K	318 K	323 K
Liu isotherm						
Q_{max} (mg g^{-1})	482.2	447.6	413.9	386.1	359.4	333.2
K_g (L mg^{-1})	0.1698	0.1539	0.1412	0.1257	0.1142	0.1048
n_L	0.5235	0.5424	0.5658	0.5781	0.5890	0.5313
R^2_{adj}	0.9996	0.9997	0.9998	0.9996	0.9998	0.9996

Where R^2_{adj} is the adjusted determination factor

of K (exothermic process). Based on these values, it is not possible to predict if an increase in temperature would lead to endothermic or exothermic adsorption process, unless the isotherm equilibrium constants are evaluated.

4.7 Adsorbent Dosages

The variation of adsorbent dosage for the removal of adsorbates from aqueous solution is usually carried out using adsorbent dosages ranging from 1.0 to 30.0 g L^{-1} of adsorbents [32, 33] at a fixed adsorbate concentration. Initially, an increase in adsorbent dosage tends to cause an increase in the percentage of removal, until a plateau is reached and the curve is leveled off (see Fig. 4.5). For adsorbent dosages higher than the threshold value of adsorbent dosage, the percentage of adsorbate removal remained almost constant. Increasing in the percentage of the adsorbate removal as the adsorbent dosages increase up to threshold value of adsorbent dosage could be attributed to increases in the adsorbent surface areas, augmenting the number of adsorption sites available for adsorption, as already reported in several papers [32, 33]. On the other hand, an increase in the adsorbent doses leads to a remarkable decrease in the amount of dye uptake per gram of adsorbent (q), (see Fig. 4.6). The effect can be mathematically explained using Eq. 4.7 [32, 33].

$$q = \frac{\%\text{Removal} \cdot C_o}{100 \cdot X} \tag{4.7}$$

As observed from Eq. 4.7 the amount of adsorbate uptake (q) is inversely proportional to the adsorbent dosages (X). An increase in the adsorbent dosage leads to a decrease in q values, since the volume (V) and initial adsorbate concentrations

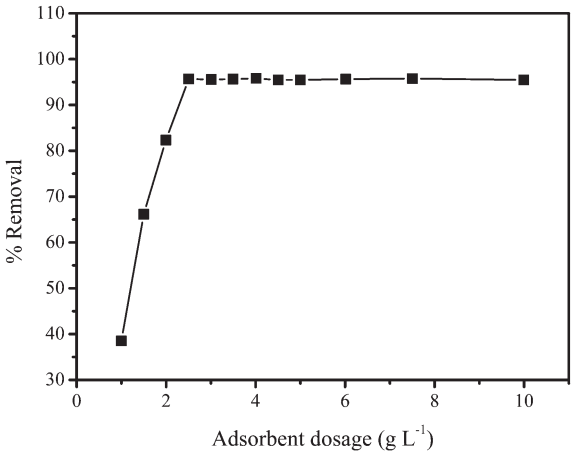

Fig. 4.5 Effect of adsorbent dosage on the percentage of removal of an adsorbate using an adsorbent

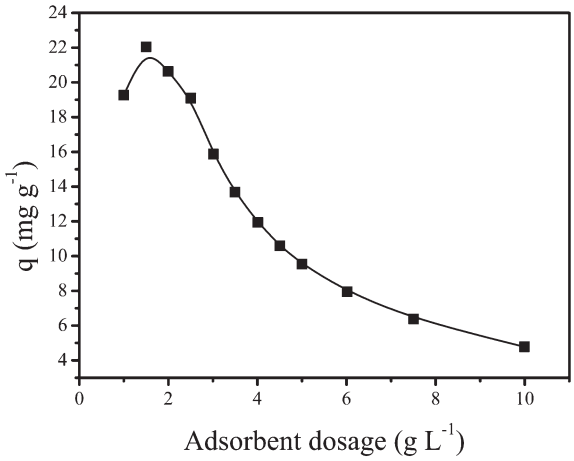

Fig. 4.6 Effect of adsorbent dosage on the sorption capacity of an adsorbate using an adsorbent

(C_o) are always fixed. These values clearly indicate that the adsorbent dosage must be fixed at the threshold value, which is the adsorbent dosage that corresponds to the minimum amount of adsorbent that leads to constant adsorbate removal [33]. Moreover, the mathematical explanation about the decrease of q value with an increase in adsorbent dosage can be explained using two factors. Firstly, an increase in adsorbent mass at fixed adsorbate concentration and volume will lead to unsaturation of adsorption sites through the adsorption process, and secondly, the reduction in adsorbent capacity may be due to particle aggregation, resulting from high adsorbent mass. Such aggregation would lead to a decrease in the total surface area of the adsorbent and an increase in diffusional path length [33].

4.8 Agitation Speed

Another influential factor of adsorptive system is agitation speed. Agitation speed is not always investigated, however, it influences adsorption process up to a remarkable level. An adsorbent must interact properly with a given adsorbate before it can be adsorbed from solutions. Therefore, an adsorptive system must be reasonably agitated to bring adsorbate molecules closer to the active sites of adsorbents. Influence of agitation speed on the removal of Malachite green (MG) by *S. asper* is shown in Fig. 4.7. From this figure, 150 rpm (revolution per minute) was the optimal speed for MG removal. Most of the researchers utilized between 100 and 200 rpm as optimal adsorption agitation speed depending on the nature of the system under investigation.

Generally, pollutants uptake by nanostructured materials is proportional to the agitation speed until a climax is reached after which an increase in speed tends to decrease or keep constant the uptake of pollutants. At extremely low or high agitation speed, adsorption process cannot be optimally achieved. Elevated agitation speed could trigger desorption due to breaking down of adsorbate molecules [34].

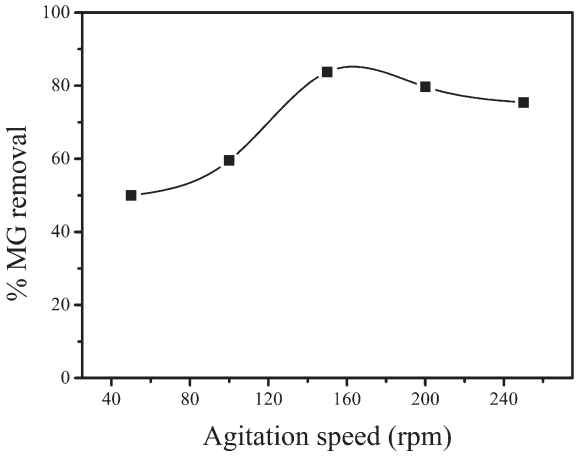

Fig. 4.7 Influence of agitation speed on Malachite Green removal by *S. asper*

Different pairs of adsorbate–adsorbent could have different optimum agitation speed, which could influence the adsorption capacity. Agitation speed should be considered and not assumed while investigating adsorptive systems.

4.9 Concluding Remarks

In this chapter, the main experimental factors and conditions that influence the adsorption batch process were discussed and correlated with examples reported in the literature. As elaborated, the textural properties of the adsorbents are very important factors that influence the adsorption process. The adsorption of small molecules occurs meanly at the micropores of an adsorbent, in contrast, higher molecules are mainly retained in the mesopores of an adsorbent. The microporous materials are characterized for higher surface area. The total pore volume is also important in the sorption capacity of an adsorbent, higher total pore volume of an adsorbent will lead to adsorbents of higher sorption capacity. Regarding the initial adsorbate concentration, this increase, usually, would lead to an increase in the amount adsorbed, until the adsorbent get saturated. Already the adsorbent dosage must be fixed at the threshold value, which is the adsorbent dosage that corresponds to the minimum amount of adsorbent that leads to constant adsorbate removal. The pH of the solution can influence the overall adsorption process and the adsorption capacity because different species can have different optimal pH ranges depending on the adsorbent used. Concerning the contact time, it is advisable to increase the contact time of the interaction between adsorbent and adsorbate beyond the equilibrium time to guarantee the proper equilibrium at higher concentration levels. Apropos the temperature changes, it could change the sorption capacity. An increase in temperature could increase, keep practically

constant or decrease the sorption capacity of a given adsorbate on a given adsorbent. Similarly, agitation speed of an adsorptive system has been found to influence adsorption capacity.

Acknowledgments The authors acknowledge funding from Brazilian agencies CNPq, CAPES, and TWAS.

References

1. Adebayo MA, Prola LDT, Lima EC et al (2014) Adsorption of Procion Blue MX-R dye from aqueous solutions by lignin chemically modified with aluminium and manganese. J Hazard Mater 268:43–50
2. Sing KSW, Everett PHR, Haul AW et al (1958) Reporting physisorption data for gas/solid systems with special reference to the determination of surface area and porosity. Pure Appl Chem 57:603–619
3. Dąbrowski A (2001) Adsorption—from theory to practice. Adv Colloid Interface Sci 93:135–224
4. Reedijk J, Poeppelmeie KR (2013) Comprehensive inorganic chemistry II, 2nd edn. Elsevier, Waltham, MA
5. Ioannatos GE, Verykios XE (2010) H_2 storage on single- and multi-walled carbon nanotubes. Int J Hydrogen Energy 35:622–628
6. de Menezes EW, Lima EC, Royer B et al (2012) Ionic silica based hybrid material containing the pyridinium group used as adsorbent for textile dye. J Colloid Interface Sci 378:10–20
7. Calvete T, Lima EC, Cardoso NF et al (2010) Application of carbon ad-sorbents prepared from Brazilian-pine fruit shell for the removal of reactive orange 16 from aqueous solution: kinetic, equilibrium, and thermodynamic studies. Environ Manag 91:1695–1706
8. Prola LDT, Acayanka E, Lima EC et al (2013) Comparison of *Jatropha curcas* shells in natural form and treated by non-thermal plasma as bio-sorbents for removal of Reactive Red 120 textile dye from aqueous solution. Ind Crop Prod 46:328–340
9. Schierz A, Zänker H (2009) Aqueous suspensions of carbon nanotubes: surface oxidation, colloidal stability and uranium sorption. Environ Pollut 157:1088–1094
10. Prola LDT, Machado FM, Bergmann CP et al (2013) Adsorption of Direct Blue 53 dye from aqueous solutions by multi-walled carbon nanotubes and activated carbon. J Environ Manag 130:166–175
11. Webb PA, Orr CA (1997) Analytical methods in fine particle technology. Micromeritics Instrument Corporation, Norcross, GA
12. Gupta VK, Saleh TA (2013) Sorption of pollutants by porous carbon, carbon nanotubes and fullerene—an overview. Environ Sci Pollut Res 20:2828–2843
13. Sui K, Li Y, Liu R et al (2012) Biocomposite fiber of calcium alginate/multi-walled carbon nanotubes with enhanced adsorption properties for ionic dyes. Carbohydr Polym 90:399–406
14. Li Y, Du Q, Liu T et al (2013) Comparative study of methylene blue dye adsorption onto activated carbon, graphene oxide, and carbon nanotubes. Chem Eng Res Des 91:361–368
15. Alencar WS, Lima EC, Royer B et al (2012) Application of aqai stalks as biosorbents for the removal of the dye Procion Blue MX-R from aqueous solution. Sep Sci Technol 47:513–526
16. Liao Q, Sun J, Gao L (2008) Adsorption of chlorophenols by multi-walled carbon nanotubes treated with HNO_3 and NH_3. Carbon 46:544–561
17. Pillaya K, Cukrowska EM, Coville NJ (2009) Multi-walled carbon nanotubes as adsorbents for the removal of parts per billion levels of hexavalent chromium from aqueous solution. J Hazard Mater 166:1067–1075

18. Faria AF, Martinez DST, Moraes ACM et al (2012) Unveiling the role of oxidation debris on the surface chemistry of graphene through the anchoring of Ag nanoparticles. Chem Mater 24:4080–4087
19. Pillaya K, Cukrowska EM, Coville NJ (2009) Multi-walled carbon nanotubes as adsorbents for the removal of parts per billion levels of hexavalent chromium from aqueous solution. J Hazard Mater 166:1067–1075
20. Ranga R, Conyers JL (2009) Biomedical applications of functionalized fullerene-based nanomaterials. Int J Nanomed 4:261–275
21. Ren X, Li J, Tan X, Wang X (2013) Comparative study of graphene oxide, activated carbon and carbon nanotubes as adsorbents for copper decontamination. Dalton Trans 42:5266–5274
22. Robinson T, Chandran B, Nigam P (2002) Effect of pretreatments of three waste residues, wheat straw, corncobs and barley husks on dye adsorption. Bioresour Technol 85:119–124
23. Ahmad R, Kumar R (2010) Conducting polyaniline/iron oxide composite: a novel adsorbent for the removal of amido black 10B. J Chem Eng Data 55:3489–3493
24. Machado FM, Bergmann CP, Fernandes THM et al (2011) Adsorption of Reactive Red M-2BE dye from water solutions by multi-walled carbon nanotubes and activated carbon. J Hazard Mater 192:1122–1131
25. Machado FM, Bergmann CP, Lima EC et al (2012) Adsorption of Reactive Blue 4 dye from water solutions by carbon nanotubes: experiment and theory. Phys Chem Chem Phys 14:11139–11153
26. Li YH, Di Z, Ding J, Wu D, Luan Z, Zhu Y (2005) Adsorption thermodynamic, kinetic and desorption studies of Pb^{2+} on carbon nanotubes. Water Res 39:605–609
27. Gupta VK, Nayak A (2012) Cadmium removal and recovery from aqueous solutions by novel adsorbents prepared from orange peel and Fe_2O_3 nanoparticles. Chem Eng J 180:81–90
28. Suksabye P, Thiravetyan P (2012) Cr(VI) adsorption from electroplating plating wastewater by chemically modified coir pith. J Environ Manag 102:1–8
29. Alencar WS, Acayanka E, Lima EC et al (2012) Application of *Mangifera indica* (mango) seeds as a biosorbent for removal of Victazol Orange 3R dye from aqueous solution and study of the biosorption mechanism. Chem Eng J 209:577–588
30. Cardoso NF, Lima EC, Royer B et al (2012) Comparison of *Spirulina platensis* microalgae and commercial activated carbon as adsorbents for the removal of Reactive Red 120 dye from aqueous effluents. J Hazard Mater 241–242:146–153
31. Ribas MC, Adebayo MA, Prola LDT et al (2014) Comparison of a homemade cocoa shell activated carbon with commercial activated carbon for the removal of reactive violet 5 dye from aqueous solutions. Chem Eng J 248:315–326
32. Calvete T, Lima EC, Cardoso NF, Dias SLP, Pavan FA (2009) Application of carbon adsorbents prepared from the Brazilian-pine fruit shell for removal of Procion Red MX 3B from aqueous solution—kinetic, equilibrium, and thermodynamic studies. Chem Eng J 155:627–636
33. Oladoja NA, Akinlabi AK (2009) Congo red biosorption on palm kernel seed coat. Ind Eng Chem Res 48:6188–6196
34. Omri A, Benzina M, Ammarb N (2013) Preparation, modification and industrial application of activated carbon from almond shell. J Ind Eng Chem 19:2092–2099

Chapter 5
Carbon Nanomaterials for Environmental Applications

Fernando Machado Machado, Éder Cláudio Lima, Iuri Medeiros Jauris and Matthew Ayorinde Adebayo

Abstract The qualities of waters are constantly diminishing due to release of toxic components into the environment. It is very important to treat wastewater in order to remove pollutants and improve water quality. Generally, adsorption technology has proven to be one of the most effective techniques in the separation and removal of a wide variety of organic and inorganic pollutants from wastewater. Recently, carbon nanomaterials such as fullerene, carbon nanotubes (CNT) and graphene-family have become promising adsorbents for water treatment. This chapter compiles relevant knowledge about the experimental and theoretical adsorption activities of fullerene, CNT and graphene-family as nanoadsorbents for removal of organic and inorganic environmental pollutants.

Keywords Adsorption · Nanoadsorbents · Ab initio calculations · Fullerene · Carbon nanotubes · Graphene-family · Wastewater

F.M. Machado (✉)
Centro de Desenvolvimento Tecnológico, Universidade Federal de Pelotas,
Pelotas, RS 96010610, Brazil
e-mail: fernando.machado@hotmail.com.br

É.C. Lima
Instituto de Química, Universidade Federal do Rio Grande do Sul,
Porto Alegre, RS 91501970, Brazil
e-mail: profederlima@gmail.com

I.M. Jauris
Área de Ciências Tecnológicas, Centro Universitário Franciscano,
Santa Maria, RS 97010032, Brazil
e-mail: iuri.jauris@gmail.com

M.A. Adebayo
Department of Chemistry, Federal University of Agriculture,
Abeokuta 110008, Ogun State, Nigeria
e-mail: adebayomao@gmail.com

C.P. Bergmann and F.M. Machado (eds.), *Carbon Nanomaterials as Adsorbents for Environmental and Biological Applications*, Carbon Nanostructures,
DOI 10.1007/978-3-319-18875-1_5

Abbreviations

AR-183	Acid Red 183
BPH A	Bisphenol A
COD	Chemical Oxygen Demand
CP	Chlorpyrifos
CNT	Carbon Nanotube
DB-53	Direct Blue 53 dye
DCL	Sodium Diclofenac
DFT	Density Functional Theory
DOX	Doxorubicin
EDC	Endocrine Disrupting Compounds
ES	Endosulfan
GO	Graphene Oxide
GNSs	Graphene Nanosheets
MB	Methyl Blue
ML	Malathion
MO	Methyl Orange
MWCNT	Multi-Walled Carbon Nanotube
NAPH	2-Naphthol and Naphthalene
PAC	Powdered Activated Carbon
RB-4	Reactive Blue 4
rGO	Reduced Graphene Oxide
RRM	Reactive Red M-2BE
SIESTA	Spanish Initiative for Electronic Simulations with Thousands of Atoms
SWCNT	Single-Walled Carbon Nanotube
TCB	1,2,4-Trichlorobenzene
TCP	2,4,6-Trichlorophenol

5.1 Introduction

Adsorption technology is considered, by several researchers, as the most promising technique of water treatment and purification. It is an extremely robust technique with high-efficiency at low cost. However, for a successful wastewater treatment, the correct choice of adsorbent is a major determining factor. Carbon-based nanomaterials have been extensively explored for adsorption applications because of their structural diversity, large specific surface area, small size, good chemical stability, low density, possible regeneration and reusability [1].

Fullerenes, which possess structures characterized with a spherical, ellipsoid, or cylindrical arrangement of dozens of carbon atoms [2] with high chemical and thermal stability and excellent electron acceptor, have been investigated as

potential adsorbents [1, 2]. The fullerenes have shown good sorption capacities for removal of organic pollutants such as aliphatic, cyclic and aromatic compounds from solutions [1, 3, 4].

Multi-walled (MWCNT) and single-walled carbon nanotubes (SWCNT) [5–7] have been shown as effective adsorbents for removal of many adsorbates. They are attractive and alternative adsorbents for removal of organic and inorganic contaminants from water due to high aspect ratio, high pore size and total pore volume, and large surface area [1, 8, 9].

The graphene, a single atomic layer of graphite [10], has been used in a number of investigations to study its applicability as a potential adsorbent for water purification. Recently, members of the graphene-family nanomaterials such as graphene oxide (GO), reduced graphene oxide (rGO) and graphene nanosheets have also emerged as a promising group of adsorbents for the removal of various environmental pollutants from aqueous effluents [1, 11, 12].

In this chapter, we present an overview of the current and available experimental and theoretical research on carbon nanomaterials such as fullerene, carbon nanotubes (CNT) and graphene-family for removal of toxic species such as synthetic dyes, drugs and pesticides, as well as metallic ions from aquatic systems. In addition, we briefly discuss the physical, chemical and structural properties of the interactions between the contaminants and the carbon nanomaterials to appraise the use of these nanoadsorbents in environmental applications.

5.2 Removal of Metallic Ions

The contamination of hydric systems by metallic ions such as Cu(II), Cd(II), Pb(II), Cr(III) and Cr(VI), Zn(II) and Ni(II) has steadily increased over the past few decades due to uncontrolled discharge of waste effluents from industries such as metal plating, mining, electroplating, smelting, tanneries, painting, printing and petroleum refining, as well as runoff from agricultural lands, where fertilizer and fungicidal spray are intensively used. These metallic ions tend to accumulate in living organisms and have potentially damaging effects on human physiology and other biological systems when the tolerance levels are exceeded [13, 14].

Numerous investigations have been undertaken to evaluate the removal capacity of metallic ions by CNT from water systems. In the subsequent paragraphs, recent advances in the adsorption of metallic ions from wastewaters by MWCNT and SWCNT are presented.

For metallic ions, the parameters such as pH and temperature play a fundamental role in CNTs sorption [15–18]. The influence of pH on the adsorption process was demonstrated in the adsorption of zinc from solutions by SWCNTs and MWCNTs purified with sodium hypochlorite solutions [15]. In the study the CNTs were purified by sodium hypochlorite solutions, which made the nanotubes become more hydrophilic and suitable for adsorption of Zn(II) from aqueous solutions. The adsorption process was pH-dependent; it increased, with low variations,

when the pH of the solution was increased from 1 to 8, it reached a plateau in the pH range of 8–11 and thereafter decreased at pH 12. The contact time to reach equilibrium is 60 min for SWCNTs and MWCNTs. The maximum adsorption capacities of Zn(II) calculated by the Langmuir model are 43.66 and 32.68 mg g^{-1} for SWCNTs and MWCNTs, respectively.

The operating temperature of adsorption process is an influential factor not only to the sorption rate, but also to the degree in which sorption occurs. The adsorption capacity of the CNTs is a function of temperature. This effect is evident in the adsorption of Zn(II) and Pb(II) [15, 16], indicating that an increment in temperature increases the amount of metal ions adsorbed. Similarly, the time requires to obtain 50 % of maximum sorption capacity ($t_{1/2}$) of Zn(II) was reached faster at higher operating temperatures [15].

The oxidation of CNTs can considerably improve the sorption capacity of metallic ions. In this regard, the sorption mechanism is attributable to chemical interaction between the metallic ions and the surface functional groups [19, 20]. In addition, adsorption of metallic ions on CNTs may involve other complex mechanisms such as electrostatic attraction and precipitation [19]. However, it is believed that the chemical interaction between metallic ions and functional groups at the surface of CNT is the major mechanism of adsorption [21].

Functionalized MWCNTs were employed as sorbent for Pb(II) from aqueous solution [16]. The sorption of Pb(II) using HNO_3-modified MWCNT was a fast process, and the kinetic sorption followed a pseudo-second-order model. The positive value of the enthalpy indicates that an increase in the temperature increases the amount of Pb(II) adsorbed by CNTs. The negative values of adsorption standard free energy changes and positive value of standard entropy changes indicate that the adsorption process is spontaneous. Desorption studies reveal that Pb(II) can be easily desorbed from MWCNTs by varying the pH of the solution using HCl and HNO_3 solutions. CNTs oxidized using alternative methods were also utilized for adsorption of Pb(II) from aqueous solutions [22]. Apart from the conventional ultrasonication method, the UV-radiation associated with HNO_3 was also used to oxidized SWCNTs and MWCNTs. The adsorption data were compared using Langmuir isotherm model. For SWCNTs, adsorption capacity value of UV-radiation method is 511.99 mg g^{-1} and that of ultrasonication method is 342.36 mg g^{-1}. For MWCNTs, the adsorption capacity value of UV-radiation method is 306.99 mg g^{-1} and that of ultrasonication method is 279.99 mg g^{-1}. The UV-radiation increased the surface acidity of the CNT more than ultrasonication, thereby increased the adsorption capacity. The adsorption mechanisms between the CNTs and Pb(II) ions were best described by pseudo second-order kinetic model. It shows that, the adsorption materializes between the metallic ions and surface functional groups of CNT. It is an ion-exchange reaction, and the rate-limiting step is the electron exchange between the lead ions and adsorbent surface.

The NaClO-oxidized MWCNTs and SWCNTs were reported as adsorbents for removal of Ni(II) from aqueous solutions [21]. The surface properties of CNTs were greatly changed after oxidation, including the rise in functional groups, total acidic sites, and negatively charged carbons. These modifications made CNTs

become more hydrophilic and led to more Ni(II) adsorption. The adsorption mechanisms are attributable to chemical interactions and electrostatic forces between the Ni(II) and the surface functional groups of CNTs. The Ni(II) removal by CNTs increased rapidly in the range pH 1–8, suffered a slight change and reached a maximum in the range 8–11, and steeply decreased at pH 12. Furthermore, the amount of Ni(II) sorbed onto oxidized CNTs increased when agitation speed was increased at a specific initial Ni(II) concentration, but decreased when mass of CNTs and ionic strength of the adsorbate solution were increased.

Using a batch technique, MWCNTs and functionalized MWCNTs were employed for the adsorption of Cu(II) from aqueous solutions [23]. The results revealed that modification increased the adsorption capacity because functional groups appeared on the functionalized MWCNT surface. The appearance of these groups not only increased the active area of adsorption sites of CNTs, but also increased the proportion of available adsorption sites. The negatively charged surface of functionalized MWCNTs electrostatically favors the adsorption of Cu(II) onto $H_2SO_4/KMnO_4$-modified MWCNTs than that of H_2SO_4-modified MWCNTs. Additionally, the adsorption capacity of Cu(II) onto as-grown MWCNTs and functionalized MWCNTs surface increased as temperature was increased. The Langmuir isotherm gave the best fit of the experimental data and the maximum adsorption capacities of Cu(II) calculated by this model at 320 K are 6.2, 18.3 and 42.7 mg g^{-1} for as-grown MWCNTs, H_2SO_4-modified MWCNTs and $H_2SO_4/KMnO_4$-modified MWCNTs, respectively. The positive enthalpy values demonstrated that the adsorption of Cu(II) onto all MWCNTs is endothermic—a result supported by the increase in the adsorption of Cu(II) with temperature.

The Cd(II) removal from solution using MWCNTs oxidized with H_2O_2, $KMnO_4$ and HNO_3 was reported [18]. The results of the influence of pH and MWCNTs dosage on the Cd(II) adsorption show that the increase of Cd(II) adsorption capacity for $KMnO_4$ oxidized MWCNTs is greater than those of the as-grown MWCNTs, H_2O_2 and HNO_3 oxidized MWCNTs. The Cd(II) adsorption capacity of the as-grown MWCNTs is only 1.1 mg g^{-1}, while it reaches 2.6, 5.1 and 11.0 mg g^{-1} for the H_2O_2, HNO_3 and $KMnO_4$ oxidized MWCNTs, respectively. Furthermore, the authors demonstrated that adsorption of Cd(II) by MWCNTs was strongly pH-dependent and the increase of adsorption capacities for HNO_3 and $KMnO_4$ oxidized MWCNTs are more obvious than those of as-grown and H_2O_2 oxidized MWCNTs at lower pH regions.

The removal of hexavalent chromium (Cr(VI)) from aqueous solutions, using functionalized (oxidized) and non-functionalized MWCNTs, has also been studied [24, 25]. The removal of Cr(VI) from aqueous solutions on oxidized MWCNTs is favored at low pH values (maximum removal at pH < 2 [24]). The maximum adsorption capacity of Cr(VI) calculated by the Langmuir model was 4.3 mg g^{-1} at pH = 2.05. The major mechanisms for removal Cr(IV) as identified are: intraparticle diffusion, electrostatic interactions and redox reactions [24]. The latter appears as the main mechanism for adsorption of chromium by MWCNTs. The redox reaction between the adsorption of Cr(VI) and the surface of oxidized MWCNTs leads to the formation of Cr(III) and subsequently the sorption

of Cr(III) on MWCNTs (On the MWCNT surface exists both Cr(VI) and Cr(III) species). Removal of Cr(VI) is effective and without significant release of Cr(III) to the environment. The non-functionalized MWCNTs show a higher adsorption capacity than the functionalized MWCNTs [25]. This is because the functionalized MWCNTs contain electron rich atoms in their functional groups, which repel the negatively charged dichromate ions that inhibit the adsorption process. Both functionalized and non-functionalized MWCNTs possess adsorption capacities higher than that of activated carbon [25].

CNTs have been investigated for the adsorption of multi-metals ions from wastewaters. MWCNTs have been used for simultaneous adsorption of Cd(II), Pb(II), Cu(II) and Zn(II) at 298 K [20]. The binding of these metal ions by MWCNT was found to follow the following order: Cu(II) > Pb(II) > Zn(II) > Cd(II). The kinetics of adsorption these metallic ions on MWCNTs were analyzed using different kinetic models, but the pseudo second-order model best described the adsorption processes of the heavy metallic ions. The thermodynamics study showed that the adsorption process is spontaneous in the experimental temperature range and becomes more spontaneous by raising the temperature of the solution. The positive values of enthalpy for the adsorption of Pb(II), Cd(II), Cu(II), and Zn(II) by MWCNTs from an aqueous solutions indicate the endothermic nature of the metal ions adsorption. The changes in entropy have positive values, which indicate an increase in randomness due to the physical adsorption of metallic ions from the aqueous solutions to the CNT surface.

Coupled with high adsorption capacity of metallic ions, the regeneration of CNT can be easily achieved by changing the pH of the solution, without a significant decrease on the performance of the CNTs—indicating that CNTs are promising adsorbents for the treatment of effluents contaminated with metallic ions [15, 16].

Due to textural properties of graphene, many investigations have been carried out on graphene as an adsorbent to remove metallic ions from aqueous solutions [12, 14]. The possibility of the removal of Sb(III) using graphene as adsorbent from aqueous solutions has been explored [26]. Batch adsorption experiments were performed to investigate the influence of operating parameters such as solution pH, initial Sb(III) concentration, temperature and contact time on the adsorption process. An increase in the efficiency of Sb(III) removal was observed at pH higher than 3.8, and a maximum removal (about 99.5 %) was observed at pH > 11. The adsorption capacity decreased with increasing Sb(III) concentrations, but it increased with increasing temperature. The Freundlich isotherm fitted well the experimental data and the maximum adsorption capacities of Sb(III). The adsorption kinetic data best fitted into the pseudo-second-order model and the model suitably interpret the overall adsorption process, demonstrating that the rate determining step is chemisorption. The Sb(III) loaded graphene could be regenerated, using 0.1 mol L^{-1} ethylenediaminetetraacetic acid disodium salt as a desorbing agent [26].

Graphene nanosheets obtained by vacuum-promoted low-temperature (500 and 700 °C) exfoliation were used to adsorb Pb(II) from aqueous solutions [27]. The adsorption process was pH-dependent; increases with the increase in pH in the pH

range 2–8. It is hypothetical that the Lewis basicity of nanosheets is improved by heat treatment under a high vacuum, in favor of simultaneous adsorption of Pb(II) and protons onto GNSs. The maximum adsorption capacities of Pb(II) calculated by the Langmuir model was 35.46 mg g^{-1} for heat-treatment GNS at 700 °C.

The adsorption of Cr(III) on GO from aqueous solutions [28] was strongly dependent on solution pH, but feebly dependent on ionic strength. The adsorption of Cr(III) increased between pH 1.0 and 6.0. At low pH, the low adsorption capacity of adsorbent can be attributed partially to the competition between the excess proton in solution and Cr(III) for the same binding sites on nanoadsorbate surface. The pseudo-second-order model described well the adsorption kinetic data. The equilibrium data were well fitted by Langmuir model and the maximum adsorption capacity at pH 5.0 and 296 K was 92.65 mg g^{-1}. The calculated thermodynamic parameters indicated that the adsorption of Cr(III) on GO was spontaneous, endothermic and the magnitude of enthalpy was comparable with that of electrostatic interaction between a nanoadsorbent and an adsorbate.

The GO prepared using modified Hummer's method was used as adsorbent for removal of Cu(II) from aqueous solution [29]. The oxygenous functional groups on the surface of adsorbent were mainly responsible for the adsorption of ions. The effects of the parameters such as pH value, adsorbate concentration, adsorbent dosage and contact time on adsorption were examined. The best conditions for Cu(II) removal by GO were: solution pH = 5.3, adsorbent dosage of 1 mg mL^{-1} and an equilibrium contact time of 150 min. The equilibrium adsorption data fitted well to the Freundlich isotherm model with maximum sorption capacity of 117.5 mg g^{-1}. The adsorption of Cu(II) on GO was mainly credited to surface complexation, ion exchange, and electrostatic attraction. The Cu(II) loaded GO could be regenerated using HCl. The reusability of the carbon nanoadsorbent could still maintain >90 % of its initial capability after ten adsorption–desorption cycles [29].

The adsorptive properties of GO towards Cu(II), Zn(II), Cd(II) and Pb(II) from aqueous solutions were investigated [30]. The GO was prepared through the oxidation of graphite using potassium dichromate. The results of batch experiments indicate that maximum adsorption can be achieved in broad pH ranges: 3–7 for Cu(II), 5–8 for Zn(II), 4–8 for Cd(II) and 3–7 for Pb(II). The maximum adsorption capacities of GO for Cu(II), Zn(II), Cd(II) and Pb(II) at pH = 5, calculated by the Langmuir model, were 294, 345, 530, 1119 mg g^{-1}, respectively. The competitive adsorption experiments demonstrated the attraction in the order of Pb(II) > Cu(II) ≫ Cd(II) > Zn(II). Adsorption kinetic and isotherms studies suggest that sorption of the metallic ions on sheets is monolayer coverage and adsorption is controlled by chemical adsorption involving the strong surface complexation of metal ions with the oxygen-containing groups on the surface of nanoadsorbent [30].

The rGO prepared by the reduction GO using thiourea dioxide was used for adsorption of Th(IV) from water [31]. The adsorption of Th(IV) on rGO as a function of pH, adsorbent dosage, adsorbate initial concentration, temperature and contact time was investigated through batch adsorption process. The removal efficiency of Th(IV) increases as pH increases from 1.0 to 6.0. The adsorption

efficiency of adsorbate was low at pH value below 3 due to the protonation of residual oxygenous functional groups on rGO and the competition between H^+ and Th(IV) for the same adsorption site. The results showed that the adsorption behavior of Th(IV) on rGO followed the Langmuir isotherm and the pseudo-second order kinetic models. The maximum adsorption capacity was calculated to be 0.21 mmol Th g^{-1} rGO at 298.15 K. The thermodynamic parameters indicated that the adsorption process was endothermic, spontaneous and the magnitude of enthalpy suggesting that the mechanism of the adsorption process was that of physical adsorption of an adsorbate on a nanoadsorbent.

5.3 Removal of Dye

Many industries such as textile, paper, feedstuffs, cosmetics, and leather, among others utilize dyes to color their products, and consequently produce large amounts of wastewaters containing this organic pollutant [32]. During manufacturing processes, 10–60 % of dyes are lost—generating large quantities of colored wastewaters [33]. The presence of dye-containing waters can adversely affect the aquatic environment by obstructing light penetration and reducing photosynthetic rate of aquatic flora [34]. Furthermore, most of these dyes can cause skin irritation, allergy, dermatitis, and can also induce cancer and cell mutation [35]. Dyes are organic compounds characterized with complex aromatic molecular structures that can provide bright and firm colour to other materials. Dyes are stable and difficult to biodegrade because of their structures [36]. In this regards, dye-containing effluents require treatment before being released into the environment [8].

As discussed in the previous chapters, one of the unitary operations vastly employed for the removal of synthetic dyes from aqueous effluents is the adsorption technique [8]. Different adsorbents have been used for the removal of synthetic dyes from aqueous solutions [32, 34]. From this scenario, the usage of carbon nanomaterials as nanoadsorbent have been successfully employed for the removal of several dyes from aqueous effluents [1, 37].

Carbon nanotube, because of its characteristic structures highlighted in Chap. 2, is one the adsorbents mostly employed for the successful removal of dyes from aqueous effluents [38–40]. Carbon nanomaterials are attracting attention as nanoadsorbents for removal of these organic pollutants. CNTs interact strongly with organic molecules via non-covalent forces such as hydrogen bonding, π–π stacking, electrostatic forces, van der Waals forces and hydrophobic interactions [1].

CNTs were efficient for removal of direct dyes such as Direct Yellow 86 and Direct Red 224 [41] and cationic dyes such as Methylene Blue [42]. The analysis indicated that the thermodynamics of adsorption of both direct dyes and the cationic dye were endothermic and spontaneous [41, 42]. In addition, the adsorption of both dyes occurs through physisorption process [41, 42]. The adsorption of reactive dyes such as Reactive Red 2 onto MWCNTs has also been considered [43]. The results suggest that the adsorption of reactive dye on MWCNTs

decreases as pH increases, but increases as temperature increases. As with direct and reactive dyes, the adsorption of Reactive Red 2 occurred spontaneously through physisorption process [43].

MWCNTs show better adsorption than powdered activated carbon (PAC) for Reactive Red M-2BE dye (RRM) [8] and Direct Blue 53 dye (DB-53) [44] from aqueous solutions, under optimum conditions of pH = 2.0 and temperature range of 298 and 323 K. The contact time to obtain equilibrium isotherms at 298–323 K was fixed at 3 and 1 h for DB-53 and RRM, respectively. For DB-53 dye, the equilibrium data (298–323 K) were best fitted to the Sips isotherm model. However, the equilibrium data of RMM dye were best fitted to the Liu isotherm model. For adsorption of the dyes by MWCNTs, the maximum sorption capacities obtained at 323 K were 409.4 and 335.7 mg g^{-1} for DB-53 and RRM, respectively. The general order kinetic model and Avrami fractional-order kinetic model best described the kinetic data of DB-53 and RMM, respectively. The faster kinetics of adsorption of dyes on MWCNT compared to PAC was attributed to the textural properties of the MWCNTs, where the aggregated pores expanded when immersed in aqueous solutions, increasing the volume of the aggregated pores [8]. For both cases, the enthalpy of adsorption indicated that adsorption process was endothermic and the magnitudes of enthalpy were consistent with that of electrostatic interaction between the adsorbents and the adsorbates. Studies of adsorption/desorption show that MWCNT can be regenerated from DB-53-loaded MWCNT and RMM-loaded MWCNT using a 50 % acetone + 50 % of 3 mol L^{-1} NaOH [44] and Methanol + 4.0 mol L^{-1} NaOH [8], respectively.

Adsorption of Methyl Orange dye (MO) on MWCNTs from aqueous solutions was investigated [45]. The results showed that the adsorption capacity increased with increasing temperature, agitation speed and dye concentration. MO dye adsorption per gram of MWCNTs decreases with the rise in the MWCNTs mass in the solution. The pseudo-second-order kinetic model gave the best fit of the kinetic experimental data.

MWCNTs and SWCNTs were used as nanoadsorbents for the removal of Reactive Blue 4 (RB-4) textile dye from aqueous solutions [9]. In the acidic region (pH = 2.0), the adsorption of RB-4 dye on both CNTs was a favorable process. The contact time to obtain equilibrium isotherms at 298–323 K was fixed at 4 h for both adsorbents. The general order kinetic model provided the best fit to the experimental data for both CNTs. For RB-4 dye, the equilibrium data (298–323 K) were best fitted to the Liu isotherm model. The maximum sorption capacities for adsorption of the dye occurred at 323 K, attaining values of 502.5 and 567.7 mg g^{-1} for MWCNT and SWCNT, respectively. The maximum amount of RB-4 dye adsorbed on SWCNT was 13.0 % higher than the value obtained for MWCNT. The textural characteristics CNTs justified this difference. Although the MWCNTs present a higher average pore diameter compared to SWCNTs, the specific surface area and total pore volume of SWCNTs were 114.3 and 91.9 %, respectively, higher than those of MWCNTs. The enthalpy of adsorption indicated that adsorption was an endothermic process. The interaction of RB-4 dye with (8,0) SWCNTs was investigated using first principles calculations based on

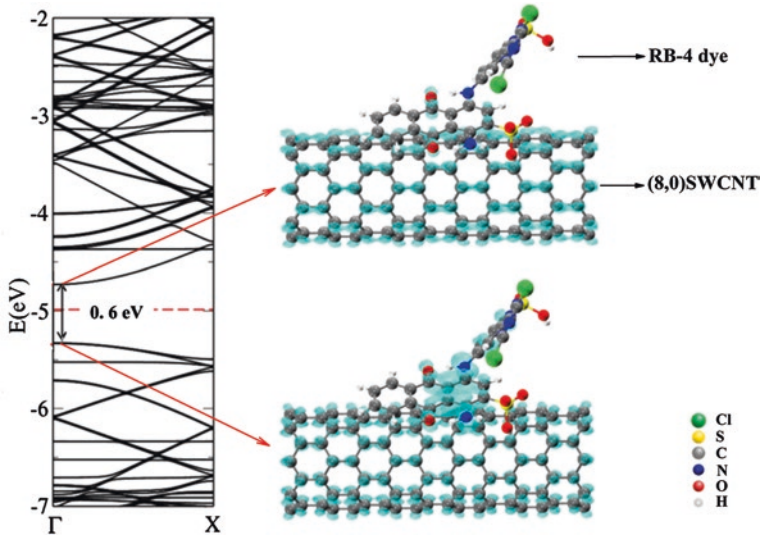

Fig. 5.1 Band structure and local density of states to the RB-4 dye adsorbed on (8,0) SWCNT

Density Functional Theory (DFT) (Fig. 5.1). Results from ab initio calculations indicated that RB-4 textile dye could be adsorbed on (8,0) SWCNT through an electrostatic interaction (energy binding $\approx$ 0.78 eV or 75.26 kJ mol^{-1}). These results are in agreement with the experimental predictions [9].

The adsorption of Acid Red 183 (AR-183) dye RB-4 dye on MWCNTs was investigated in single and binary dye systems [46]. The MWCNTs presented a higher adsorption of RB-4 than AR-183 in single and binary dye systems, due to stronger adsorbate-adsorbent interactions. In a single dye system, RB-4 and AR-183 adsorption followed pseudo second-order kinetics, and the isotherm was fitted by the Langmuir isotherm. In this system, the adsorption capacities of the MWCNTs for RB-4 and AR-183 at 298 K are 69 and 45 mg g^{-1}, respectively. Higher temperature lowered adsorption of both dyes on the MWCNTs. In binary dye systems, RB-4 and AR-183 showed competitive adsorption, resulting in RB-4 adsorption but desorption of AR-183 from the MWCNTs. The RB-4 adsorption capacity in binary dye systems was also reduced to 56 mg g^{-1} at 298 K. The interaction of the RB-4 and AR-183 dyes with MWCNTs was dominated by electrostatic attraction [46].

Graphene-family has been widely explored as nanoadsorbents for successful removal of dyes from aqueous effluents [12]. A relevant study in this area reported the adsorption of acrylonitrile, p-toluenesulfonic acid, 1-naphthalenesulfonic acid and Methyl Blue (MB) on graphene [47]. In this study, it was demonstrated that organic chemicals with larger molecular size and more benzene rings possessed a higher adsorption speed and a higher maximum adsorption capacity. Specifically in the case of MB dye, the results showed an adsorption capacity of 1.52 g g^{-1}.

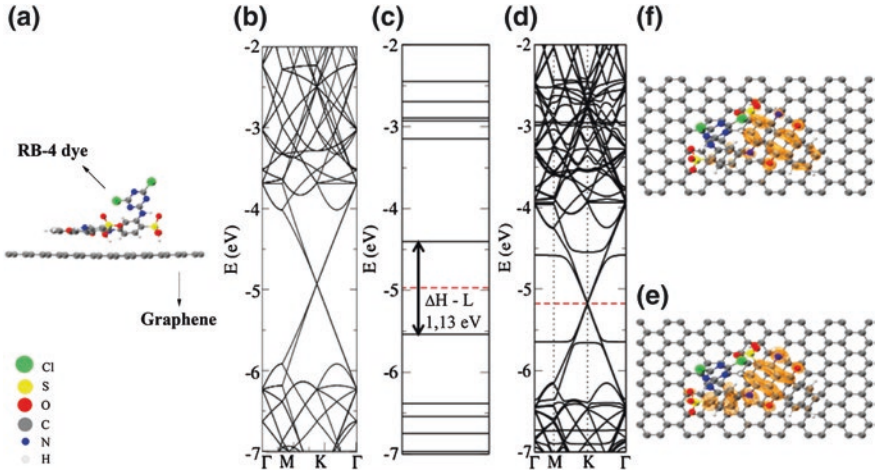

Fig. 5.2 Results for the most stable system found for the adsorption of RB4-dye on graphene. **a** Geometric structure of the interacting system. Electronic levels for isolated graphene (**b**) RB4-dye (**c**); RB4-dye adsorbed on graphene (**d**). Electronic charge density plots for **e** valence levels from −5.8 to −5.5 eV and **f** conduction levels from −4.7 to −4.4 eV. The horizontal *dashed red lines* indicate the Fermi energy

The adsorption occurred through π–π stacking interactions as inferred by fluorescence spectroscopy studies. Yet, the large amount of dye adsorbed was dependent on the initial concentration of dye. The thermodynamic analysis showed spontaneous and endothermic nature of the adsorption process. The researchers also investigated the possibility to regenerate and reuse graphene and observed no significant changes in the efficiency of graphene at least during the first five cycles of the adsorption–desorption process [47].

Nevertheless, even with a wide range of experimental studies available on literature, it is also required to develop a better understanding of the mechanism of dye adsorption on graphene. To this purpose, we have performed ab initio simulations based on the DFT to evaluate the interaction between graphene and GO and the RB-4 dye (Fig. 5.2). Thereby, several configurations with RB-4 dye interacting with graphene and graphene plus vacancy were performed. The results showed that the most stable configurations to adsorption in graphene exhibit an average binding energy of about 1.17 eV (or 112.89 kJ mol^{-1}). When a vacancy was added to graphene, the binding energy presented a small fluctuation 1.22 eV depending on the configuration studied. This observation may indicate a predominance of π–π interactions between the dye and the planar surface of graphene. However, when a vacancy was added on basal plane of graphene there was a significant contribution of electrostatic interactions between the reactive sites of RB-4 dye and the incomplete sp^2 bonding in the vacancy. Nevertheless, as the vacancies are becoming larger, one can notice a small decrease in energy, which may indicate a decrease in π–π interactions.

5.4 Removal of Drugs and Emerging Contaminants

A large amount of drugs from different classes is consumed annually worldwide. These pharmaceuticals include antipyretics, analgesics, lipid regulators, antibiotics, antidepressants, chemotherapeutic agents, contraceptive drugs and others [48]. After use, these compounds are partially metabolized and excreted in urine and feces and subsequently enter the sewage treatment plants, where the drugs remnants are treated, together with other organic and inorganic components of effluent. However, it has been shown that some of these drugs are not completely removed in the sewage treatment plants [49]. As a result, these compounds are found in effluents of municipal sewerage systems as well as in surface and ground waters. Similarly, some veterinary drugs have been found in aquatic environment.

SWCNTs, MWCNTs and oxidized MWCNTs were evaluated as adsorbents of ibuprofen and triclosan as representative types of pharmaceutical and personal care products, respectively, under different chemical solution conditions [50]. The sorption capacities of ibuprofen and triclosan on CNTs were pH-dependent and decreased with increasing pH. A good fitting of sorption isotherms was obtained using a Polanyi Manes model. The maximum sorption capacities of ibuprofen onto MWCNTs (81.6 and 186.5 $\mu g\ mg^{-1}$ for pH 7 and 4, respectively) were approximately 3 times lesser than those of SWCNTs (231.5 and 496.1 $\mu g\ mg^{-1}$ for pH 7 and 4, respectively). SWCNT has higher specific surface area and pore volume than MWCNT. Maximum sorption capacities of triclosan are 1.3 times higher for SWCNTs (558.2 and 133.0 $\mu g\ mg^{-1}$ at pH 7 and 4, respectively) than for MWCNTs (434.7 and 103.5 $\mu g\ mg^{-1}$ for pH 7 and 4, respectively), but the normalized maximum sorption capacity values for SWCNT (0.55 and 0.13 mg m^2 for pH 7 and 4, respectively) are lesser than for MWCNTs (1.54 and 0.37 mg m^2 for pH 7 and 4, respectively). The maximum sorption capacities of ibuprofen and triclosan for oxidized MWCNT were approximately four times lesser than those of pristine MWCNT. This is because both triclosan and ibuprofen contain ionizable phenolic or carboxylic acid groups, their adsorption varied more noticeably with oxidation of the CNT [50].

The adsorption of two antibiotics, lincomycine and sulfamethoxazole on single-walled and multi-walled CNT, was investigated using batch adsorption experiments [51]. The adsorption data were compared with those of PAC. Adsorption isotherms of the two antibiotics on carbon adsorbents were nonlinear and described by Freundlich isotherm model. The adsorption generally followed the order: SWCNT > PAC > MWCNT. The authors attribute the low adsorption capacity of antibiotics onto MWCNT to the lower specific surface area of the MWCNT, compared to other carbon materials [51]. Since the two studied pharmaceuticals are very hydrophilic, the sorption mechanism was attributed to electrostatic interactions and hydrogen bonds.

The adsorption and desorption of doxorubicin (DOX) on oxidized multi-walled CNT under different conditions were systematically measured [52]. The study shows that the oxidized MWCNTs are appropriate carriers of DOX. The

equilibrium data were best fitted to the Langmuir isotherm model. The maximum sorption capacity for adsorption of the DOX was 1.03×10^3 mg g^{-1} at 2 h incubation and the 10 days experiment was much higher (9.45×10^3 mg g^{-1}). The slow adsorption kinetics made the full loading of DOX on oxidized MWCNTs very difficult. The very slow adsorption kinetics of DOX onto oxidized MWCNTs was attributed to the formation of sludge-like stacking of DOX on MWCNT surfaces. The data were fitted to the pseudo-second-order model. The desorption of DOX from oxidized MWCNTs in buffer solution was very difficult at pH 7.4 and 5.5. This could be significantly facilitated by the protein competition, lower pH value and short adsorption time.

The removal of endocrine disrupting compounds (EDC) from water has attracted considerable attention because of their interference with human reproductive systems by blocking the activity of natural hormones [53–55].

Adsorption of EDC 17R-ethinyl estradiol and bisphenol A (BPH A) on fullerene was investigated [3]. This study indicated that surface area is a major factor for 17R-ethinyl estradiol and BPH A adsorption on fullerene. BPH A adsorption capacity is higher than 17R-ethinyl estradiol on fullerene. The molecular conformation simulation indicated that BPH A has a unique ability to adsorb on the curvature surface of fullerene because of its "butterfly" structure of two benzene rings. The higher adsorption capacity of BPH A over 17R-ethinyl estradiol is well explained by considering helical (diagonal) coverage of BPH A on the fullerene surface and wedging of BPH A into the groove and interstitial region of fullerenes bundles or aggregates.

The adsorption of EDC such as 7α-ethinyl estradiol and BPH A, from brackish water, artificial seawater or the combination thereof using SWCNTs as adsorbent was evaluated [53]. Linearized Freundlich and Langmuir models were used to fit the isothermal data of the adsorption of BPH A and 7α-ethinyl estradiol by SWCNTs in the various types of water sources. The results show higher removal efficiency for 17α-ethinyl estradiol (95–98 %) than for BPH A (75–80 %). Changes in the water chemistry conditions of the water sources did not considerably influence the overall adsorption of EDCs. However, changing the pH of the water source from 3.5 to 11 showed a decrease in the adsorption of BPH A, it did not affect the removal of 7α-ethinyl estradiol. The hydrophobic interactions between the EDCs and the SWCNTs may be the dominant removal mechanism. However, another possible mechanism for adsorption of EDCs, is perhaps π–π electron donor-acceptor interactions [53].

As previously discussed, organic pollutants such as drugs and others emerging contaminants, could be highly toxic and can induce genotoxicity, carcinogenicity, mutagenicity, teratogenicity, immunotoxicity and physiological effects [56, 57]. Drugs and emerging contaminants have high chemical oxygen demand (COD) and low biodegradability that are harmful to aquatic organisms even at a low concentration [56, 58]. In the literature, one can find several studies related to the adsorption of this class of compounds on graphene-family [12].

Using a batch technique, graphene was used for adsorption and decontamination of BPH A, from aqueous solution. In that case, the maximum adsorption

capacity of graphene for BPH A from the linearized Langmuir model equation was estimated to be 181.82 mg g^{-1} at 302.15 K. The adsorption of BPH A on graphene was essentially maintained by interactions such as hydrogen bonding and π–π interactions. Moreover, the adsorption capacity of graphene for BPH A showed no significant variation in a wide pH range of 2.0 and 7.0. However, at pH 8.0 and 9.0, respectively, BPH A suffered two successive deprotonations and graphene was negatively charged over the whole pH scale. This fact contributes to a decrease in the adsorption capacity of graphene for BPH A in the alkaline pH range, due to strong electrostatic repulsion between the negatively charged graphene surface and the bisphenolate anion. In addition, through thermodynamic studies, the adsorption process was spontaneous and exothermic. Finally, it was concluded that graphene could be considered as a promising adsorbent for removal of BPH A.

The theoretically and experimentally studies of the adsorption characteristics of 1,2,4-trichlorobenzene (TCB), 2,4,6-trichlorophenol (TCP), 2-naphthol and naphthalene (NAPH) on graphene and GO have been reported [59]. The results showed that graphene had nearly similar adsorption capacity for all the four organic contaminants at pH 5.0 while the adsorption capacity are in the order: naphthalene < 1,2,4-tricholorobenzene < 2,4,6-trichlorophenol < 2-napthol for GO. Besides, micro Fourier transform interferometer analysis revealed that TCB, TCP and 2-naphthol were adsorbed on graphene mainly via π–π interaction. In contrast, high adsorption of TCP and 2-naphthol on GO was attributed to the formation of H-bonding between hydroxyl groups of TCP and 2-naphthol and O-containing functional groups on GO. Moreover, the theoretical results was in complete agreement with the experimental data [59].

In both cases above, it was concluded from the study that graphene or GO could be potentially used as adsorbent for removal of pollutants. In addition, it was inferred that the interactions between the pollutants and graphene or GO occurred primarily through π–π interaction or H-bonding. These conclusions seem to agree with several other studies reported in literature [12]. Nevertheless, some differences on the adsorption mechanism of several compounds have been noticed. For instance, in some papers, it was reported that pH does not interfere with adsorption process, whereas in some other cases the assertion is not true. Furthermore, some cases did not find significant differences for adsorption capacities of different compounds on graphene or GO. To explain this observation, a better understanding of the adsorption mechanism is necessary.

To understand the mechanism required for adsorption of some drugs on graphene, we have performed ab initio simulations based on the DFT theory to evaluate the interaction between graphene and GO with Sodium Diclofenac (DCL) (Fig. 5.3). We performed several configurations to interact this drug with graphene, graphene plus vacancy, graphene plus functional groups—epoxy, hydroxyl, carboxyl and carbonyl. The results showed that the most stable configuration to DCL, adsorbed in a pristine graphene, exhibit an average binding energy *ca* 0.80 eV (or 77.2 kJ mol^{-1}), a characteristic of physical adsorption, which indicates a predominance of π–π interactions. On the other hand, if a vacancy is added to graphene, the binding energy shows an increase of about 0.20 eV. This

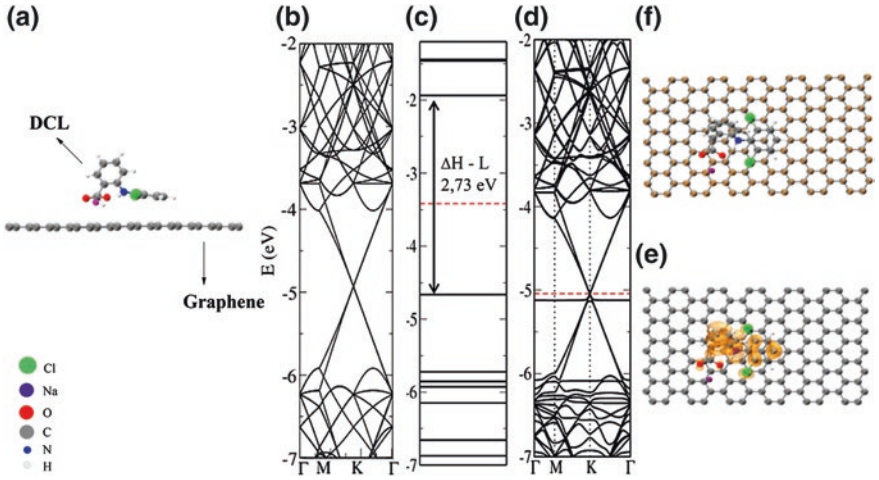

Fig. 5.3 Results for the most stable system found for the adsorption of DCL on graphene. **a** Geometric structure of the interacting system. Electronic levels for isolated graphene (**b**) Diclofenac (**c**); Diclofenac adsorbed on graphene (**d**). Electronic charge density plots for **e** valence levels from −5.3 to −5.1 eV and **f** conduction levels from −4.3 to −4.1 eV. The horizontal *dashed red lines* indicate the Fermi energy

is clearly a contribution of electrostatic interactions between the –COO– group of DCL and the incomplete sp^2 bonding in the vacancy. The presence of these electrostatic interactions is also corroborated when the DCL is adsorbed on functionalized graphene. In this case, the adsorption of DCL on functionalized graphene, with hydroxyl and epoxy groups, leads to a significant increase in binding energy. Furthermore, a greater binding energy was found when the adsorption of DCL occurred through carboxyl and carbonyl groups. This is an evidence of more effective interaction such as hydrogen bonding, apart from electrostatic and π–π interactions between DCL and GO, The understanding of these mechanisms of adsorption is quite important for future applications of graphene-family as nanoadsorbent materials.

Several chemical substances present different levels of toxicity, which can lead to acute or chronic damage in living organisms and bring risks to environment. Among these toxic substances are the pesticides, which are widely used to destroy or control plagues that are of no interest to farmers [60, 61]. After pesticides are applied to plants, they are commonly retained in fruits and grains. The first rain or dew of the night, can carry these pesticides to the ground, and thus contaminate rivers, lakes, among others [60, 61]. In general, one can refer to pesticides as agrochemical compounds such as herbicides, fertilizers and fungicides. These agrochemical compounds are also included in a class of organic pollutants.

In several published papers, sorption on CNTs has been examined for different compounds such as triazines, sulfonylureas, phenoxyalkanoic, organophosphorous pesticides, organochloride pesticides, and multi-class [62]. Removal of diuron

from aqueous solutions using oxidized MWCNT and MWCNTs has been studied [63], and the amount of diuron adsorbed was dependent on parameters such as solution pH, temperature and ionic concentration.

Pesticides are of the major concern due to their indiscriminate use and widespread presence in drinking water. The toxicity and health hazards posed by pesticides, even at very low concentrations, have become major concern for developing and developed countries [64]. The possibility of using GO as an alternative adsorbent for aniline removal from aqueous solution was reported [65]. The results show that the pH medium, adsorbent dosage, temperature, contact time and initial concentration are important parameters that can influence the maximum adsorption capacity. The study showed that GO could be used as an efficient adsorbent material for the adsorption of aniline from aqueous solution.

The adsorption capacity of Chlorpyrifos (CP), Endosulfan (ES) and Malathion (ML) pesticides by GO and rGO, from aqueous solution, was evaluated [64]. In this study, the adsorption capacities of CP, ES and ML by carbon nanostructures are as high as ~1200, 1100, and 800 mg g^{-1}, respectively. Adsorption process was insensitive to pH or background ions, which is an uncommon observation. Another important conclusion from this study is that since the adsorption on rGO was pH-independent, the surface functional group (–COO-) present on the rGO surface must not be involved in the adsorption of pesticides. Moreover, they proved that the adsorbent could be reused and potentially applied in the field of adsorption under suitable modifications. Furthermore, through first-principle calculations based on the DFT, the graphene materials–water–pesticide interactions showed that the adsorption is mediated through water, while direct interactions between graphene materials and the pesticides is rather weak or unlikely. Actually, the authors found that the pesticide adsorption on graphene materials is thermodynamically feasible only in the presence of water molecules [64].

With the aim of exploring the physical, chemical and structural properties of the interaction between pesticides and graphene materials, we have performed ab initio simulations based on the DFT to evaluate the interaction between graphene and GO with the atrazine (ATR) and pentachlorophenol (PCP) molecules (Figs. 5.4 and 5.5, respectively). Therefore, we performed several configurations with the two molecules interacting with graphene, graphene plus vacancy, graphene plus functional groups—epoxy, hydroxyl, carboxyl and carbonyl—(to simulate a GO), and graphene nanoribbons (to evaluate edge effects). It is important to emphasize that in the simulation of GO, we took into consideration that the epoxy, and hydroxyl groups are predominantly located on the basal plane of the graphene, whereas the carboxyl and/or carbonyl are mostly located on the edges of the graphene, in accordance with what has been reported [66]. The results showed that the most stable configurations of adsorption in graphene exhibit an average binding energy of 0.74 eV (or 71.4 kJ mol^{-1})—a characteristic of physical adsorption. Graphene with a vacancy has lower binding energy than graphene without vacancy for adsorption of both molecules. This observation may indicate a predominance of π–π interactions between the molecules and the planar surface of graphene. The observation occurs because the creation of a vacancy on graphene decreases

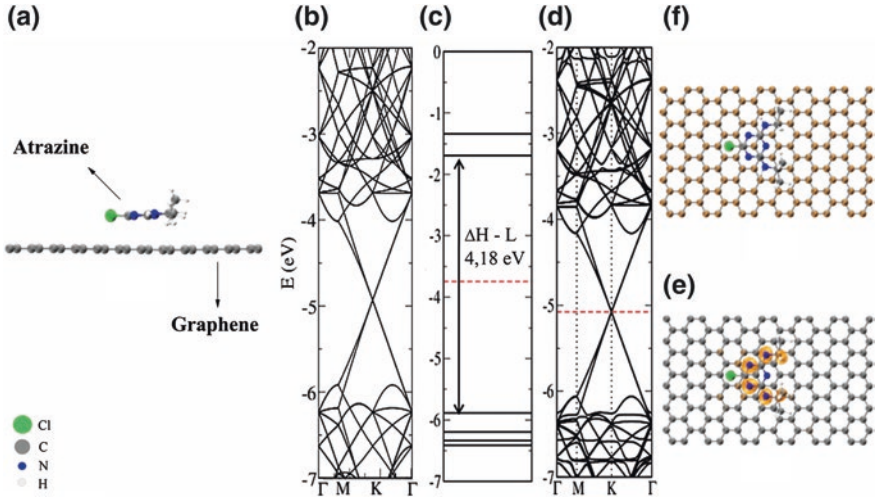

Fig. 5.4 Results for the most stable system found for the adsorption of atrazine on graphene. **a** Geometric structure of the interacting system. Electronic levels for isolated graphene (**b**) Atrazine (**c**); Atrazine adsorbed on graphene (**d**). Electronic charge density plots for **e** valence levels from −6.4 to −6.3 eV and **f** conduction levels from −4.9 to −4.8 eV. The horizontal *dashed red lines* indicate the Fermi energy

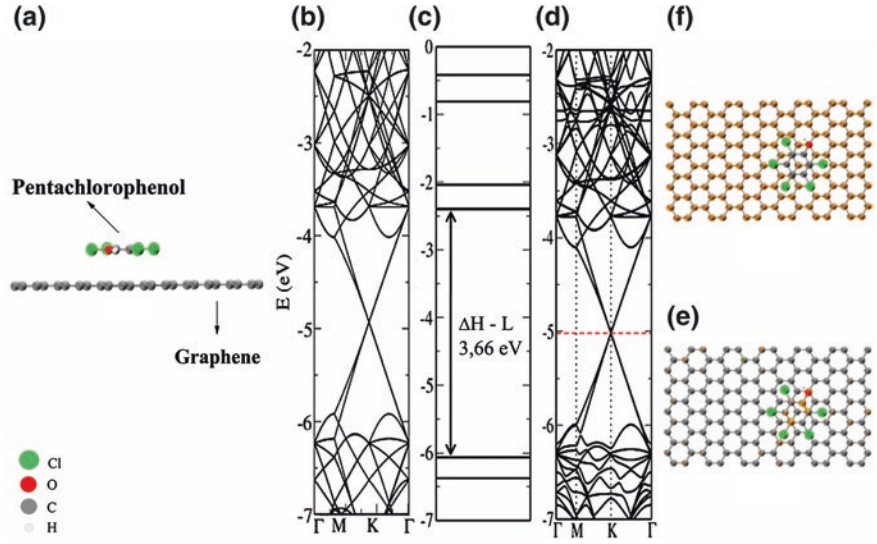

Fig. 5.5 Results for the most stable system found for the adsorption of Pentachlorophenol on graphene. **a** Geometric structure of the interacting system. Electronic levels for isolated graphene (**b**) PCP (**c**); PCP adsorbed on graphene (**d**). Electronic charge density plots for **e** valence levels from −6.3 to −6,2 eV and **f** conduction levels from −4.9 to −4.8 eV. The horizontal *dashed red lines* indicate the Fermi energy

the amount of sites for adsorption, therefore, reducing the binding energy between graphene and the molecules. On the other hand, the binding energy of the functionalized graphene with hydroxyl groups on the surface can be more effectively increased than that of epoxy group, because of enabling higher charge transfer. Furthermore, for adsorption on nanoribbons, all configurations showed an increase in binding energy when compared to a pristine graphene, indicating a strong contribution of electrostatic interactions in those cases. Furthermore, it was observed that increasing the amount of functional groups on the surface of graphene makes it more reactive. However, if there are excessive functional groups on the surface of graphene, they can negatively contribute to the binding energy, weakening the $\pi-\pi$ interactions between graphene and the molecules.

5.5 Concluding Remarks

This chapter covered a wide range of experimental and theoretical adsorption of carbon nanomaterials as nanoadsorbents, which have been employed so far for removal of various organic and inorganic pollutants from the water and wastewater. The high efficiency, simplicity and ease in the scaling-up of adsorption processes using carbon nanomaterials make the adsorption technique attractive for removal and recovery of organic and inorganic compounds. Most of the studies reported in the literature have focused on the production of carbon nanomaterials from low cost resources compared with the performance of readily available commercial activated carbons. As proved, nanotechnology can play an important role in this context and, therefore, an emerging area of research is the development of new nanomaterials with high affinity, capacity and selectivity for adsorption.

Acknowledgments The authors acknowledge funding from Brazilian agencies CNPq and CAPES.

References

1. Gupta VK, Saleh TA (2013) Sorption of pollutants by porous carbon, carbon nanotubes and fullerene—an overview. Environ Sci Pollut Res 20:2828–2843
2. Kroto HW, Heath JR, Obrien SC, Curl RF, Smalley RE (1985) C_{60}: Buckminsterfullerene. Nature 318:162–163
3. Pan B, Lin D, Mashayekhi H, Xing B (2008) Adsorption and hysteresis of bisphenol A and 17r-ethinyl estradiol on carbon nanomaterials. Environ Sci Technol 42:5480–5485
4. Yang Y, Nakada N, Tanaka H (2013) Adsorption of fullerene nC60 on activated sludge: kinetics, equilibrium and influencing factors. Chem Eng J 225:365–371
5. Iijima S (1991) Helical microtubules of graphitic carbon. Nature 354:56–58
6. Iijima S, Ichihashi T (1993) Single-shell carbon nanotubes of 1-nm diameter. Nature 363:603–605
7. Bethune DS, Klang CH, De Vries MS et al (2003) Cobalt-catalysed growth of carbon nanotubes with single-atomic-layer walls. Nature 363:605–607

8. Machado FM, Bergmann CP, Fernandes THM et al (2011) Adsorption of Reactive Red M-2BE dye from water solutions by multi-walled carbon nanotubes and activated carbon. J Hazard Mater 192:1122–1131
9. Machado FM, Bergmann CP, Lima EC et al (2012) Adsorption of Reactive Blue 4 dye from water solutions by carbon nanotubes: experiment and theory. Phys Chem Chem Phys 14:11139–11153
10. Novoselov KS, Geim AK, Morozov SV et al (2004) Electric field effect in atomically thin carbon films. Science 306:666–669
11. Ramesha GK, Kumara AV, Muralidhara HB, Sampath S (2011) Graphene and graphene oxide as effective adsorbents toward anionic and cationic dyes. J Colloid Interface Sci 361:270–277
12. Chowdhury S, Balasubramanian R (2014) Recent advances in the use of graphene-family nanoadsorbents for removal of toxic pollutants from wastewater. Adv Colloid Interface Sci 204:35–56
13. Salam MA, Al-Zhrani G, Kosa SA (2014) Removal of heavy metallic ions from aqueous solution by multi-walled carbon nanotubes modified with 8-hydroxyquinoline: kinetic study. J Ind Eng Chem 20:572–580
14. Ren X, Li J, Tan X, Wang X (2013) Comparative study of graphene oxide, activated carbon and carbon nanotubes as adsorbents for copper decontamination. Dalton Trans 42:5266–5274
15. Lu CS, Chiu HS (2006) Adsorption of zinc(II) from water with purified carbon nanotubes. Chem Eng Sci 61:1138–1145
16. Li YH, Di Z, Ding J, Wu D, Luan Z, Zhu Y (2005) Adsorption thermodynamic, kinetic and desorption studies of Pb2+ on carbon nanotubes. Water Res 39:605–609
17. Schierz A, Zänker H (2009) Aqueous suspensions of carbon nanotubes: surface oxidation, colloidal stability and uranium sorption. Environ Pollut 157:1088–1094
18. Li YH, Wang S, Luan Z, Ding J, Xu C, Wu D (2003) Adsorption of cadmium(II) from aqueous solution by surface oxidized carbon nanotubos. Carbon 41:1057–1062
19. Rao GP, Lu C, Su F (2007) Sorption of divalent metallic ions from aqueous solution by carbon nanotubes: a review. Sep Purif Technol 58:224–231
20. Salam MA (2013) Removal of heavy metallic ions from aqueous solutions with multi-walled carbon nanotubes: kinetic and thermodynamic studies. Int J Environ Sci Technol 10:677–688
21. Lu C, Liu C (2006) Removal of nickel(II) from aqueous solution by carbon nanotubos. J Chem Technol Biotechnol 81:1932–1940
22. Bayazit ŞS, Inci I (2013) Adsorption of Pb(II) ions from aqueous solutions by carbon nanotubes oxidized different methods. J Ind Eng Chem 19:2064–2071
23. Kuo CY (2009) Water purification of removal aqueous copper(II) by as-grown and modified multi-walled carbon nanotubes. Desalination 249:781–785
24. Hu J, Chen C, Zhu X, Wang X (2009) Removal of chromium from aqueous solution by using oxidized multiwalled carbon nanotubes. J Hazard Mater 162:1542–1550
25. Pillaya K, Cukrowska EM, Coville NJ (2009) Multi-walled carbon nanotubes as adsorbents for the removal of parts per billion levels of hexavalent chromium from aqueous solution. J Hazard Mater 166:1067–1075
26. Leng Y, Guo W, Su S, Yi C, Xing L (2012) Removal of antimony(III) from aqueous solution by graphene as an adsorbent. Chem Eng J 211–212(15):406–411
27. Huang Z-H, Zheng X, Lv W, Wang M, Yang Q-H, Kang F (2011) Adsorption of lead(II) ions from aqueous solution on low-temperature exfoliated graphene nanosheets. Langmuir 27:7558–7562
28. Yang S, Li L, Peia Z (2014) Adsorption kinetics, isotherms and thermodynamics of Cr(III) on graphene oxide. Colloids Surf A 457:100–106
29. Wu W, Yang Y, Zhou H et al (2013) Highly efficient removal of Cu(II) from aqueous solution by using graphene oxide. Water Air Soil Pollut 224:1372–1375
30. Sitko R, Turek E, Zawisz B et al (2013) Adsorption of divalent metal ions from aqueous solutions using graphene oxide. Dalton Trans 42:5682–5689

31. Pan N, Deng J, Guan D, Jin Y, Xia C (2013) Adsorption characteristics of Th(IV) ions on reduced graphene oxide from aqueous solutions. Appl Surf Sci 287:478–483
32. Alencar WS, Lima EC, Royer B et al (2012) Application of aqai stalks as biosorbents for the removal of the dye Procion Blue MX-R from aqueous solution. Sep Sci Technol 47:513–526
33. Hessel C, Allegre C, Maisseu M, Charbit F, Moulin P (2007) Guidelines and legislation for dye house effluents. J Environ Manage 83:171–180
34. Cardoso NF, Lima EC, Royer B et al (2012) Comparison of Spirulina platensis microalgae and commercial activated carbon as adsorbents for the removal of Reactive Red 120 dye from aqueous effluents. J Hazard Mater 241–242:146–153
35. Carneiro PA, Umbuzeiro GA, Oliveira DP, Zanoni MVB (2010) Assessment of water contamination caused by a mutagenic textile effluent/dye house effluent bearing disperse dyes. J Hazard Mater 174(1–3):694–699
36. Prola LDT, Acayanka E, Lima EC et al (2013) Comparison of Jatropha curcas shells in natural form and treated by non-thermal plasma as biosorbents for removal of Reactive Red 120 textile dye from aqueous solution. Ind Crop Prod 46:328–340
37. Li Y, Du Q, Liu T et al (2013) Comparative study of methylene blue dye adsorption onto activated carbon, graphene oxide, and carbon nanotubes. Chem Eng Res Des 91:361–368
38. Chatterjee S, Chatterjee T, Lim SR, Woo SH (2011) Effect of the addition mode of carbon nanotubes for the production of chitosan hydrogel core–shell beads on adsorption of Congo red from aqueous solution. Bioresour Technol 102:4402–4409
39. Mishra AK, Arockiadoss T, Ramaprabhu S (2010) Study of removal of azo dye by functionalized multi walled carbon nanotubes. Chem Eng J 162:1026–1034
40. Wang S, Ng CW, Wang W, Li Q, Hao Z (2012) Synergistic and competitive adsorption of organic dyes on multiwalled carbon nanotubes. Chem Eng J 197:34–40
41. Kuo CY, Wu CH, Wuc JY (2008) Adsorption of direct dyes from aqueous solutions by carbon nanotubes: determination of equilibrium, kinetics and thermodynamics parameters. J Colloid Interface Sci 327:308–315
42. Yao Y, Xu F, Chen M, Xu Z, Zhu Z (2010) Adsorption behavior of methylene blue on carbon nanotubes. Bioresour Technol 101:3040–3046
43. Wu CH (2007) Adsorption of reactive dye onto carbon nanotubes: equilibrium, kinetics and thermodynamics. J Hazard Mater 144:93–100
44. Prola LDT, Machado FM, Bergmann CP et al (2013) Adsorption of Direct Blue 53 dye from aqueous solutions by multi-walled carbon nanotubes and activated carbon. J Environ Manage 130:166–175
45. Zhao D, Zhang W, Chen C, Wang X (2013) Adsorption of methyl orange dye onto multiwalled carbon nanotubes. Procedia Environ Sci 18:890–895
46. Wang S, Ng CW, Wang W, Li Q, Li L (2012) A comparative study on the adsorption of acid and reactive dyes on multiwall carbon nanotubes in single and binary dye systems. J Chem Eng Data 57:1563–1569
47. Wu T, Cai C, Tan S, Li H, Liu J, Yang W (2011) Adsorption characteristics of acrylonitrile, p-toluenesulfonic acid, 1-naphthalenesulfonic acid and methyl blue on graphene in aqueous solutions. Chem Eng J 173:144–149
48. Yu J-G, Zhao X-H, Yang H et al (2014) Aqueous adsorption and removal of organic contaminants by carbon nanotubes. Sci Total Environ 482–483:241–251
49. Gebhardt W, Schröder HF (2007) Liquid chromatography-(tandem) mass spectrometry for the follow-up of the elimination of persistent pharmaceuticals during wastewater treatment applying biological wastewater treatment and advanced oxidation. J Chromatogr A 1160:34–43
50. Cho H-H, Huang H, Schwab K (2011) Effects of solution chemistry on the adsorption of ibuprofen and triclosan onto carbon nanotubes. Langmuir 27:12960–12967
51. Kim H, Hwang YS, Sharma VK (2014) Adsorption of antibiotics and iopromide onto single-walled and multi-walled carbon nanotubes. Chem Eng J 255:23–27
52. Wang Y, Yang S-T, Wang Y, Liu Y, Wang H (2012) Adsorption and desorption of doxorubicin on oxidized carbon nanotubes. Colloids Surf B 97:62–69

53. Joseph L, Zaib Q, Khan IA et al (2011) Removal of bisphenol A and 17alpha-ethinyl estradiol from landfill leachate using single-walled carbon nanotubes. Water Res 45:4056–4068
54. Xu J, Wang L, Zhu Y (2012) Decontamination of bisphenol A from aqueous solution by graphene adsorption. Langmuir 28:8418–8425
55. Zaib Q, Khan IA, Saleh NB, Flora JRV, Park Y-G, Yoon Y (2012) Removal of bisphenol A and 17β-estradiol by single-walled carbon nanotubes in aqueous solution: adsorption and molecular modeling. Water Air Soil Pollut 223:3281–3293
56. Zhang MH, Zhao QL, Bai X, Ye ZF (2010) Adsorption of organic pollutants from coking wastewater by activated coke. Colloids Surf A 362:140–146
57. Al-khalid T, El-naas MH (2012) Aerobic biodegradation of phenols: a comprehensive review. Crit Rev Env Sci Technol 42:1631–1690
58. Delval F, Crini G, Vebrel J (2006) Removal of organic pollutants from aqueous solutions by adsorbents prepared from an agroalimentary by-product. Bioresour Technol 97:2173–2181
59. Pei Z, Li L, Sun L et al (2013) Adsorption characteristics of 1,2,4-trichlorobenzene, 2,4,6-trichlorophenol, 2-naphthol and naphthalene on graphene and graphene oxide. Carbon 51:156–163
60. Smith EA, Oehme FW (1992) The biological activity of glyphosate to plants and animals: a literature review. Vet Hum Toxicol 34:531–543
61. Samsel A, Seneff S (2013) Glyphosate's suppression of cytochrome P450 enzymes and amino acid biosynthesis by the gut microbiome: pathways to modern diseases. Entropy 34:1416–1463
62. Pyrzynska K (2011) Carbon nanotubes as sorbents in the analysis of pesticides. Chemosphere 83:1407–1413
63. Deng J, Shao Y, Gao N et al (2012) Multiwalled carbon nanotubes as adsorbents for removal of herbicide diuron from aqueous solution. Chem Eng J 193–194:339–347
64. Maliyekkal SM, Sreeprasad TS, Krishnan D et al (2013) Graphene: a reusable substrate for unprecedented adsorption of pesticides. Small 9(2):273–283
65. Fakhri A (2013) Adsorption characteristics of graphene oxide as a solid adsorbent for aniline removal from aqueous solutions: kinetics, thermodynamics and mechanism studies. J Saudi Chem Soc. doi:10.1016/j.jscs.2013.10.002
66. Mkhoyan KA, Contryman AW, Silcox J et al (2009) Atomic and electronic structure of graphene-oxide. Nano Lett 9(3):1058–1063

Chapter 6
Molecules with Biological Interest Adsorbed on Carbon Nanostructures

Mariana Zancan Tonel, Vivian Machado de Menezes, Ivana Zanella and Solange Binotto Fagan

Abstract In the last decade, carbon nanostructures have been exhaustively studied mainly associated with their application in biosensors and drug delivery systems. In this context, the present chapter introduces several studies combining amino acids and pharmaceutical drugs with carbon nanostructures such as graphene, carbon nanotubes and fullerene. More specifically, the biomolecules under focus are the amino acid cysteine and the pharmaceutical drugs nimesulide, meloxicam and zidovudine. These molecules can be considered models for different chemical interactions or adsorptions with carbon nanostructures. The adsorptions analysed suggest possible applications such as biosensors or drug delivery depending on the use of particular pristine or functionalised carbon nanomaterials.

Keywords Carbon nanomaterials · Biosensors · Drug delivery · Amino acids · Pharmaceutical drugs

Abbreviations

0D	Zero dimensional
1D	One dimensional

M.Z. Tonel · I. Zanella · S.B. Fagan (✉)
Área de Ciências Tecnológicas, Centro Universitário Franciscano, Santa Maria, RS 97010032, Brazil
e-mail: solange.fagan@gmail.com

M.Z. Tonel
e-mail: marianaztonel@gmail.com

I. Zanella
e-mail: ivanazanella@gmail.com

V.M. de Menezes
Universidade Federal da Fronteira Sul, Laranjeiras do Sul, PR 85301970, Brazil
e-mail: demenezes.vivian@gmail.com

C.P. Bergmann and F.M. Machado (eds.), *Carbon Nanomaterials as Adsorbents for Environmental and Biological Applications*, Carbon Nanostructures,
DOI 10.1007/978-3-319-18875-1_6

2D	Two dimensional
AIDS	Acquired immune deficiency syndrome
AZT	Zidovudine or azidothydamine
BSSE	Basis set superposition error
CN	Carbon nanomaterials
CNT	Carbon nanotubes
COX	Cyclooxygenase
DFT	Density functional theory
DNA	Deoxyribonucleic acid
DOX	Doxorubicin
NSAID	Nonsteroidal anti-inflammatory drugs
SIESTA	Spanish initiative for the electronic simulations of thousands of atoms
SWCNT	Single-walled carbon nanotubes

6.1 Introduction

Nanoscience and nanotechnology have attracted great interest from the scientific community due to the new technological possibilities offered by the properties of nanomaterials. A wide variety of applications has been suggested, in fields ranging from electronics [1] to materials science [2]. There has also been a significant amount of research conducted with a biological focus, associated with the search for new methods of disease detection and therapy [3, 4], as well as monitoring via sensors [5, 6].

The most promising materials developed for use in nanotechnology are carbon nanomaterials (CNs). Among these, graphene, carbon nanotubes (CNTs) and fullerenes are considered 2D, 1D and 0D materials, respectively, based on their electronic confinement (Fig. 6.1a–c). These three nanomaterials have attracted considerable interest due to their structural and electronic characteristics [7], in particular those offering the possibility of performing biofunctionalisations [8] via applications such as drug carriers and biological sensors.

The molecules of biological interest evaluated in the present chapter include amino acids such as cysteine, and pharmaceutical drugs such as nimesulide, zidovudine (AZT) and meloxicam. These molecules can be considered models for different chemical interactions or adsorptions with CNs based on their functional groups, with possible applications including biosensors and drug delivery systems.

6.2 Biomolecule Adsorption on Carbon Nanostructures

Pharmaceutical drugs and amino acids adsorbed on CNs such as fullerenes [9], CNTs [10] and graphene [11] can be used for applications including selective drug delivery systems and the detection of biological constituents.

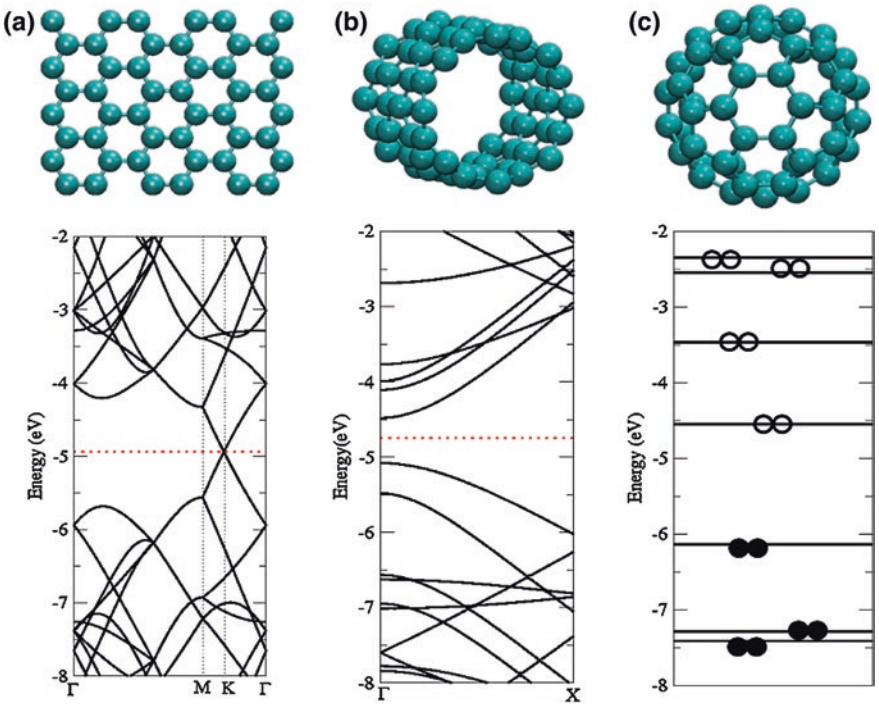

Fig. 6.1 Carbon nanostructures: **a** graphene, **b** CNTs and **c** fullerene, with their respective electronic levels. The horizontal *dashed red lines* correspond to the Fermi energy

Graphene was first isolated by Novoselov and collaborators via the mechanical exfoliation of graphite [12]. This material is defined as one carbon layer with the atoms arranged in a honeycomb lattice [12]. A 2D nanomaterial in which the electrons are free to move in two directions and confined in one, graphene is the thinnest material known (a thickness of one atom) and one of the strongest ever measured. Graphene also exhibits interesting features that offer possibilities for various applications, including as a charge carrier due to its high electronic mobility and zero effective mass [13]. Further promising applications in biomedicine include drug delivery, cancer therapy, cancer cell detection and biological imaging [14]. Recent research shows that graphene can be used as a substrate with which to connect biomolecules and biological cells [15]. However, for the effective use of carbon nanostructures (including graphene) in biological environments, their solubility and selectivity with biomolecules must be improved. To this end, several studies have focused on the modification and functionalisation of the surface of carbon nanostructures in an attempt to improve their biocompatibility. Such functionalisations can be carried out via topological defects, adsorption of functional groups, or deoxyribonucleic acid (DNA) and protein attachment on the graphene surface [16]. Figure 6.2 illustrates the exponential increase in the number of publications associated with at least one of the subjects ‘graphene’, ‘biosensor’

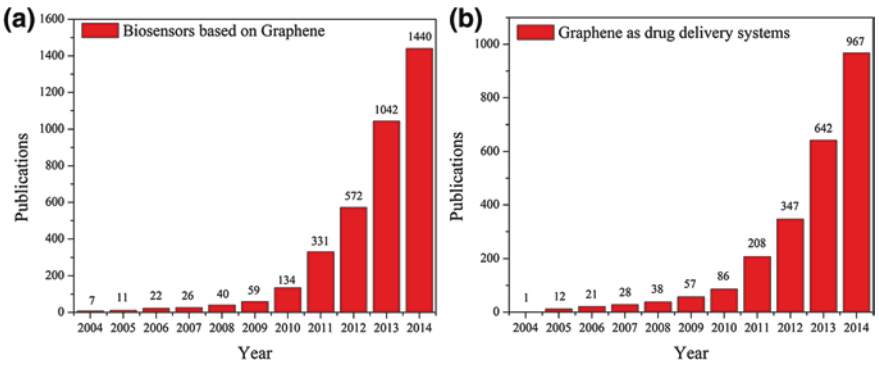

Fig. 6.2 Articles published since 2004 regarding the application of graphene in **a** biosensors and **b** drug delivery systems (www.sciencedirect.com, last accessed 30th October 2014)

and 'drug delivery' that has taken place during the last decade (2004–2014), indicating the relevance of the study of biomolecules interacting with this particular nanomaterial.

A CNT was described for the first time in 1991 by Iijima [17] and is defined, theoretically, as a graphene sheet rolled up into a cylinder. Considered one of the strongest, most durable and flexible materials studied for mechanical applications [18, 19], CNTs can exhibit a variety of different electronic properties, being metallic and semiconducting, depending on their chirality and diameter. A CNT is considered a 1D system because its length is larger than its diameter, creating a quantum confinement in two directions. CNTs have similar dimensions to those of biological molecules, a feature which has prompted their development for use in biosensors, drug delivery and biomechanical devices [20, 21]. Although the CNT was described ten years before graphene [12, 17], the increasing trend regarding the number of scientific publications focussing on biological applications is the same for the two materials, as can be seen in Fig. 6.3.

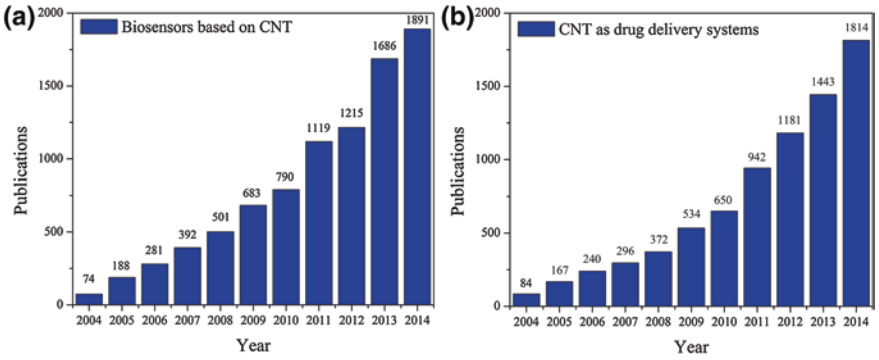

Fig. 6.3 Articles published since 2004 regarding the application of CNTs in **a** biosensors and **b** drug delivery systems (www.sciencedirect.com, last accessed 30th October 2014)

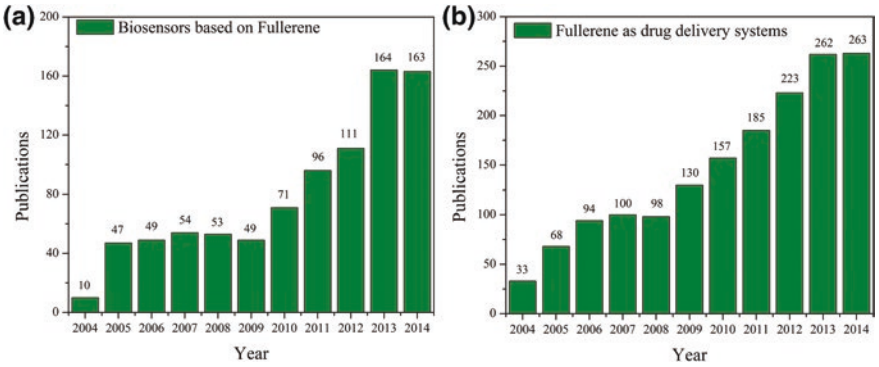

Fig. 6.4 Articles published since 2004 regarding the application of fullerene in **a** biosensors and **b** drug delivery systems (www.sciencedirect.com, last accessed 30th October 2014)

Fullerenes are a class of spherical molecules formed by only carbon atoms and can be found in a range of sizes, including 20, 60, 70, 100, 180, 240 and 540 atoms [22]. The C_{60} molecule, which is considered the most abundant fullerene, contains 60 carbon atoms in a 0D structure, with electrons confined in all directions. Several biological properties of these materials and their derivatives have been studied in fields ranging from photodynamic therapy, neuroprotective-, antimicrobial- and antiviral activity, through to other interactions with multiple biological targets [23]. Although fullerenes were discovered in 1985 and have a wide range of potential biological applications, the number of scientific publications examining such molecules is ten times smaller (Fig. 6.4) than that for graphene (Fig. 6.2) and CNT (Fig. 6.3) in terms of their application in biosensors and drug delivery.

The following sections will discuss some of the issues involving CNs and the adsorption of amino acids (Sect. 6.3) and pharmaceutical drugs (Sect. 6.4). The presented data were selected from both the literature and original experiments. For the latter, ab initio simulations were performed via density functional theory (DFT) using the SIESTA code (Spanish Initiative for the Electronic Simulations of Thousands of Atoms) [24]. The methodology used in the simulations is in agreement with other studies carried out by the present authors, such as Menezes and coworkers [25].

6.3 Amino Acids Adsorbed on Carbon Nanostructures

Among the various molecules of biological interest, it is essential to highlight amino acids. These molecules are vital to the human body since they are constituents of proteins, enzymes, transport molecules, cell membranes, peptides, hormones and signalling molecules of the nervous system, among others [26–28]. Organic molecules containing amine ($–NH_2$) and carboxyl (–COOH) groups, amino acids are amphoteric substances, which means they can behave as either

acid or base depending on the environment [26]. Amino acids are also classified as essential or non-essential, with the human body unable to produce the latter.

Cysteine (HS–CH_2–CH–(NH_2)–COOH) is an essential amino acid that contains thiol (–SH), amine (–NH_2) and carboxyl (–COOH) chemical groups. This molecule is present in proteins and plays a key role in molecular biology, biochemistry and medicine, especially in the interaction of biomolecules with the inorganic environment or in association with metallic ions. Although the cysteine molecule has a number of derivative forms, here we will discuss only the most abundant enantiomer: L-cysteine [26].

CNs can be associated with amino acids through the latter's functional groups acting as coupling agents. From an experimental point of view, several alternatives have been evaluated aimed at connecting amino acids to CNs [27, 28].

Electrochemical sensors that are highly sensitive to L-cysteine have been developed using graphene–Au nanoparticles that combine the exceptional conductivity of graphene and the strong catalytic property of the Au nanomaterial [29]. Graphene oxide, a derivative of functionalised graphene [30], has also been analysed for use as an alternative electrochemical sensor, via fluorescence resonance for the detection of molecules including cysteine, DNA, proteins and metallic ions [31].

Similarly, Carneiro et al. [32] employed DFT to investigate the adsorption of the amino acid alanine on pristine and functionalised (5,5) single-walled carbon nanotubes (SWCNTs), showing that the interaction occurred via the amine group. For the pristine SWCNTs, the strongest bond was observed where all C atoms from the tubes exhibited sp^2-like hybridisation and remained a metallic system. In contrast, for functionalised SWCNTs with carboxyl groups, the properties of the resulting systems were independent of the alanine adsorption site [32].

Ganji evaluated, also via DFT, the interaction of the amino acids glycine, histidine, cysteine and phenylalanine with (10,0) SWCNTs, taking into account the ionic/non-ionic environment and the molecule position on the surface, revealing physical adsorption [33]. The same author also studied the influence of the inner and outer surface of (13,0) SWCNTs on glycine, histidine, cysteine and phenylalanine adsorption, finding that these amino acids can be encapsulated inside the tube and form a more stable complex than those adsorbed on the outer surface [34]. Additional work has shown that the thiol (–SH) group of cysteine can improve the interaction of this particular amino acid with metallic systems due to its ability to act as a chemical sensor for metallic ions, especially Au and Pt [35].

DFT simulations of cysteine adsorption onto pristine and Au-functionalised graphene surfaces have indicated that both nanosystems have some chemosensor capacity, although the Au-doped graphene improved sensor ability largely than pristine graphene [36]. In the same way, DFT-based calculations of cysteine interaction with the surface of pristine and Pt-functionalised graphene have also demonstrated that their metallic functionalised surfaces are good candidates for use in the detection of biomolecules with a thiol group [37].

In order to contribute to the discussion surrounding cysteine interaction with carbon nanostructures, we here present a systematic study of the adsorption of this amino acid onto graphene (8,0) SWCNTs and fullerene. The interaction of the

Table 6.1 Binding energies and electronic charge transfers found for the most stable configurations of the interactions between cysteine and CNs

Configuration	Binding energy (eV)	Electronic charge transfer (e^-)
Cys–SH–graphene	−0.24	−0.02
Cys–COOH–graphene	−0.18	−0.04
Cys–NH_2–graphene	−0.19	+0.09
Cys–SH–graphene—vacancy	−0.29	+0.01
Cys–COOH–graphene—vacancy	−0.09	−0.01
Cys–NH_2–graphene—vacancy	−0.23	+0.07
Cys–SH–SWCNT	−0.22	+0.05
Cys–COOH–SWCNT	−0.22	−0.03
Cys–NH_2–SWCNT	−0.20	+0.06
Cys–SH–C_{60}	−0.12	−0.01
Cys–COOH–C_{60}	−0.11	−0.05
Cys–NH_2–C_{60}	−0.11	+0.05

Negative values for binding energy represent an exothermic interaction. Charge transfer positive: from the CNs to the cysteine molecule

cysteine molecule on the CN surface was performed using the amine, carboxyl and thiol groups in different atomic arrangements. The results for the most stable configurations of these analyses are shown in Table 6.1, which displays the values of the binding energies and electronic charge transfer.

Binding energies were calculated using the basis set superposition error (BSSE) [38]. This method employs 'ghost' atoms in Eq. 6.1 as follows:

$$\text{Binding energy} = E_{\text{T}}(\text{CN} + X) - E_{\text{T}}\left(\text{CN} + X_{\text{ghost}}\right) - E_{\text{T}}\left(\text{CN}_{\text{ghost}} + X\right) \quad (6.1)$$

where X corresponds to the amino acid or pharmaceutical drug, and CN to the carbon nanostructure. E_{T} (CN + X) is the total energy of nanostructure interaction with the adsorbed molecule. The 'ghost' CN/X corresponds to the additional basis wave functions centred at the position of the original CN/X, but without any atomic potential.

The association of the tested 2D, 1D and 0D nanomaterials with cysteine was found to be weak, as can be seen in Table 6.1, with the binding energies for all the interacting systems indicating physical adsorption (all values below −0.24 eV). These interactions occurred without any changes to the amino acid molecular structure, a phenomenon that is of great significance regarding the use of the nanomaterials as drug carriers. Additionally, depending on the desired application, the weakness of the interaction (physisorption) is itself interesting, because in such cases the system is not connected and can therefore be easily 'turned off', i.e. used as a reversible biosensor.

Figure 6.5 displays the results for the most stable system of cysteine adsorption onto graphene. Analysing the electronic band structure of this adsorption (Fig. 6.5d), one can observe that there are no significant changes in comparison to that of pristine graphene (Fig. 6.5b). This result corroborates the weak interaction found via the binding energy calculation (−0.24 eV), where the observed changes

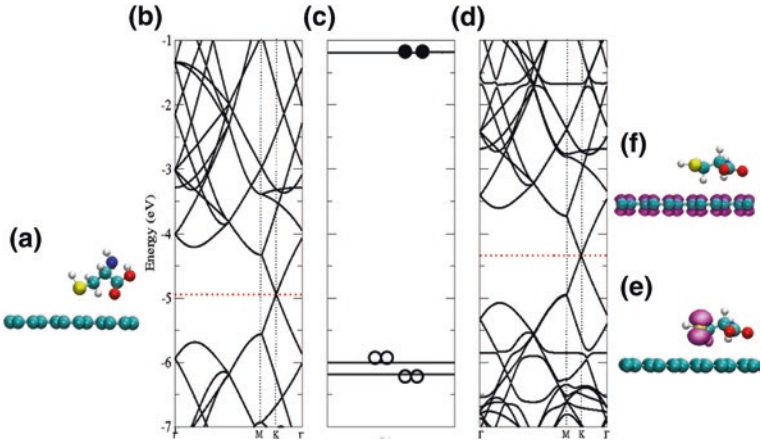

Fig. 6.5 Results for the most stable system found for the adsorption of cysteine on graphene. **a** Geometric structure of the interacting system. Electronic levels for isolated graphene **b** and cysteine **c**; cysteine adsorbed on graphene **d**. Electronic charge density plots for **e** valence levels from −6.0 to −5.5 eV and **f** conduction levels from −3.10 to −3.09 eV. The horizontal *dashed red lines* indicate the Fermi energy

in band structure are associated with the appearance of flat levels of cysteine electronic charge density. Examination of the electronic charge density plots reveals a concentration of charge on the graphene surface in the conduction band (Fig. 6.5f), with the charge in the valence band concentrated on the –SH group of cysteine (Fig. 6.5e), the most reactive chemical group in the molecule.

Comparing the recorded binding energy values for pristine and defective graphene, it can be seen that the vacancy on the graphene surface increases the reactivity of the system, changing the value of binding energy for the –SH group from −0.24 to −0.29 eV. In addition, a comparison of the three systems reveals that graphene has the highest binding energy, followed by CNT and fullerene. Menezes et al. [25] also found the same result, concluding that this particular pattern reflects the number of CN atoms close to the adsorbed molecule; as graphene is the most planar structure it has more atoms able to interact with the molecule, thus increasing adsorption.

Figure 6.6 displays the results for one of the most stable systems found regarding the adsorption of cysteine on the tested SWCNTs, in this case via –SH group interaction with the surface.

Analysing the electronic band structure of cysteine adsorbed on CNTs (Fig. 6.6d), a similar result to that of the interaction with graphene is found, with no significant changes in comparison to the pristine material (Fig. 6.6b). Since only a weak interaction was observed in terms of the binding energy (−0.22 eV), the appearance of non-interacting levels from the molecule when adsorbed on the nanotube surface could be expected. Once more, the charge was concentrated on the –SH group of cysteine, and in the valence band for the CNTs (Fig. 6.6e).

Finally, Fig. 6.7 displays the results for the most stable system found for cysteine adsorption onto fullerene C_{60}, again for the –SH group.

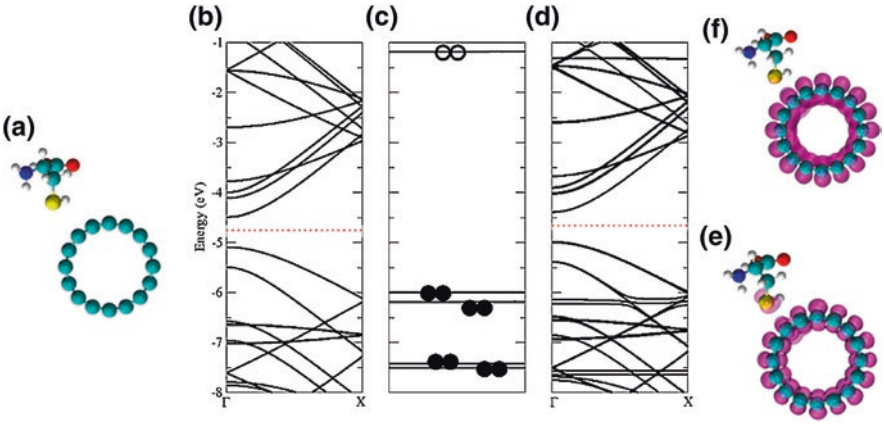

Fig. 6.6 Results for the most stable system found regarding the adsorption of cysteine on SWCNTs. **a** Geometric structure of the interacting system. Electronic levels for isolated (8,0) SWCNT **b** and cysteine **c**; cysteine adsorbed on the (8,0) SWCNT **d**. Electronic charge density plots for **e** valence levels from −4.99 to −4.90 eV and **f** conduction levels from −4.50 to −4.30 eV. The horizontal *dashed red lines* indicate the Fermi energy

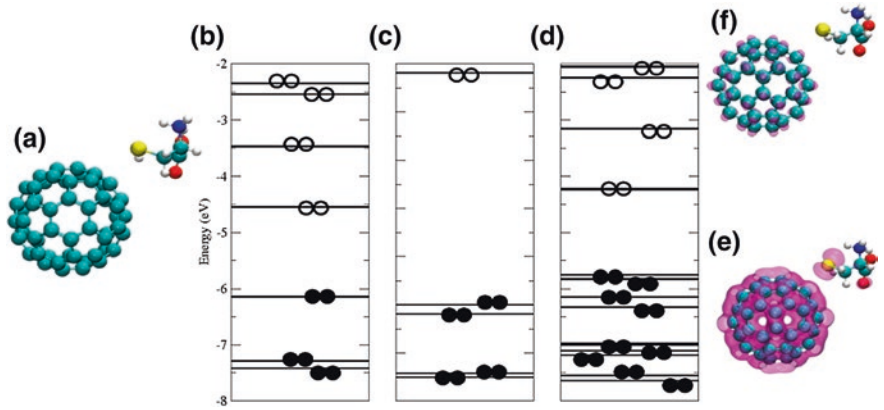

Fig. 6.7 Results for the most stable system found for the adsorption of cysteine on fullerene. **a** Geometric structure of the interacting system. Electronic levels for isolated fullerene molecule **b** and cysteine **c**; cysteine adsorbed on graphene **d**; electronic charge density plots for **e** HOMO and **f** LUMO. The horizontal *dashed red lines* indicate the Fermi energy

Figure 6.7d displays the electronic levels for the adsorbed molecule plus the fullerene, when both systems interact. The charge density plots illustrate the same behaviour as that found for SWCNTs, with a concentration of charge on the fullerene surface for the conduction level, and in the fullerene and the –SH group for the valence level. As discussed earlier, a number of studies have investigated the

interaction of different amino acids with pristine and functionalised CNs, mainly aimed at the development of biosensor applications [29, 31–37]. From a theoretical point of view, the binding energies and electronic properties of the three functional groups of cysteine, when interacting with different pristine CNs (graphene, CNTs and fullerene), reflect physical adsorption. Functionalisation is an effective method with which to increase the interaction between the CN and the adsorbed molecules, especially for biosensor applications [31–37].

6.4 Drugs Adsorbed on Carbon Nanostructures

Among the countless pharmaceutical compounds currently available, here we choose to highlight non-steroidal anti-inflammatory drugs (NSAIDs), which have the ability to both control inflammation and hyperthermia and reduce pain [39]. One such NSAID is nimesulide, which although has analgesic and antipyretic properties, its use has been linked to side effects associated with gastrointestinal toxicity [40, 41]. Nimesulide differs from other anti-inflammatory drugs [42] in that its structure includes a sulfoanilide fraction with the acid group. Unlike other classic NSAIDs, it also exhibits high gastrotolerability and acts as preferential in the cyclooxygenase-2 (COX-2) path. One method developed with which to increase the availability of nimesulide [43] has been its combination with other agents, such as cyclodextrins [44] and CNs [45].

Meloxicam is an enolic acid derivative NSAID [46] developed for the treatment of rheumatoid arthritis and osteoarthritis [47]. However, its administration has been linked to dangerous diseases including organic and functional disorders of the cardiovascular system and gastrointestinal tract [48]. Combining this drug with nanovehicles can potentially reduce these side effects.

Zidovudine or azidothymidine (AZT) is used as an antiviral drug in the treatment of Acquired Immune Deficiency Syndrome (AIDS) and infections involving *Pneumocystis carinii*. Indeed, AZT was one of the first drugs approved for AIDS treatment [49]. The structural and electronic properties of the interaction of AZT with SWCNTs and fullerenes were investigated, via ab initio calculations, by Vendrame and co-workers [50]. These authors found that the AZT molecules interact with the CN in a physisorption regime involving no changes to their electronic and structural properties, a phenomenon now considered an essential characteristic of successful drug delivery systems. The current section thus focuses on the interactions of CNs, such as graphene, CNTs and fullerenes, with anti-inflammatories and pharmaceutical compounds. Here we demonstrate that these nanostructures are sensitive to the presence of some molecules, and thus can be employed for use as pharmaceutical drug carriers. In this case the adsorbed molecules under study were nimesulide, meloxicam and AZT. Table 6.2 displays the results for the most stable configurations. Binding energy was calculated using the same equation as in Sect. 6.3 (Eq. 6.1).

As Table 6.2 reveals, the binding energy values associated with the adsorption of nimesulide, meloxicam and AZT onto the tested 0D, 1D and 2D CNs were all

Table 6.2 Binding energy and electronic charge transfer values found for the most stable configurations of nimesulide, meloxicam and AZT interaction with CN

Configuration	Binding energy (eV)	Electronic charge transfer (e^-)
Nimesulide—graphene	−0.57	+0.06
Nimesulide—SWCNT	−0.32	+0.07
Nimesulide—C_{60}	−0.32	+0.01
Meloxican—graphene	−0.36	+0.08
Meloxicam—SWCNT	−0.50	+0.07
Meloxicam—C_{60}	−0.29	+0.018
AZT—graphene	−0.62	+0.108
AZT—SWCNT	−0.44	+0.06
AZT—C_{60}	−0.32	−0.06

Negative values of binding energy represent an exothermic interaction. Charge transfer positive: from the CN to the pharmaceutical drug

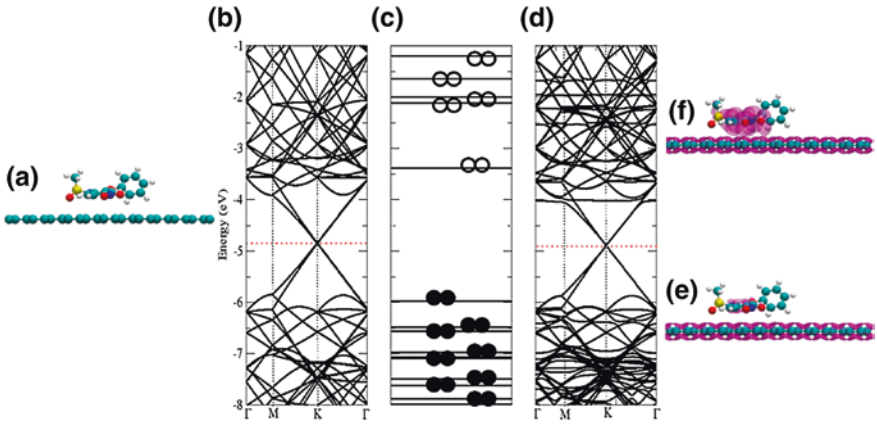

Fig. 6.8 **a** Geometric structure of nimesulide interaction with graphene. Electronic levels for **b** isolated graphene, **c** isolated nimesulide and **d** nimesulide interaction with graphene. Electronic charge density plots for **e** valence levels from −6.13 to −6.11 eV and **f** conduction levels from −4.03 to −4.01 eV. The horizontal *dashed red lines* represent the Fermi energy

low, indicating physical adsorption. As the electronic properties of their interactions with the CNs were similar, here we will discuss the obtained results for only one of the three selected pharmaceutical drugs (nimesulide).

Figure 6.8 displays the data for nimesulide adsorption onto a graphene surface. The electronic band structure of the nimesulide molecule (Fig. 6.8d) exhibits no significant changes in comparison to that of pristine graphene (Fig. 6.8b). This observation is due to the weak interaction of the adsorption (−0.57 eV), with flat levels of molecule charge noted mainly close to the conduction band in Fig. 6.8d. Analysis of the electronic charge density plots reveals a concentration of charge on the graphene surface in the valence band (Fig. 6.8e); in contrast, charge in the conduction band is concentrated on both graphene and nimesulide (Fig. 6.8f).

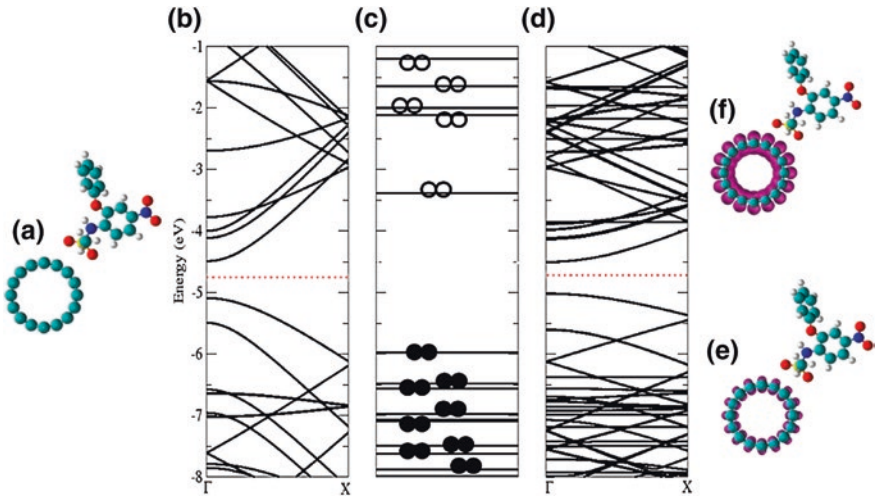

Fig. 6.9 **a** Geometric structure of nimesulide interaction with SWCNT. Electronic levels for **b** isolated nanotube, **c** isolated nimesulide and **d** nimesulide interaction with nanotube. Electronic charge density plots for **e** valence levels from −5.02 to −5.00 eV and **f** conduction levels from −4.60 to −4.40 eV

Figure 6.9 displays the obtained data for nimesulide adsorption onto a SWCNT surface. Analysis of the electronic band structure of the interacting systems (Fig. 6.9d) reveals a similar result to that found for the interaction with graphene, with no significant changes in comparison to pristine SWCNT (Fig. 6.9b). Considering the weak binding energy value shown in Table 6.2 (−0.32 eV), the appearance of flat levels of molecule electronic charge density during its adsorption on the nanotube surface was expected. This phenomenon can be observed in Fig. 6.9d.

In summary, no significant changes were observed in the band structures during nimesulide molecule adsorption on the SWCNT, indicating a physical process. Analysis of the electronic charge plots reveals that in both situations, i.e. for both valence (Fig. 6.9e) and conduction (Fig. 6.9f) bands, the charges are concentrated on the SWCNT surface.

Figure 6.10d shows the electronic levels for the nimesulide molecule plus the fullerene when the two systems interact, where these levels are a mix of those of isolated fullerene (Fig. 6.10b) and isolated nimesulide (Fig. 6.10c). The charge density plots reveal a concentration of charge in the nimesulide in the valence level (Fig. 6.10e) and in the fullerene in the conduction level (Fig. 6.10f).

Several experimental studies have been performed aimed at the development of graphene for use in biomedical applications [50–55]. These studies have revealed graphene to be efficient for both drug delivery, due to the aromatic π–π bonds found on its surface [51, 52], and photodynamic therapy, due to its high absorption in the infrared spectral range. A number of in vivo experimental studies have also proven the effectiveness of graphene for use in cancer treatment [53, 54].

More recently, graphene has been employed for the controlled delivery of the drug doxorubicin (DOX) [55]. According to Zhang et al. [56], photothermal

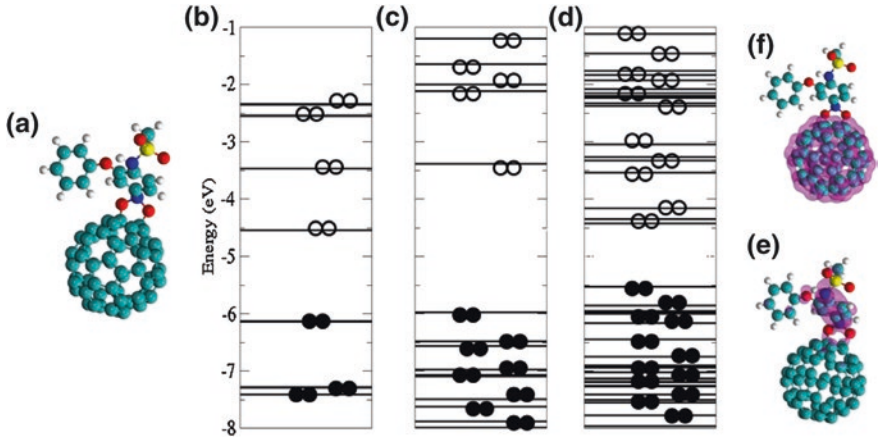

Fig. 6.10 **a** Geometric structure of nimesulide interaction with fullerene. Electronic levels for **b**) isolated fullerene, **c** isolated nimesulide and **d** nimesulide interaction with fullerene. Electronic charge density plots for **e** HOMO and **f** LUMO

therapy carried out using this combination resulted in both the complete annihilation of a tumour and a reduction in side effects.

Zanella and collaborators [45] evaluated the interaction of the nimesulide molecule with pristine and Si-doped capped SWCNTs, using first-principles calculations. The obtained results suggest that nimesulide interaction with capped nanotubes occurs in a physisorption regime and is much more intense when capped with a Si atom [45].

Analysis of Table 6.2 reveals that the use of graphene resulted in the highest binding energies for most of the studied pharmaceutical drugs. Similar results were found by Menezes et al. [25] regarding the interaction of carbon nanostructures (graphene, SWCNTs and fullerene) with vitamins. This behaviour is likely due the planarity of graphene, which increases the number of atoms near the nanostructure surface. In contrast, fullerene's greater curvature increases the distance between atoms, decreasing binding energy values with respect to those of SWCNTs. The results displayed in Table 6.2 demonstrate that CNTs, which are characterised by an intermediate curvature level, are generally associated with intermediate binding energies. The same pattern can be seen in Table 6.1 for the interaction of CN and cysteine.

In summary, the adsorption of molecules of biological interest, such as amino acids and pharmaceutical drugs, on pristine CNs is mediated through a physisorption regime. The presented results reveal only insignificant changes to the original geometric structures of the molecules take place after interaction on the CN, with the former thus retaining their initial chemical properties. The physisorption regimes of the systems (CN+ molecules of biological interest) may be relevant for drug delivery purposes due to the possibility of detaching the molecules from the nanostructure surface. Experiments examining the development of CNs for biosensor system applications have indicated the necessity of nanostructure functionalisation through the use of defects, carboxylation, oxidation or metallic attachment [27, 37].

References

1. Kim KS, Zhao Y, Jang H et al (2009) Large-scale pattern growth of graphene films for stretchable transparent electrodes. Nature 457:706–710
2. Singh V, Joung D, Zhai LS, Khondaker SI, Seal S (2011) Graphene based materials: past, present and future. Prog Mater Sci 56:1178–1271
3. Liu WT, Bien MY, Chuang KJ et al (2014) Physicochemical and biological characterization of single-walled and double-walled carbon nanotubes in biological media. J Hazard Mater 280:216–225
4. Venkatesan BM, Bashir R (2011) Nanopore sensors for nucleic acid analysis. Nat Nanotechnol 6:615–624
5. Li W, Wu P, Zhang H, Cai C (2012) Signal amplification of graphene oxide combining with restriction endonuclease for site-specific determination of DNA methylation and assay of methyltransferase activity. Anal Chem 84:7583–7590
6. Pumera M (2011) Graphene in biosensing. Mater Today 14:308–315
7. Terrones M, Botelllo-Méndez AR, Campos-Delgado J (2010) Graphene and graphite nanoribbons: morphology, properties, synthesis, defects and applications. Nano Today 5:351–372
8. Wang Y, Li Z, Wang J, Li J, Lin Y (2011) Graphene and graphene oxide: biofunctionalization and applications in biotechnology. Trends Biotechnol 29:205–212
9. Partha R, Conyers JL (2009) Biomedical applications of functionalized fullerene-based nanomaterials. Int J Nanomed 4:261–275
10. Fei S, Chen J, Yao S, Deng G, He D, Kuang Y (2005) Electrochemical behavior of L-cysteine and its detection at carbon nanotube electrode modified with platinum. Anal Biochem 339:29–35
11. Yang X, Wang Y, Huang X et al (2011) Multi-functionalized graphene oxide based anticancer drug-carrier with dual-targeting function and pH-sensitivity. J Mater Chem 21:3448–3454
12. Novoselov KS, Geim AK, Morozov SV et al (2004) Electric field effect in atomically thin carbon films. Science 306:666–669
13. Geim AK (2009) Graphene: status and prospects. Science 324:1530–1534
14. Feng L, Chen Y, Ren J, Qu XA (2011) A graphene functionalized electrochemical aptasensor for selective label-free detection of cancer cells. Biomaterials 32:2930–2937
15. Shen H, Zhang L, Liu M, Zhang Z (2012) Biomedical applications of graphene. theranostics 2:283–294
16. Compton OC, Nguyen ST (2010) Graphene oxide, highly reduced graphene oxide, and graphene: versatile building blocks for carbon-based materials. Small 6:711–723
17. Iijima S (1991) Helical microtubules of graphitic carbon. Nature 354:56–58
18. Kam NW, O'Connell M, Wisdom JA, Dai H (2005) Carbon nanotubes as multifunctional biological transporters and near-infrared agents for selective cancer cell destruction. Proc Natl Acad Sci USA 102:11600–11605
19. Wong SS, Joselevich E, Woolley AT, Cheung CL, Lieber CM (1998) Covalently functionalized nanotubes as nanometezised probes in chemistry and biology. Nature 394:52–55
20. Li X, Peng Y, Qu X (2006) Carbon nanotubes selective destabilization of duplex and triplex DNA and inducing B-A transition in solution. Nucleic Acids Res 34:3670–3676
21. Li X, Peng Y, Ren J, Qu X (2006) Carboxyl-modified single-walled carbon nanotubes selectively induce human telomerici-motif formation. Proc Natl Acad Sci USA 103:19658
22. Kroto HW (1987) The stability of the fullerenes C-24, C-28, C-32, C-36, C-50, C-60 And C-70. Nature 329:529–531
23. Jensen AW, Wilson SR, Schuster DI (1996) Biological applications of fullerenes. Bioorg Med Chem 4:767–779
24. Soler JM, Artacho E, Gale JD et al (2002) The SIESTA method for ab-initio order-N materials simulation. J Phys: Condens Matter 14:2745–2779
25. de Menezes VM, Michelon E, Rossato J, Zanella I, Fagan SB (2012) Carbon nanostructures interacting with vitamins A, B3 and C: *Ab initio* simulations. J Biomed Nanotechnol 8:1–5

26. Moore S, Stein WH, Fruton JS (1946) Chemical reactions of mustard gas and related compounds. The reaction of mustard gas with carboxyl groups and with the amino groups of amino acids and peptides. J Org Chem 11:675–680
27. Wu W, Jiang W, Zhang W, Lin D, Yang K (2013) Influence of functional groups on desorption of organic compounds from carbon nanotubes into water: insight into desorption hysteresis. Environ Sci Technol 47:8373–8382
28. Guo Y, Lu X, Weng J, Leng Y (2013) Density functional theory study of the interaction of arginine-glycine-aspartic acid with graphene, defective graphene, and graphene oxide. J Phys Chem C 117:5708–5717
29. Xu F, Yang D, Gao Y, Li H (2014) Electrochemical sensing platform for L-CySH based on nearly uniform Au nanoparticles decorated graphene nanosheets. Mater Sci Eng, C 38:292–298
30. Lee DW, Santos LDL, Seo JW et al (2010) Quantum confinement-induced tunable exciton states in graphene oxide. J Phys Chem B 114:5723–5728
31. Gao L, Lian C, Zhou Y et al (2014) Graphene oxide-DNA based sensors. Biosens Bioelectron 60:22–29
32. Carneiro MA, Venezuela P, Fagan SB (2008) First principles calculations of alanine radicals adsorbed on pristine and functionalized carbon nanotubes. J Phys Chem C 112:14812–14815
33. Ganji MD (2009) Density functional theory based treatment of amino acids adsorption on single-walled carbon nanotubes. Diamond Relat Mater 18:662–668
34. Ganji MD (2010) Calculations of encapsulation of amino acids inside the (13,0) single-walled carbon nanotube. Fullerenes, Nanotubes, Carbon Nanostruct 18:24–36
35. Ritchie SMC, Kissick KE, Bachas LG, Sikdar SK, Parikh C, Bhattacharyya D (2001) Polycysteine and other polyamino acid functionalized microfiltration membranes for heavy metal capture. Environ Sci Technol 35:3252–3538
36. Zhang Z, Jia H, Ma F, Han P, Liu X, Xu B (2011) First principle study of cysteine molecule on intrinsic and Au-doped graphene surface as a chemosensor device. J Mol Model 17:649–655
37. Ma F, Zhang Z, Jia H, Liu X, Hao Y, Xu B (2010) Adsorption of cysteine molecule on intrinsic and Pt-doped graphene: a first-principle study. J Mol Struct THEOCHEM 955:134–139
38. Boys SF, Bernardi F (1976) The calculation of small molecular interactions by the differences of separate total energies. Some procedures with reduced errors. Mol Phys 19:553–566
39. Borges M, Marini Filho R, Laposy CB et al (2013) Nonsteroidal anti-inflammatory therapy. Changes on renal function of healthy dogs. Acta Cir Bras 28:842–847
40. Barrier CH, Hirschowitz BI (1989) Current controversies in rheumatology. Controversies and management of non-steroidal anti-inflammatory drug induced side effects on upper gastrointestinal tract. Arthritis Rheum 32:926–929
41. Bjarnason I, Williams P, Smethrust P et al (1993) Side effects of nonsteroidal anti-inflammatory drugs on the small and large intestine in humans. Gastroenterology 104:1832–1847
42. Engelhardt G, Bögel R, Schnitzler C, Utzmann R (1996) Meloxican: influence on arachidonic acid metabolism: part II. In vivo findings. Biochem Pharmacol 51:29–38
43. Davis N, Brogden RN (1994) Nimesulide: an update of its pharmacodynamic and pharmacokinetic properties and its therapeutic efficacy. Drugs 48:431–454
44. Vavia PR, Adhage NA (1999) Inclusion complexation of nimesulide with beta-cyclodextrins. Drug Dev Ind Pharm 25(4):543–545
45. Zanella I, Fagan SB, Mota R, Fazzio A (2007) *Ab initio* study of pristine and Si-doped capped carbon nanotubes interacting with nimesulide molecules. Chem Phys Lett 439:348–353
46. Engelhardt G, Bögel R, Schnitzer C, Utzmann R (1996) Meloxican: influence on arachidonic acid metabolism. Part 2. In vivo findings. Biochem Pharmacol 51:29–38
47. Noble S, Balfour JA (1996) Meloxicam. Drugs 51(3):424–430
48. Karateev AE (2014) Meloxicam: the golden mean of nonsteroidal anti-inflammatory drugs. Ter Arkh 86:99–115
49. Ramana LN, Anand AR, Sethuraman S, Krishnan UM (2014) Targeting strategies for delivery of anti-HIV drugs. J Controlled Release 192:271–283
50. Vendrame L, Zanella I, Michelon E, Fagan SB, Mota R (2013) First principles simulations of zidovudine (AZT) molecules interacting with carbon nanostructures. J Comput Theor Nanosci 10:313–317

51. Sun X, Liu Z, Welsher K et al (2008) Nano-graphene oxide for cellular imaging and drug delivery. Nano Res 1:203–212
52. Liu Z, Robinson JT, Sun X, Dai H (2008) PEGylated nanographene oxide for delivery of water-insoluble cancer drugs. J Am Chem Soc 130:10876–10877
53. Tian B, Wang C, Zhang S, Feng L, Liu Z (2011) Photothermally enhanced photodynamic therapy delivered by nano-graphene oxide. AcsNano 5:7000–7009
54. Dolmans DE, Fukumura D, Jain RK (2003) Photodynamic therapy for cancer. Nat Rev Cancer 3(5):380–387
55. Depan D, Shah J, Misra RDK (2011) Controlled release of drug from folate-decorated and graphene mediated drug delivery system: Synthesis, loading efficiency, and drug release response. Mater Sci Eng, C 31:1305–1312
56. Zhang W, Guo Z, Huang D, Liu Z, Guo X, Zhong H (2011) Synergistic effect of chemo-photothermal therapy using PEGylated graphene rust. Biomaterials 32:8555–8561